The Pennsylvania State University
The Graduate School

ASSESSMENT OF THE PERFORMANCE OF ABLATIVE INSULATORS UNDER REALISTIC SOLID ROCKET MOTOR OPERATING CONDITIONS

A Dissertation in
Mechanical Engineering
by
Heath Thomas Martin

Submitted in Partial Fulfillment
of the Requirements
for the Degree of

Doctor of Philosophy

May 2013

The dissertation of Heath Thomas Martin was approved* by the following:

Kenneth K. Kuo
Distinguished Professor Emeritus of Mechanical Engineering
Dissertation Advisor, Chair of Committee

Fan-Bill Cheung
Professor of Mechanical and Nuclear Engineering

Gita Talmage
Professor of Mechanical Engineering

Stefan Thynell
Professor of Mechanical Engineering

Deborah Levin
Professor of Aerospace Engineering

Karen A. Thole
Department Head of Mechanical and Nuclear Engineering
Professor of Mechanical Engineering

*Signatures on file in the Graduate School

Abstract

Ablative insulators are used in the interior surfaces of solid rocket motors to prevent the mechanical structure of the rocket from failing due to intense heating by the high-temperature solid-propellant combustion products. The complexity of the ablation process underscores the need for ablative material response data procured from a realistic solid rocket motor environment, where all of the potential contributions to material degradation are present and in their appropriate proportions. For this purpose, the present study examines ablative material behavior in a laboratory-scale solid rocket motor. The test apparatus includes a planar, two-dimensional flow channel in which flat ablative material samples are installed downstream of an aluminized solid propellant grain and imaged via real-time X-ray radiography. In this way, the in-situ transient thermal response of an ablator to all of the thermal, chemical, and mechanical erosion mechanisms present in a solid rocket environment can be observed and recorded. The ablative material is instrumented with multiple micro-thermocouples, so that in-depth temperature histories are known. Both total heat flux and thermal radiation flux gauges have been designed, fabricated, and tested to characterize the thermal environment to which the ablative material samples are exposed. These tests not only allow different ablative materials to be compared in a realistic solid rocket motor environment but also improve the understanding of the mechanisms that influence the erosion behavior of a given ablative material.

Table of Contents

List of Figures

Nomenclature

List of Acronyms

ASNBR	Asbestos Silica Filled NBR
ASRM	Advanced Solid Rocket Motor
CFEPDM	Carbon Fiber Filled EPDM
CMA	Aerotherm Charring Material Ablation Code
DAQ	Data Acquisition System
EPDM	Ethylene Propylene Diene Monomer
HPCL	High Pressure Combustion Laboratory
IHCA	Inverse Heat Conduction Analysis
KFEPDM	Kevlar Filled EPDM
NBR	Nitrile Butadiene Rubber
PBI	Polybenzimidizole
PICA	Phenolic Impregnated Carbon Ablator
PSU	The Pennsylvania State University
RSRM	Reusable Solid Rocket Motor
RTR	Real-Time Radiography
SRM	Solid Rocket Motor
SSRM	Simulated Solid Rocket Motor

Variable Definitions

English Letter Symbols:

A	area	Nu	Nusselt number
c	specific heat	q	quantity of heat
F	radiation view factor	Re	Reynolds number
h	heat-transfer (film) coefficient	St	Stanton number
J	radiosity	T	temperature
k	thermal conductivity	u	velocity component in x direction
m	mass	x, y, z	Cartesian Spatial Coordinates

Greek Letter Symbols:

α	absorptivity	ρ	density
δ	momentum thickness of boundary layer	σ	Stefan-Boltzmann constant
ε	emissivity	τ	transmissivity

Subscripts:

∞	evaluated at the free-stream state	*i*	time index
a	evaluated at the aperture location	*p*	evaluated for combustion products
conv	due to convection	*rad*	due to radiation
film	average of free-stream and surface states	*s*	evaluated at surface

Acknowledgements

The author would like to thank the support of ATK-Launch Systems under the management of Mr. James Braithwaite to Combustion Propulsion & Ballistic Technology Corporation (CPBT Corp.) with a subcontract to The Pennsylvania State University. This project was associated with the NASA Space Shuttle Booster program, the insulation erosion portion of which was managed by Mr. J. Louie Clayton of NASA-MSFC. A portion of this work was also funded by a contract to CPBT Corp. from NASA-MSFC under the management of Dr. Matt Cross (P.O. #NNM12AA99P). His interest and technical advice were highly appreciated. Special thanks also go out to Larry Jones of Medtherm Corporation for his work performing the radiometer calibration and time response tests and for his technical guidance regarding these critical procedures.

The author would also like to thank each of the current and former HPCL members who have contributed to this work: Dr. Eric Boyer for always being ready to listen to ideas and providing constructive feedback; Dr. Andrew Cortopassi for seeing to the details of the X-ray RTR system, his tireless efforts to make to Outdoor Test Site livable, his assistance with general problem solving, and his management of the Soda Fund; Mr. Matthew Degges for the hours spent chasing gremlins from thermocouple circuits, his development of so many of the practical solutions for fabrication, installation, and removal of test apparatus components, and his introduction of levity into what was often otherwise fatiguing and frustrating work; Mr. Peter Ferrara for his

assistance with the mechanical design of the solid rocket motor components and for being a steadying presence while the author was still gaining his sea legs; Dr. Ryan Houim for both his instruction in and performance of CFD simulations and Fortran90-style programming for the inverse heat conduction analysis code, as well as his vital theoretical insight; Dr. Jeffery Moore for his work in proposing this project and guiding its inception, and Mr. Timothy Wawernia for calling Lockheed. A very special thank you is due to Prof. Baoqi Zhang, who spent many, many hours performing tedious and meticulous work making thermocouples and fabricating heat flux gauges and temperature sensors. It may be truly stated that without his efforts, no heat flux measurement could have been performed.

The author would also like to thank all the former HPCL members who did not contribute directly to this work, but who served as sounding boards for ideas or just provided a sense of camaraderie, either within or without of the lab, to lift the general despair that it engenders: Mr. Alexander Colletti, Dr. Jonathan Essel, Dr. Brian Evans, Mr. Jeffrey Krug, Mr. Patrick Kutzler, Mr. Daniel Larson, and Mr. Matthew Sirignano.

Additionally, the author of this work would like to acknowledge his academic advisor, Dr. Kenneth K. Kuo, whose tenacious support was critical and very much appreciated during the lean years of this project and whose guidance and instruction were truly invaluable.

Finally, the author of this work would like to thank his family for their love and support – for listening to all of his gripes, bearing all of his ill humors, and offering timely encouragement and perspective through the years of this endeavor.

Chapter 1 Introduction

1.1. Ablative Internal Insulators in Solid Rocket Motors

Large solid-propellant rocket motors (SRMs) have been used for many years as first-stage augmentation for launch vehicles due to their ability to generate the large amounts of thrust required for quick initial acceleration with relatively little inert mass compared with liquid-propellant rocket engines (LREs) [1]. The LRE's disadvantage in large-scale thrust production is due to practical constraints on the size of the turbo-pumps required to deliver fuel and oxidizer to its combustion chamber. These constraints limit the mass flow rate of propellant through a single LRE; consequently, multiple LREs are required to produce the necessary liftoff thrust, adding significant inert mass to a launch vehicle [1] [2]. Therefore, it has become common practice to augment the first stage of a launch system with strap-on SRMs to reduce the number of LREs required for liftoff, then jettisoning the SRMs at the time in the flight when the benefits of the superior efficiency of the LREs outweigh the thrust production of the SRMs. The premier example of this type of SRM application is the Space Shuttle's Reusable Solid Rocket Motor (RSRM), which provides the majority of the liftoff thrust for the Space Shuttle. This same SRM booster concept is also used contemporaneously by the European Space Agency's Ariane V launch vehicle, the Japan Aerospace Exploration Agency's H-II launch vehicle, and others [2]. SRMs are heavily utilized for ICBMs, as well, due to the storability and reliable ignition characteristics of solid propellants that allow them to be fired on short notice. Therefore, SRMs are anticipated to be in service for many years to come, as they offer reliable, cost-effective, high thrust propulsion for a variety of applications [2] [3].

The thermal environment in the combustion chamber of a rocket motor is intense due to the high temperature (> 3000 K) combustion products and high heat transfer rates due to local high gas velocities. In metallized SRMs (those whose propellant formulations include the use of a metallic fuel, such as aluminum), the existence of condensed-phase metal oxide particles in the combustion products significantly enhances wall heat transfer due to radiation [3]. In order to insure structural integrity, the internal surfaces of the rocket motor must be maintained at a safe operating temperature by either a cooling mechanism or insulation. Unfortunately, the lack of pumping hardware that makes SRMs attractive for high-thrust applications also precludes the use of regenerative cooling for the nozzle and/or combustion chamber, as is typical on liquid engines, thus, the rocket's structure must be insulated. Insulating the walls with a high-temperature, low-thermal-conductivity ceramic seems logical; however, such materials are rather sensitive to thermal shock and have a significant thermal expansion mismatch with the rocket's structural materials, which causes further design difficulties [4]. Therefore, ablative materials are typically used to protect the structure of a SRM from its high internal heat loads.

While most engineering materials are prized for their ability to withstand severe environments, the superior insulating characteristics of ablative materials are predicated on their degradation. The decomposition of an ablative insulator involves both endothermic processes and heat blockage effects, each of which absorb or deflect energy that would have been otherwise transferred to the wall in the absence of the ablator and cause this energy to remain in the exhaust products, where it is either converted to kinetic energy or merely expelled out of the nozzle. In this way, the ablative insulator is superior to a non-degrading, low-thermal-diffusivity insulator, because relatively little heat is transferred to the structure, either during the firing or during post-firing heat soak.

1.2. Decomposition of Ablative Materials

The decomposition of ablative materials is complex, involving many and multifarious physical and chemical processes, all of which are driven by the combined effect of convective and radiative heat transfer from the hot combustion products to the surface of the ablator. In the initial phase of decomposition, the energy is transferred within the ablative material purely by conduction, which causes the material to swell due to thermal expansion and vaporizes any absorbed moisture in the material [5]. Once the ablator reaches its decomposition temperature, the virgin material begins to pyrolyze via endothermic chemical reactions, generating relatively cool, fuel-rich pyrolysis gases and leaving behind a layer of porous, carbonaceous residue known as char. Continued heating of the ablator causes the reaction, or pyrolysis, zone to proceed further into the material, thickening the char layer, which now behaves as a thermal shield over the virgin material, as the high surface temperature of the char reduces both convective and radiative heat transfer from the combustion products. The pyrolysis gases escaping through the char layer remove heat from the char layer via convection and further endothermic decomposition and produce surface blowing, which thickens the boundary layer of the flow of combustion products, thereby reducing convective heat transfer to the char surface. If the species contained in the pyrolysis products are strong emitters or absorbers of radiation (i.e. C_2), the pyrolysis gas flow that provides the convective blockage effect will also contribute a radiation blockage effect by providing a radiation shield of relatively cool, radiatively-participating species between the combustion products and the char surface [6]. The pyrolysis products may also react chemically with the boundary-layer gases after emerging from the char layer. As the surface temperature of the char layer continues to rise, reradiation from the hot char surface will become a more significant mode of heat accommodation. If the ablator contains a meltable component, this component will melt, absorbing additional heat via its heat of fusion, and form a liquid layer on the surface of the ablator, which further protects the underlying material by blocking convection and vaporizing [7]. The pyrolysis gases will percolate through this melt layer, where further chemical reactions may take place [8]. Under continued heating, the char layer will reach a temperature at which it will begin to recede via oxidation, sublimation, or mechanical removal by shear forces or spallation [9], and the surface temperature of the ablator will be maintained at the so-called failure temperature of the ablative material [5].

1.3. Characteristics of Ablative Materials

As an ablator is a thermal insulator, its most important properties are thermal properties: ablation temperature, density, specific heat, and thermal conductivity. A superior ablative material will exhibit a high ablation temperature to retard the onset of ablation, low thermal conductivity to inhibit the flow of heat through the material, and high specific heat to absorb large quantities of heat while maintaining relatively low temperatures. Ideal density, however, is a Pareto optimum of two competing effects: high density for low recession rates and low density for reduced inert mass [10]. Nevertheless, in launch vehicle applications, minimizing mass is a higher priority than minimizing recession rate, so low-density ablators are typically sought. An ablative insulator must also decompose endothermically and generate profuse amounts of gases to absorb and block heat incident on the material. Furthermore, an ablator must have favorable mechanical properties to withstand the high stresses and vibrations present in the SRM environment. Given these criteria, polymers are a natural choice for use as ablative insulators, as they exhibit all of the above criteria regarding thermal properties and boast highly endothermic degradation.

In current applications, ablative materials are generally composite materials consisting of a polymeric matrix and high-temperature reinforcement fiber. The polymer matrix performs the primary function of endothermically decomposing to balance the incident heat flux; however, since the resultant char is rather weak and brittle, high-temperature fibers are used to structurally reinforce the char and mitigate its mechanical removal [9]. Phenolic resin is the most commonly used polymer matrix [5] due to its excellent ablation resistance; nevertheless, rubbers, such as ethylene propylene diene monomer (EPDM) and nitrile butadiene rubber (NBR), are preferred for service as internal insulators, because of their superior mechanical flexibility [10]. Flexibility is critical for internal insulators because, in addition to their role as thermal insulators, they serve to bond the propellant grain to the motor case, which deforms under pressurization. The flexibility of the rubber prevents the mechanical stresses due to case deformations from being transmitted to the propellant grain, where they could cause cracking or de-bonding, which could lead to rapid over-pressurization and ultimately failure of the motor [10].

1.4. Other Uses of Ablative Materials

Due to their ability to accommodate large heat loads and heating rates, ablative materials are used as thermal protection in other severe thermal environments encountered in aerospace applications, such as rocket nozzles, re-entry heat shields, and missile launcher blast tubes. Each of these applications occupies a unique thermal and mechanical paradigm, and, therefore, the ideal material for each application is selected based on different performance criteria. Rocket nozzles experience higher heat-transfer rates than internal insulation since the mass flux of product gases is higher through the nozzle than in any other location in the motor. Since the mass of the nozzle is small compared to the remainder of the rocket and the diameter of the nozzle is a critical parameter influencing the overall performance of the rocket motor [11], nozzle materials are selected primarily for minimum erosion rate, with inert mass being a subsidiary concern. Therefore, dense, rigid materials such as silica- and carbon-cloth-phenolics as well as carbon-carbon are typically employed in nozzle applications, as they offer a higher erosion resistance than elastomer-matrix ablatives [10]. The best-known use of ablative materials is likely in the atmospheric re-entry heat shields of manned space capsules, such as the Mercury, Gemini, and Apollo, and unmanned space probes like Galileo and Stardust. Currently, the material of choice for this application is Phenolic Impregnated Carbon Ablator (PICA), which utilizes a low-density fibrous carbon tile matrix infiltrated with phenolic resin to minimize inert mass while maintaining high ablation resistance [12]. Ablative materials are also used in missile launching systems to protect the launcher's components from the destructive effects of an impinging rocket plume [5]. These materials are subjected to not only the high temperatures of the plume gases, but also to the abrasive effects of high-speed impinging alumina particles. Nevertheless, since this ablative system is not part of the structure of the rocket itself, weight is minimally important, so materials are selected primarily on their erosion performance. Glass-phenolics, such as MXBE-350 and H41N, are typically chosen for this application, as the glass fibers form a protective melt layer on the surface of the ablator that significantly reduces erosion [13]. Despite the differences in these applications, however, the purpose of these materials is essentially the same, and research intended for one application can still provide valuable insight into the mechanisms at work in another.

1.5. Asbestos Fiber Replacement

The space shuttle's RSRM employed asbestos-silica-filled NBR (ASNBR) as its primary internal case insulation; however, the adverse health effects attributed to asbestos fibers makes its production expensive and unattractive [14]. Therefore, NASA has sought its replacement for many years, but replacement has been challenging to effect as the comprehensive performance of ASNBR is difficult to match and qualification testing is expensive [15]. The aft dome of the RSRM was insulated with carbon-fiber-filled EPDM (CFEPDM), as it has demonstrated superior ablation resistance in this region of the motor [14]; however, using two different types of insulation for a single booster is undesirable due to the increased costs associated therewith. Kevlar-filled EPDM (KFEPDM) was selected as the most promising candidate to replace both ASNBR and CFEPDM by Tam and Bell [16] in the design of the Advanced Solid Rocket Motor (ASRM), which was developed to replace the RSRM, and by Fitch and Eddy [14], due to its excellent performance in preliminary testing and sub-scale SRM firings. Nevertheless, KFEPDM was ultimately rejected as a suitable replacement because of its poor performance vis-à-vis CFEPDM in the full-scale RSRM aft dome, and its lack of wide-ranging applicability, as multiple KFEPDM formulations were required to meet the diverse requirements of the different regions of the booster [14]. While the Space Shuttle has recently been retired, a modified version of the RSRM is currently slated to be used as a booster for NASA's next-generation heavy-lift Space Launch System; therefore, there still exists the need to replace the current ASNBR/CFEPDM insulation system with one that is safer and more cost-effective. Within the past decade, another candidate material has been proposed: polybenzimidizole-fiber-filled NBR (PBINBR), but at this time sufficient testing has not been performed to qualify the material for use in man-rated launch systems. PBI fibers are aramid (aromatic polyamide) fibers similar to Kevlar, and offer the same positive traits of tensile strength and high-temperature stability, but it has yet to be determined if they will have similar disqualifying weaknesses.

1.6. Motivation and Objectives

Unfortunately, despite the modeling and characterization work that has been performed to date, it is unknown exactly why KFEPDM performed differently during full-scale motor firings than during sub-scale motor firings [14]: a fact that underscores the need for further research into the decomposition behavior of ablative materials, particularly under realistic SRM conditions. The complexity of the process of ablative decomposition of internal insulators in SRMs causes it to be a difficult process to accurately model and, thus, difficult to accurately predict the behavior of ablative insulators in SRM environments. This uncertainty increases the risks associated with insulator design and typically produces excessive conservatism in prescribed insulation thicknesses, which, in turn, reduces SRM performance and increases cost by saddling the booster with superfluous inert mass. In order to reduce this uncertainty through improved understanding of ablative material degradation processes and to enhance the predictive capability of the ablation models by providing data for model validation, this study was initiated with the primary objective of characterizing the decomposition behavior of two particular ablative insulators of interest, PBINBR and CFEPDM, under realistic and precisely-quantified SRM operating conditions.

In order to observe the PBINBR and CFEPDM samples in an environment nearly identical to that present in a full-scale SRM in terms of temperature, pressure, convective and radiative heat transfer rates, chemical species of combustion products, viscous shear, and alumina particle impact, the subscale SRM displayed in Figure 1-1 was developed. Locating two samples of ablative insulation downstream of an end-burning, aluminized solid propellant grain (TP-H1148) ensured similarity of temperature, gaseous species, alumina particle content, and radiative heat transfer rates of the combustion product flow to that of the full-scale SRM, while the nozzle and flow channel cross-sectional areas were sized to produce full-scale-similar chamber pressures and flow velocities (and thus viscous shear and convective heat transfer rates), respectively.

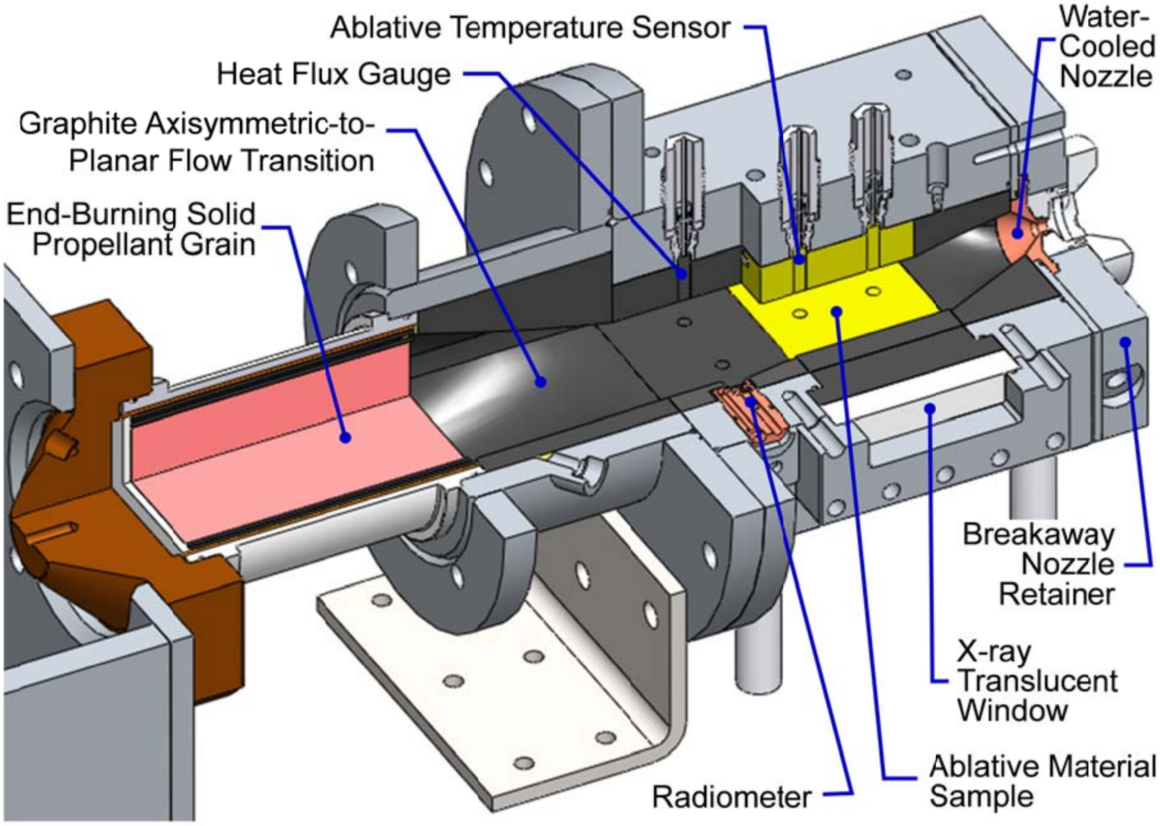

Figure 1-1. Cut-away view of the subscale SRM used to characterize ablative internal insulators

The generation, development, and erosion of a char layer on the ablative material samples as a consequence of their exposure to the SRM environment was observed and recorded with real-time X-ray radiography (X-ray RTR), which produced time-resolved image sequences of the SRM interior. The in-depth thermal response of the ablative material samples was monitored by embedding multiple micro-thermocouples at different depths within the samples to produce temperature histories for those known subsurface locations.

Precise quantification of the conditions to which the ablative material samples are exposed within the SRM is critical to the utility of the X-ray RTR and subsurface ablative material temperature data for model validation purposes, as the model inputs as well as their corresponding outputs must be known. To this end, SRM chamber pressure, total wall heat flux, and radiative wall heat flux are measured in the SRM firings conducted in this study. While pressure is measured using commercially-available (Setra Systems Model 206) pressure transducers, both the total heat and thermal-radiation-only fluxes to the SRM chamber wall in the section of the flow channel directly upstream of the ablative material samples are measured using custom-designed gauges. Like the degradation behavior and subsurface temperature of the ablative material samples, each of the SRM environment measurements is time-resolved, so that the behavior of the ablative material samples at any particular moment can be directly related to the value of both present and past pressures and heat fluxes.

Chapter 2 Literature Review

2.1. Ablative Material Testing Methods

Given the importance of internal insulation to the safety and performance of a SRM, ablative materials have been extensively tested since the inception of their use. Nevertheless, the severity of the SRM internal environment that necessitates the use of ablative materials makes in-situ studies prohibitive. For this reason, the vast majority of ablative material degradation studies performed to date either use real-time diagnostics in a more accessible heating apparatus, or simply compare pre- and post-firing measurements taken from rocket motor firings. The advantages of the former type of testing include its ability to provide a well-characterized thermal environment in which to expose an ablative material sample, easier access for real-time diagnostics, and generally more cost-effective testing than possible in an SRM. Its primary disadvantage, however, lies in its inability to accurately replicate each of the thermal, chemical, and mechanical mechanisms involved in the ablation process within an SRM.

2.1.1. Laser Heating

The simplest of these methods merely heats the surface of an ablative material sample with a high-power laser to impart heat fluxes within the range of those present in the SRM. This technique has been demonstrated by Russell and Strobel [17], Maw et al. [18], and Brewer [19], and is convenient because it is possible to know and control the precise heat flux incident on the sample as a function of time, and the surface temperature of the ablative can be measured via optical methods, i.e. a pyrometer [19]. Unfortunately, these tests do not subject the sample to flow of gases or particles over the surface of the ablative or to the same chemical species present in the combustion chamber, and are, therefore, only illustrative of the thermal mechanisms of ablative degradation. The results of these types of tests, however, still have value either as preliminary screening tests, or in revealing the behavior of ablatives in radiation-dominated environments such as the forward dome of a SRM or the stagnation point of a re-entry vehicle.

2.1.2. Arc-Jet Testing

Ablative materials are often tested in wind tunnels whose working fluid is heated to high temperatures by electric arcs, and accelerated to high velocities. This type of testing is known as arc-jet testing and was developed primarily for the evaluation of re-entry heat shield materials, as this environment, high Mach number flow and air atmosphere, closely approximates atmospheric re-entry conditions. Ablative material samples may be placed at varying impingement angles relative to the jet to adjust the incident heat flux and mechanical shear conditions on the sample. Arc-jet tests have been performed on heat shield materials [12] [20] [21] [22] [23] [24], such as phenolic-nylon and PICA. In these tests, the incident heat flux may be calibrated prior to the test by replacing the ablative sample with a heat flux gauge [21]. During the tests, the surface temperature of the material samples has been measured with an optical pyrometer [21] [12] [23], and the in-depth ablative temperatures measured with embedded thermocouples [12] [23] [24]. However, while the fidelity of arc-jet testing with regard to re-entry conditions is high, it is rather lacking for SRM internal insulators, as it does not approximate SRM product gases or flow field conditions, including the presence of condensed-phase products.

2.1.3. Plume-Impingement Testing

Rather similar to arc-jet testing is plume-impingement testing, which replaces the electrically heated jet with the exhaust plume from a small rocket motor. This type of testing has been used extensively to evaluate ablative materials to be utilized in protecting missile launchers from the destructive effects of missile plumes, due to obvious similarities in these environments. An excellent example of this type of facility is the simulated solid rocket motor (SSRM) facility developed by Chaboki et al. [25]. Many experiments have been performed in this facility over the years, testing ablative materials for missile launcher protection [26] [27] [28], SRM internal insulation [29], and rocket nozzle materials [30]. Multiple types of instrumentation have been used among these ablative studies to measure heat flux, bond-line temperature, surface temperature, and final erosion depth. Heat flux measurements were made prior to sample testing with different types of heat flux gauges to establish the average cold-wall heat flux at the ablative sample location. These gauges included: the Gardon gauge, flat plate calorimeter, pencil probe surface (eroding) thermocouple [25], and a commercially available gauge of an unspecified type [29]. Bond-line temperatures were measured during the post-firing heat-soak using a thermocouple sandwiched between the backside of the ablative sample and its support plate [29]. The surface temperature of the ablative material sample was measured immediately after the rocket firing using an infrared pyrometer focused at the center of the sample [31] [29]. Final erosion depth has been measured with a number of techniques including: pencil-point dial indicator [29], LVDT, eddy current device, and ultrasonic device [25], but no attempt was made to obtain time-resolved surface recession measurements. Plume-impingement testing is one step nearer to simulating SRM conditions than arc-jet testing as the composition of the impinging products is very similar to that of a SRM, even to the point of including condensed-phase products [26]. Regardless, the temperatures of the torch exhaust are much lower than those found in an SRM, and the flow-field structure deviates significantly as well, relegating this method, like those preceding it, to strictly screening duty for internal insulators.

2.1.4. Subscale SRM Testing

Subscale SRM testing clearly represents the highest-fidelity testing method vis-à-vis full-scale testing as compared to the abovementioned methods. As such they have been used many times for the final screening tests for internal insulators and nozzles before they are tested in a full-scale motor [32] [33] [34] [18]. The instrumentation in these tests is typically limited to pre- and post-firing erosion depth and mass loss measurements, as the function of these tests is merely to discriminate between multiple candidate materials for a given application and establish baseline average erosion rates for predicting required thicknesses in full-scale motors. Unfortunately, the fidelity of subscale tests comes at the cost of instrumentation access and survivability, which contributes to the general lack of instrumentation in subscale SRMs

2.2. Transient Erosion Measurements

Few attempts have been made to measure the transient decomposition behavior of ablative materials in more accessible forms of testing, i.e. laser, arc-jet, or plume-impingement, much less within the harsh environment of a SRM. Three different types of real-time ablation measurement techniques were proposed by LeBel and Russell [35] for re-entry heat shield materials. The first of these was called a make-wire ablation sensor, which was simply a pair of fine wires embedded in the ablative material parallel to the direction of heat flow, as shown in Figure 2-1. As embedded, these wires were not in contact with each other. The virgin ablative material was not electrically conductive; however, the char formed through its pyrolysis was. Therefore, when the char layer receded to the end depth of the wire pair, the circuit, whose resistance was constantly monitored, was closed. In this way, several pairs of wires embedded to different depths in an ablative material effectively tracked the recession of its char-virgin interface.

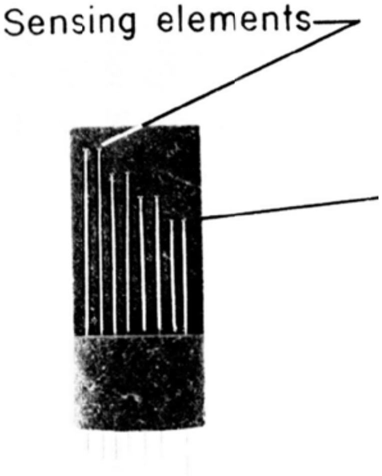

Figure 2-1. Make-wire sensor [35]

This type of measurement, which includes an array of sensing elements embedded in the ablative material that simply change state when the char-virgin interface or material surface reach them is rather common and includes not only the make-wire sensor but also the spring wire sensor [35], which tracks the surface rather than the char-virgin interface, and embedded thermocouples, whose temperature spike signals the arrival of the char-virgin interface [36]. While these instruments provide a relatively simple real-time measurement of ablative degradation, their temporal resolution is, in effect, very low due to practical limits on the number and spacing of the wires or tubes that make up the sensing elements in the ablative material. One method of obtaining a continuous measurement of erosion rate is the light pipe sensor [35], which embeds a high-temperature optical fiber parallel to the direction of the heat flux in the ablator that directs light emitted by the surface of the char to a photodetector. As the char surface erodes and approaches the fiber, the intensity of the light collected by the photodetector increases, indicating the location of the surface. The eroding potentiometer [37] is another device that provides continuous real-time erosion rate data. It resembles the make-wire sensor in that it consists of a pair of twisted wires installed parallel to the direction of the heat flow in an ablative sample. As the material erodes, the wires, whose melted tips form an electrical circuit, erode as well. The wires' recession shortens their electrical path, thereby reducing their resistance, which is monitored and correlated to the recession of the ablator. Despite the simplicity of these devices, each of them must be embedded into the ablative material itself, and their lead wires must have a path through the motor case to the exterior of the motor. Neither of these requirements is trivial to meet, so a measurement technique is sought that can provide continuous real-time measurements of erosion, whose sensing equipment is external to the test chamber.

2.2.1. Ultrasonic Pulse-Echo Method

One such method is the ultrasonic pulse-echo method, in which a transducer emits an ultrasonic pulse in a material, a portion of which will reflect from abrupt changes in acoustic impedance normal to its direction of travel, which occur at material interfaces [38]. The transducer senses this reflected wave, and its propagation time is proportional to the distance between the transducer and the interface. In ablative materials, the ultrasonic wave reflects primarily from the char-virgin interface, so the char surface is not detected [39]. The propagation time, unfortunately, is also a function of the material temperature (both local value and gradients through the material) and the stress-strain distribution in the material, which is related to pressure [39]. Despite this complication, the ultrasonic technique has been used extensively for determining the regression rate of solid propellants [38] [40] [41] and hybrid fuels [42] with satisfactory results. However, for the relatively fast regression rates of propellants (> 1 mm/s), the thermal effect is insignificant, while the pressure effect must be corrected [38]. The opposite is true for low-recession-rate materials, i.e. ablative materials: the pressure effect is negligible, while the thermal profile variation is important. In fact, the effect of the thermal profile variation is so strong that the heat flux into the material has as much effect on the propagation time of the ultrasonic wave as the material recession [39]. Therefore, in order to obtain real-time recession rate data for an ablative material via the ultrasonic method, the transient thermal profile through the ablator must be known [43].

Knowledge of the transient thermal profile necessitates the use of a thermo-ablative code, whose inputs include empirical thermal response data for the material being tested. The thermal response of an ablative has been determined by imparting a known heat flux to a sample with a CO_2 laser and recording its surface and subsurface temperatures with an optical pyrometer and embedded thermocouples, respectively [43]. As mentioned previously, laser testing may not accurately represent the thermal environment in which the ablative material must perform, and, therefore its response may differ significantly. These considerations severely limit the applicability of the ultrasonic method to internal insulation testing in SRMs.

2.2.2. Real-Time X-ray Radiography

Real-time X-ray radiography (RTR) has been utilized to great effect in SRMs because it allows the internal processes of an SRM to be observed without affecting those processes. RTR has been utilized in subscale and full-scale rocket motor firings to study alumina slag flow [44] [45], solid propellant regression rates [46], hybrid fuel regression rates [42], and graphite nozzle erosion [11]. Since the contrast of X-ray images is essentially supplied by density gradients within materials, it is an ideal technique for examining the decomposition of ablative materials. Unlike practically all other methods of determining ablative material charring and erosion, RTR is able to precisely locate both the char surface as well as the char-virgin interface, a fact demonstrated by Rollbuhler [47], who used X-ray images of fired ablative nozzles to determine the amount of throat erosion and the final thickness of the char layer. X-ray radiography is capable of similar feats in real-time, with RTR being used to track both the char-virgin interface and the char surface during laser heating of heat shield materials in a quantifiable manner [17]. In the SRM environment, RTR has been demonstrated to be an effective way to observe not only charring and erosion behavior, but also ply lift dynamics in the nozzle of a subscale SRM [48].

2.3. Subsurface Ablative Material Temperature Measurements

The temperature distribution in the ablative material is the critical determinant of decomposition, regardless of the mode of heating [49], as it influences both the state and the properties of the ablator at each location within the material. As such, it is often measured in empirical studies of material ablation. In-depth ablative material temperatures in SRMs have been measured almost exclusively by thermocouples embedded at specific locations within the material [50]. This technique has been successfully utilized for nozzle materials [47] [51] [52] [18] and internal insulation [37]. Of these, Rollbuhler [47] and McWhorter et al. [37] embed the thermocouples into the bulk insulation material during the lay-up and curing processes, which minimizes thermocouple temperature field distortion and response lag, but is difficult to implement. Baker et al. [51] and Maw et al. [18] instrument a plug of identical ablative material with thermocouples that is later installed in the bulk insulation, which is much simpler to implement in an SRM.

2.4. *Heat Flux Measurement*

2.4.1. *Heat Flux Measurement Methods*

While the temperature distribution within an ablator is the critical determinant of decomposition, the temperature distribution is itself dependent on both the magnitude and the mode of heating incident on its surface [49]; therefore, understanding the degradation behavior of an ablator in a SRM environment begins with knowledge of the wall heat flux. Instrumenting an SRM to measure heat flux or any other flow-field parameter, is difficult due to its harsh environment, which will quickly destroy many standard devices [53]. The necessity of such measurements to the understanding of ablative material response in SRMs, however, has led to several attempts to measure their wall heat flux. Slug calorimeters, mounted flush with the internal insulator surface, have been used in past studies of the SRM thermal environment [54], including a recent study at the HPCL [55], and it recommends itself for this type of duty due to its simplicity (in both design and data reduction method) [56] [57], ruggedness, and economy (inexpensive and straightforward to fabricate) [57]. Nevertheless, the slug calorimeter is inherently vulnerable to cross-conduction and thermal perturbation errors, which can cause them to report total wall heat fluxes that are significantly greater than exist in their absence [56] [57] [58].

Deduction of the surface heat flux to a slug calorimeter requires that the slug be modeled as zero-dimensional using the lumped capacitance approximation; therefore, the slug material must possess a relatively high thermal conductivity. In addition, the slug calorimeter is a transient method of heat flux measurement; that is, the slug must continually store all of the energy it absorbs throughout the duration of the test in order for the heat flux to be accurately measured [58]. This requirement dictates that the slug be insulated around its periphery, even when installed in a material that is a good thermal match (similar thermal diffusivity). Therefore, a high-thermal-diffusivity slug calorimeter is inevitably surrounded by a low-thermal-diffusivity material that adopts a very different temperature profile after the onset of heating, regardless of the mode of heating [58]. One error introduced by the presence of this lateral gradient is known as cross-conduction error, and it is illustrated in Figure 2-2, which was calculated using Fluent™ (version 6.2) flow modeling simulation software. In this simulation, a heat flux a high-thermal-diffusivity (1.1×10^{-3} m^2/s) slug calorimeter, was placed in a low-thermal-diffusivity (4.6×10^{-7} m^2/s) flat plate with and exposed to a flow of hot ($T_\infty = 3500$ K), gaseous SRM combustion products ($\rho = 3.82$ kg/m^3, $\gamma = 1.1$). The product flow was modeled as turbulent using a realizable k-ε model and a very fine mesh ($y^+ < 0.6$). The peripheral insulator adopts a much higher surface temperature than the slug under heating, establishing a temperature gradient that transfers heat laterally into the slug. The opposite is true in the deeper regions of the slug where the slug is warmer than the surrounding insulation; nevertheless, while this produces a slightly counterbalancing effect, the temperature gradient in this region is much smaller than that near the surface, so the slug will experience a significant net gain of heat, and, therefore, report a higher heat flux than is actually incident on the surface [58].

The other consequence of the disparity in surface temperature is confined to applications where convection is significant. As also illustrated in Figure 2-2, when the convective flow encounters an abrupt change in the surface temperature at its boundary, a new thermal boundary layer is developed. In the same way that the film coefficient spikes to a theoretically infinite value at the leading edge of the original boundary layer, the film coefficient becomes theoretically infinite at this new thermal "leading edge", despite the fact that the momentum boundary layer remains unaffected. This effect is shown graphically in Figure 2-3, where the film coefficient was calculated for the situation shown in Figure 2-2, as well as for the insulating wall in the absence of the slug calorimeter. Though the magnitude of the film coefficient decays rather rapidly with downstream distance, and the boundary layer eventually recovers, the effects of this heat transfer spike are significant for a relatively small slug, as demonstrated in Figure 2-4, which shows the different surface heat fluxes calculated under the same conditions as for Figure 2-3 both with and without the calorimeter. The thermal perturbation of the

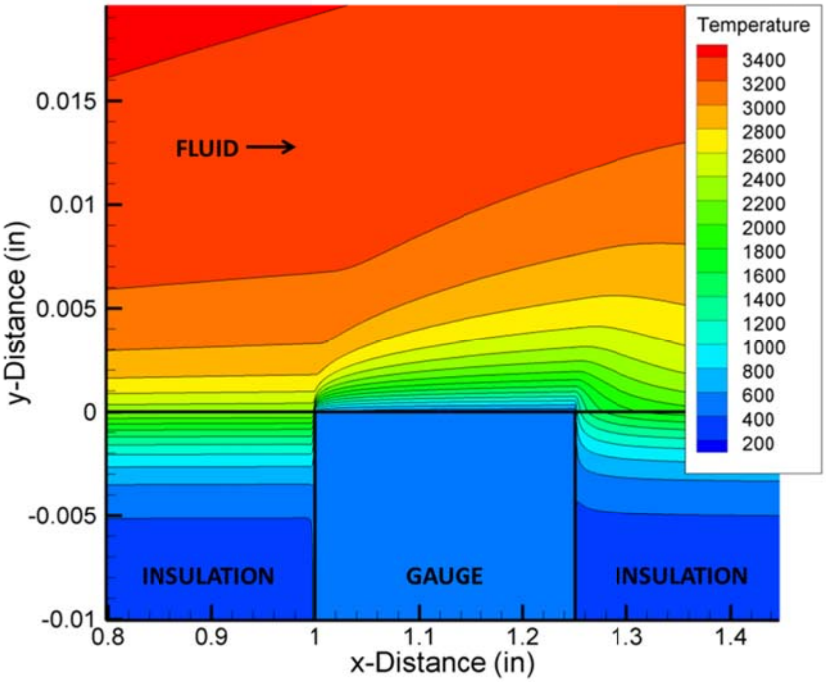

Figure 2-2. CFD-computed temperature contours near a slug gauge in a simulated SRM combustion product flow

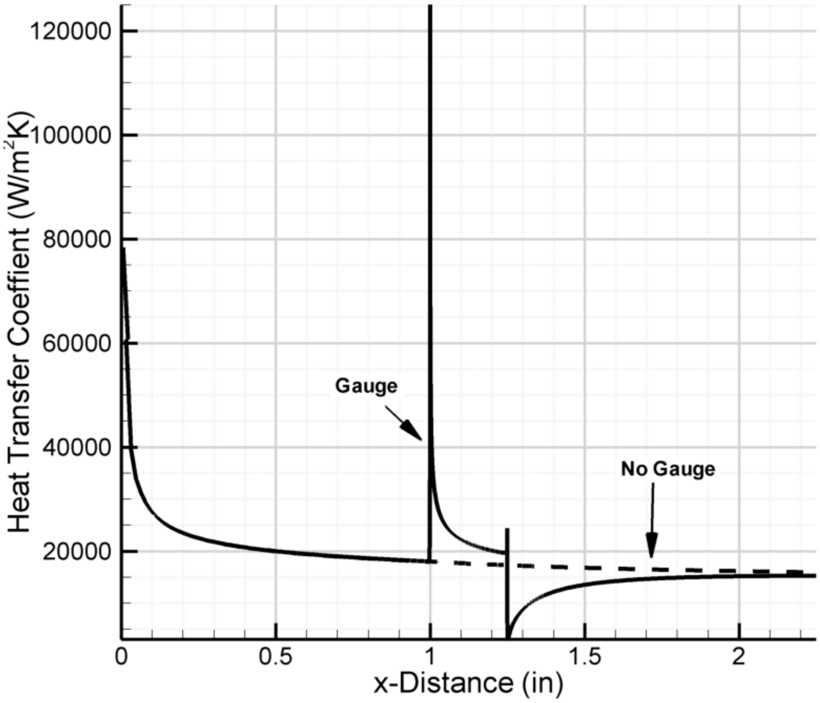

Figure 2-3 CFD-Computed heat transfer coefficient for a slug calorimeter in an insulator in an SRM combustion product flow

boundary layer causes the slug calorimeter to measure a higher heat flux at all times than would be present in its absence, and furthermore, the magnitude of the difference between these fluxes is not constant or even linear, making a theoretical correction of this error difficult. It should be noted that though this phenomenon is often referred to as the "thermal perturbation error", it is not an error in the sense that cross-conduction is, as the gauge is correctly reporting the heat flux incident on its surface; however, this measured heat flux is not indicative of the heat flux that would be present in its absence. Due to this fact, the effects of the thermal perturbation error are not restricted to slug calorimeters, but are present in any type of heat-flux gauge that adopts a different temperature than its surroundings [58], i.e. one that is made of a material whose thermal diffusivity differs from the material into which it is installed.

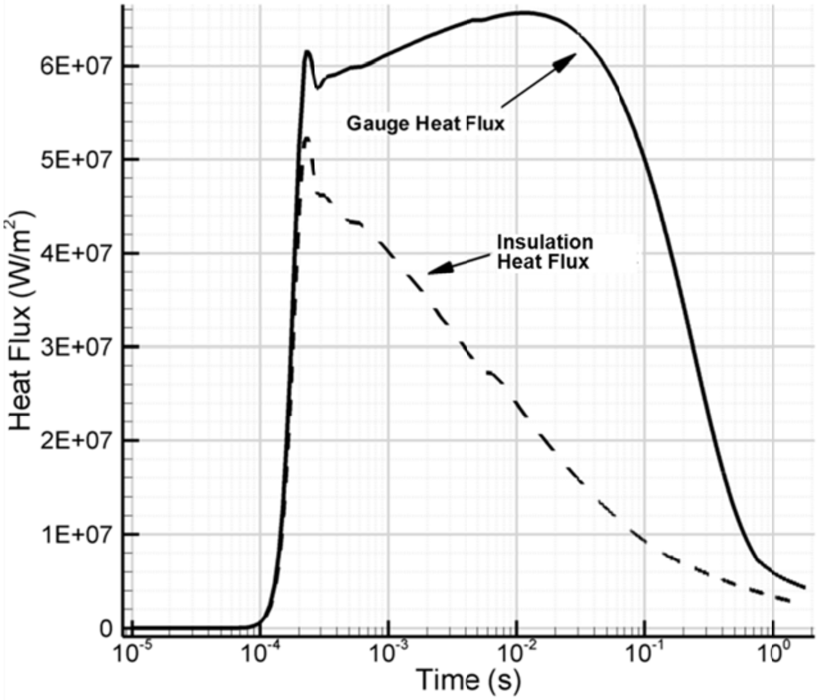

Figure 2-4 Computed transient heat flux for slug calorimeter in an insulator

Both empirical and theoretical correction factors have been proposed to account for the thermal perturbations induced by heat flux gauges. Early analytical attempts at these corrections were proposed by Rubesin [59] and Reynolds et al. [60], who arrived at the same general form for a flat plate with a step change in temperature by employing approximate integral solutions of the turbulent boundary-layer equations, which are closed-form and therefore straightforward to apply to experimental data. Nevertheless, the many assumptions and approximations required to make these analytical derivations tractable [58] cause significant (~ 30% [61]) deviations from the real case, even in flat plate geometries, and so they are insufficient for general application. In order to maintain the straightforward applicability of these solutions while improving their accuracy, subsequent researchers [61] have added empirical modifications to these relations. Empirical corrections, however, are typically not widely applicable because they are developed from a particular set of conditions. Modern computation fluid dynamics (CFD) has allowed theoretical solutions to be obtained that include many factors that are neglected in the analytical solutions, and it demonstrates the inaccuracy of the available corrections (unmodified integral solutions between 5 and 25% low and the empirically modified corrections about 10% low [62]). Therefore, simply applying a correction factor to the measurements of a conventional heat flux gauge is a flawed approach to the problem of thermal perturbations, so a means of eliminating these perturbations is sought.

The only way to eliminate thermal perturbations entirely is to use a gauge consisting of the material into which it will be installed. By embedding either conventional or eroding thermocouples within a plug of the wall material, the transient temperature profile within the material can be measured, and then the recorded data can be used as the input to a thermal model of the wall material to deduce the surface heat flux. This overall procedure is identical to that utilized for slug calorimeters, but as the lumped capacitance approximation is typically invalid for materials used in the combustion chamber and nozzle walls due to a combination of their insulating character and the extreme heat fluxes, the data reduction method becomes considerably more complex.

2.4.2. Inverse Heat Transfer Analysis

The solution of direct problems involves solving a problem's governing ordinary or partial differential equation with known parameters and boundary conditions to determine time- and space-dependent variables [63]. Inverse problems, on the other hand, use discrete measurements of these variables in an effort to ascertain the parameters or boundary conditions of the problem. Specifically, the inverse heat conduction problem uses one or more measured temperature histories taken at known locations within a thermally conductive material to estimate the heat flux history at one or more of its boundaries [64]. In this way, all methods that deduce heat flux via internal temperature measurements are forms of the inverse heat conduction problem [57], including slug calorimetry. The solution to the inverse problem for the slug calorimeter is one of the few that has a closed-form solution, due to its approximation of zero-dimensionality. Higher-dimensional problems, however, are typically solved using the well-known method of least squares [65], which is sufficiently computationally intensive to require the use of a computer. If a mathematical model and a set of measurements exist for a given problem, then the inverse problem can be solved.

For heat flux determination problems in which the material surface erosion is negligible, this model is simply the heat conduction equation, which may be solved analytically for some linear cases or via numerical methods for nonlinear cases. In SRMs, one example of this type of problem was that of Lindsey and Guster [66], who utilized eroding thermocouples to measure the temperature on the inner surface of a graphite nozzle to determine an “overall” film coefficient for the flow through the nozzle. Least squares regression was not employed for the solution to this problem, but rather a simplified analytical solution resulting in an implicit equation for the film coefficient, which was iterated until it converged. Price et al. [67] utilized eroding thermocouples to measure not only the inner surface temperature of a molybdenum nozzle but also the outer surface temperature. These temperature measurements were input to a numerical conduction code, which estimated the heat flux, but the details of the inverse method were not given.

For ablative materials, the surface erosion is, of course, significant, with many different thermochemical processes occurring in the pyrolysis zone and char layer, meaning that conduction alone is insufficient to model the thermal response of an ablator. Nevertheless, if these processes are modeled and their key parameters are known, the total surface heat flux can be estimated via an inverse analysis. For the case of empirical heat transfer estimation (Wernimont [32]), carbon-phenolic nozzle materials with empirically-determined thermal properties were fired in a subscale SRM, and their final erosion depth and char layer thickness were determined post-test. A value of the ratio of convective heat transfer coefficient to free stream constant-pressure specific heat, h/c_p, was guessed initially, then the Aerotherm Charring Material Ablation code (CMA) was run with that material's thermal properties to calculate the final erosion of the material. The value of h/c_p was then varied until the calculated erosion matched the measured value. Another example of the inverse method as applied to ablative material erosion occurs in Baker et al. [51], where thermocouples are installed in plugs of ablative material that are inserted into corresponding holes in the ablator forming the wall of a SRM nozzle. CMA is once again used to model the thermal response of the ablative material. In this case, however, the input histories of surface temperature and surface recession were adjusted iteratively until good agreement between the measured and calculated in-depth temperature histories was achieved. While neither procedure implements least squares analysis, they employ the same logic and result in an estimated heat flux history derived from a SRM environment.

2.5. Thermal Radiation Flux Measurement

Given the complexity of ablative material decomposition and the many and multifarious mechanisms by which it accommodates the incident heat flux, it is important not only to know the total heat flux but to know the contribution of each mode of heat transfer to the total flux. For non-metallized solid propellants, convection is the dominant means of heat transfer in the SRM due to the narrow-spectral-range radiative emissions of the purely gaseous combustion products, which may generally be neglected. In metallized propellants, however, radiative heating due to the presence of molten Al_2O_3 particles in the combustion products, which absorb, emit, and scatter broadband radiation, can account for as much as 100% of the total heat transfer to the internal insulation in certain regions of the SRM [68]. One method of distinguishing between the convective and radiative components of the total heat transfer involves insulating a heat flux sensor from convection by positioning it behind an infrared-transmissive window and comparing its flux measurements to those of a total heat flux gauge that is also mounted in the SRM. This is the approach favored by Brookley [54] and Baker et al. [51], which both utilize Gardon gauges as radiation detectors.

Given that a significant fraction of typical metallized SRM products (~30% by mass) exists in the form of liquid droplets, a maintaining a clean window and viewing aperture is a paramount concern. Both Brookley [54] and Baker et al. [51] accomplish this task by injecting cold, inert gas (nitrogen, specifically) into the annular region around the copper gauge body, where it serves not only to prevent particles from entering the radiometer cavity, but also to act as a coolant for the Gardon gauge's copper heat sink. Schematics of each of these radiometers are shown in Figure 2-5. Though the purge gas flow directly over the window is handled differently by each gauge, it enters the main flow channel essentially normal to the direction of the combustion product flow in both. Most importantly, both studies report that their respective configurations successfully maintained a clean window during rocket motor firings. Baker et al. [51] noted that some alumina slag accumulated on the sidewalls of the radiometer cavity for a radiometer installed in the throat of an ablative nozzle, though no slag was present in the cavity of a radiometer installed in the exit cone of the nozzle. The unusual behavior of the radiometer at the throat location, particularly when compared to the measurements of the well-behaved exit cone radiometer led Baker et al. [51] to conclude that slag was accumulating in the radiometer port to a sufficient degree to restrict the aperture of the radiometer but would periodically break off and be ejected out of the port by the pressure from the purge flow. The radiometer designed by Brookley [54] is more likely to collect alumina particles than those in Baker et al. [51], due to the fact that it is not located in the nozzle, but rather in the combustion chamber, where the alumina particles have a much lower velocity and, thus, less streamwise momentum. Nevertheless, Brookley [54] reports no low readings due to particle deposition or slag flow constriction of the viewing angle, the latter due in part to the fact that this radiometer was mounted flush with the surface of the ablator, rather than being recessed below it.

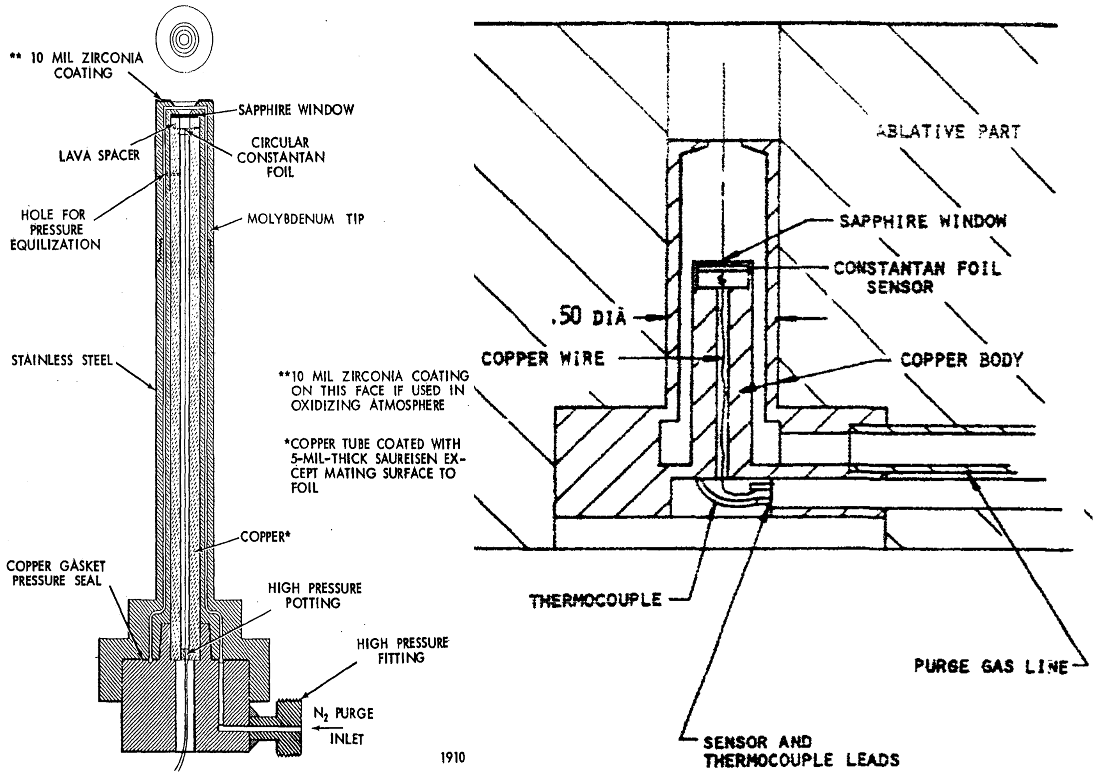

Figure 2-5 Schematics of the radiometers of Brookley [54] and Baker et al. [51]

The appropriate purge gas flow rate for the radiometer was determined by trial and error by Brookley [54], who investigated the impact of the purge flow rate on the measured radiative flux by stopping the purge flow mid-firing in two tests: one utilizing metallized propellant and the other utilizing non-metallized propellant. A momentary increase in measured radiation would suggest that the purge gas was indeed cooling the local product flow causing decreased readings. Instead, the reading immediately began to decrease as particles covered the window. In another metallized propellant firing, the purge flow rate was significantly increased, and it was found that the measured radiation was about 20% lower than in prior tests with the same measured total heat flux; therefore, care must be taken to select a purge flow rate that is adequate to maintain a clean window, but sufficiently small to be non-intrusive. Baker et al. [51] determined the purge flow rate for their radiometer based on cooling requirements for the gauge body rather than particle ejection requirements but states that the system functioned perfectly and did not affect the operation of the radiometer.

Chapter 3 Method of Approach

3.1. Design of the Subscale SRM

3.1.1. Solid Propellant Grain

The subscale SRM shown in Figure 1-1, was designed and fabricated specifically for the testing of ablative material samples for SRM internal insulation, and it consists of five main regions: the driver grain, the transition section, the instrumentation section, the test section, and the nozzle. The driver grain consists of highly-aluminized solid propellant, the products of which are used to degrade the ablative material sample located in the downstream test section. In order to provide several seconds of quasi-steady ablation behavior after the completion of transient processes in the material samples, the subscale SRM was designed to use end-burning propellant grains, which provide long-duration (~21 sec) firings, as well as a neutral burning character and a spatially uniform product gas flow, both characteristics that reduce the confounding factors in the experiment. The neutral burn character of the grain allows the pressure to remain practically constant throughout the duration of the firing, while the uniform product gas flow allows the flow in the test section to be essentially two-dimensional. The propellant formulation utilized in the end-burning grains is the same used in the RSRM, TP-H1148, whose formulation is given in Blomshield et al. [69], so that conditions are as similar as possible to the real application. Long firing durations are neither required nor desirable for verification of the operation of the subscale SRM's components and instrumentation, as the failure of a component could have catastrophic consequences over a long firing duration. Therefore, a center-perforated (CP) propellant grain configuration is utilized to provide short-duration (~3 sec) firings used to validate the function and performance of the various components and instruments employed in the subscale SRM. The CP grains were composed of ASRM propellant, a formulation developed (but ultimately abandoned) by Aerojet as a replacement for TP-H1148 with an HTPB (rather than PBAN) binder and a higher aluminum content (19 wt % vs. 16 wt %) [70]. With its larger burning surface area, the CP grain generated a much larger mass of products compared to the end-burning grain for a particular pressure, so the velocities, and, thus, heat transfer rates, in the motor were significantly greater for the short-duration firings than for the long-duration firings. The higher aluminum content of the ASRM propellant also caused a concomitant increase in the fraction of condensed-phase products in the flow.

3.1.2. Flow Channel

Immediately downstream of the driver grain is the transition section, which turns the flow from 2D axisymmetric to 2D planar. The design of the length of this section involved the balancing of two opposing principles: smoothness of transition, which argues for a long transition section, and minimal heat absorption, which argues for a short transition section. A fast contraction of the flow can cause the flow to separate and, consequently, require a long constant-area section downstream of the contraction for a two-dimensional flow to be established. In addition, the flow non-uniformities introduced by this contraction can cause local regions of relatively low or high wall heat fluxes, which could unduly stress the wall's constituent materials. On the other hand, all of the wall materials located upstream of the ablative material samples are absorbing energy from the flow, which reduces its sensible enthalpy as it proceeds downstream. Therefore, the distance between the driver grain and the candidate ablative samples should be as short as feasible while providing a two-dimensional flow. A Fluent CFD simulation of the subscale SRM was performed to determine the flow field structure in the test section. In this simulation, the internal flow of the SRM was modeled as consisting of the gaseous components of ASRM combustion products at 4.14 MPa ($\gamma = 1.1$) and as turbulent employing the Spalart-Allmaras model. The 3D polyhedral mesh was sufficiently fine such that the maximum wall y^+ in the SRM test section is 40. Figure 3-1 displays the secondary (non-axial) velocity components on six different cross-sections of the flow channel in the test section. This plot demonstrates the uniformity of the flow over both the instrumentation as well as the ablative samples as the in-plane velocity components are practically zero except in the upstream flow transition and at the very end of the ablative samples, where the flow is beginning to be contracted into the nozzle. Figure 3-2 displays the width-wise velocity profiles at five different axial locations, so that the boundary layer thickness may be determined at these locations, which are denoted by the colored lines overlaid on the cross-sectional view on the right of the figure. The colors of the velocity profiles on the velocity vs. position plot correspond to the colors of these position markers. The boundary layer remains relatively thin (occupying less than 7.0% of the width of the flow channel) throughout the test section until the flow is accelerated by the nozzle convergence, demonstrating that flow is not fully developed. However, these results were derived using the mass flow rate of the

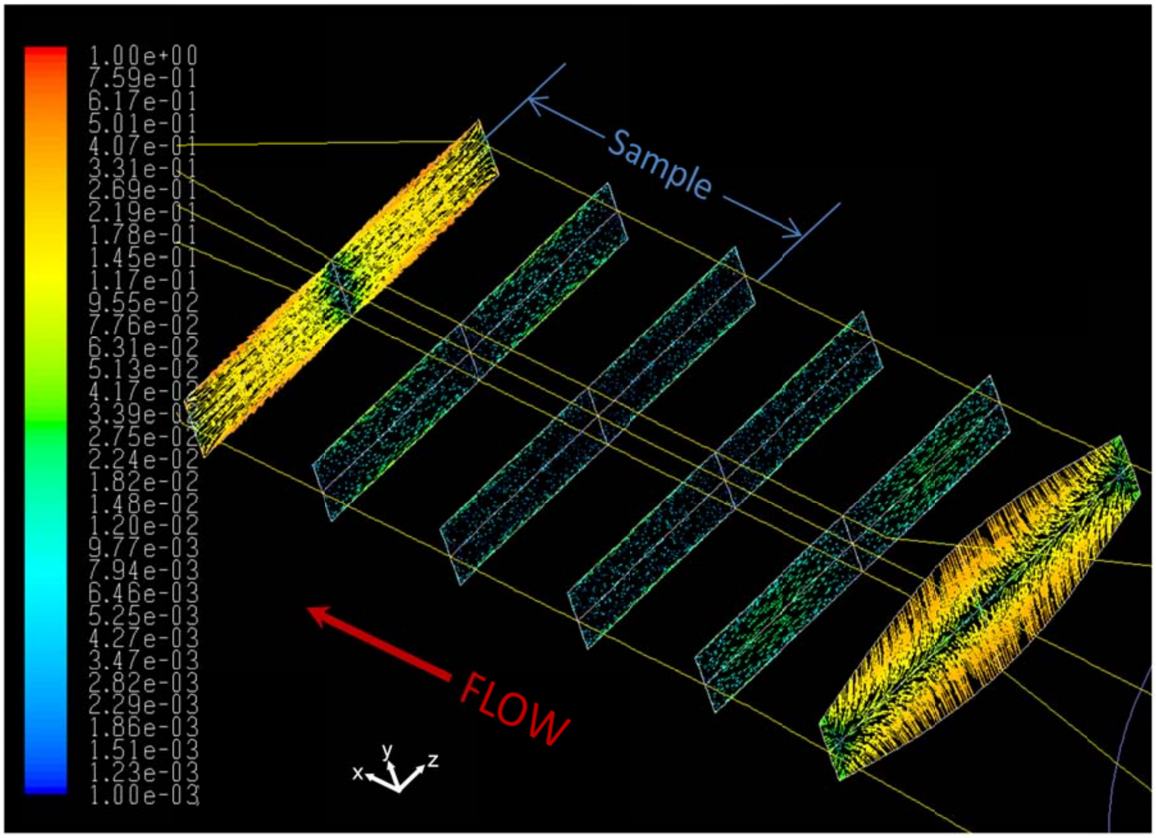

Figure 3-1. CFD simulation results – secondary velocity components in the subscale SRM test section

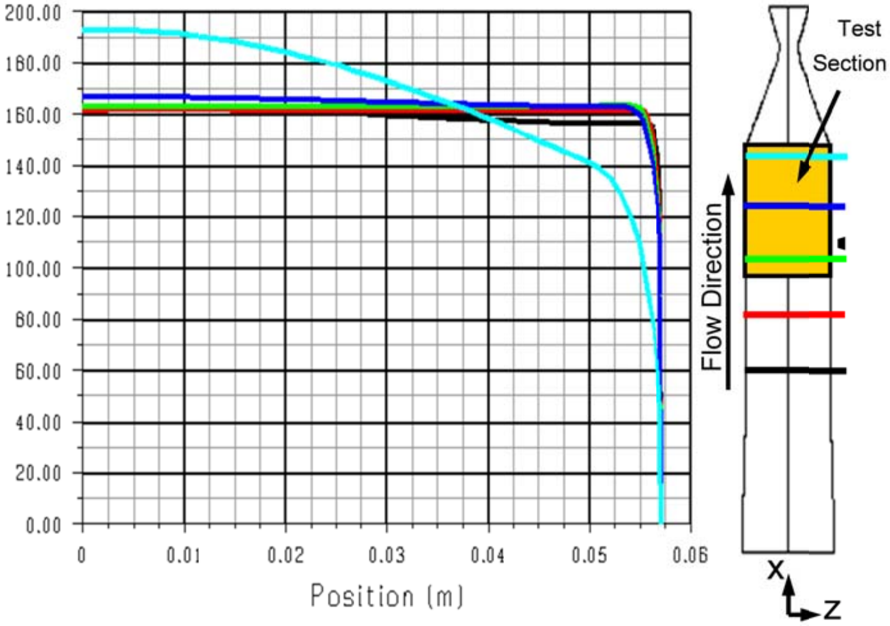

Figure 3-2. CFD simulation results – width-wise boundary layer development

CP grain, rather than that of the end-burning grain; therefore, for the long-duration tests, the boundary layer will be thicker by an amount that may be determined via theoretical arguments. For a turbulent external boundary layer over a flat plate, the following relationship between the momentum thickness and the Reynolds number can be derived [71]:

$$\frac{\delta}{x} = 0.036\,\mathrm{Re}_x^{-0.2} \tag{3.1}$$

where δ represents the local momentum thickness of the boundary layer, x is the axial coordinate, and Re_x is the local Reynolds number. Since Reynolds number and mass flow rate are directly proportional to the free-stream velocity, and the ratio of the dynamic viscosities of the two product gas flows is practically unity, the following relationship is derived:

$$\frac{\delta_2}{\delta_1} = \left(\frac{\dot{m}_1}{\dot{m}_2}\right)^{0.2} \tag{3.2}$$

where $\dot{m}$ represents the propellant mass flow rate. Since the ratio of the CP grain to the end-burning grain mass flow rates is 7.7 at the design pressure of 4.48 MPa, the boundary layers in the subscale SRM employing an end-burning grain will be 1.5 times thicker than those determined from the simulation. This does not affect the conclusion that the velocity profile may be approximated as uniform in the width direction as the boundary layers still occupy less than 11% of the width of the flow channel. The height-wise velocity profiles are shown in Figure 3-3, and, as expected, were developed to approximately the same thickness as their width-wise counterparts. The thicknesses of these boundary layers may also be calculated for the case of an end-burning grain via Equation (3.2), with the resulting maximum thickness of 6.1 mm being insufficient to cause the boundary layers to merge in the 19-mm-high channel, allowing them to be treated as external flat-plate boundary layers. This boundary layer thickness is, however, sufficient to cause the apparent free-stream velocity to increase with downstream distance, so that the boundary layer will grow more slowly in the streamwise direction than predicted from Equation (3.2).

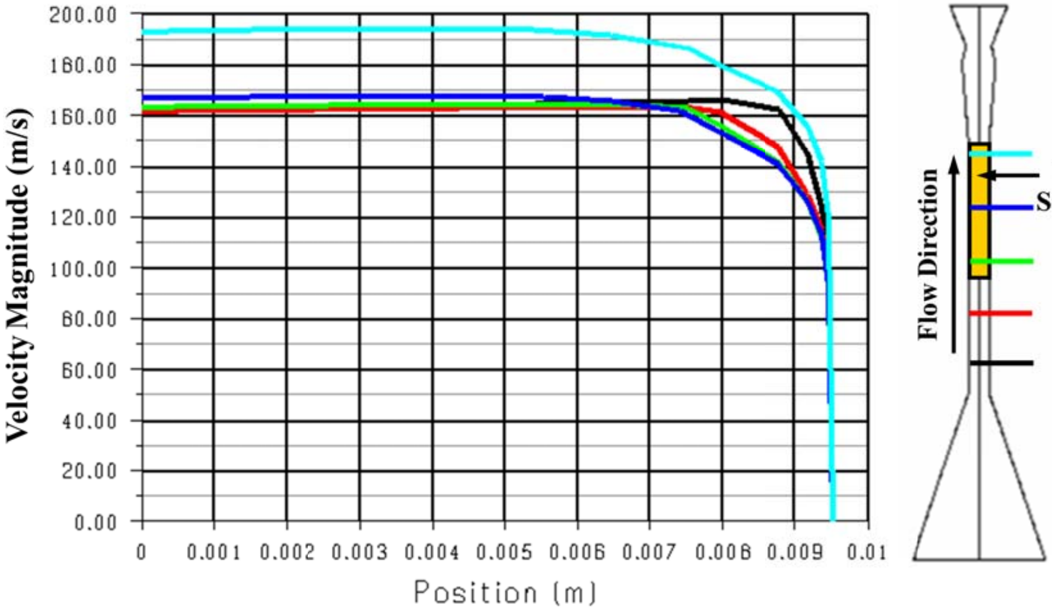

Figure 3-3 Height-wise boundary layer development

The above CFD calculations utilized a uniform velocity distribution at the entrance to the transition section, which is a good approximation of the flow field for the end-burning grain configuration, but not for the CP-grain configuration. Another CFD model was created that included the CP-grain geometry upstream of the transition section and introduced the combustion product mass flow normal to the burning surfaces of the grain. From this simulation, it was apparent that the flow in the test section of the subscale SRM was decidedly non-uniform for the CP grain configuration in the width direction; nevertheless, this effect seems minimal in the height direction likely due to the magnitude of the flow acceleration from the transition in that direction compared to the width direction.

As shown in Figure 3-4, which is a view of the velocity field in the transition region upstream of the test section, the acceleration of the flow in the height direction caused a vena contracta effect at the leading edge of the instrumentation section. This effect, however, is completely dissipated approximately one channel height (19 mm) downstream, so the ablative material samples and the heat flux gauges are unaffected by the flow transition.

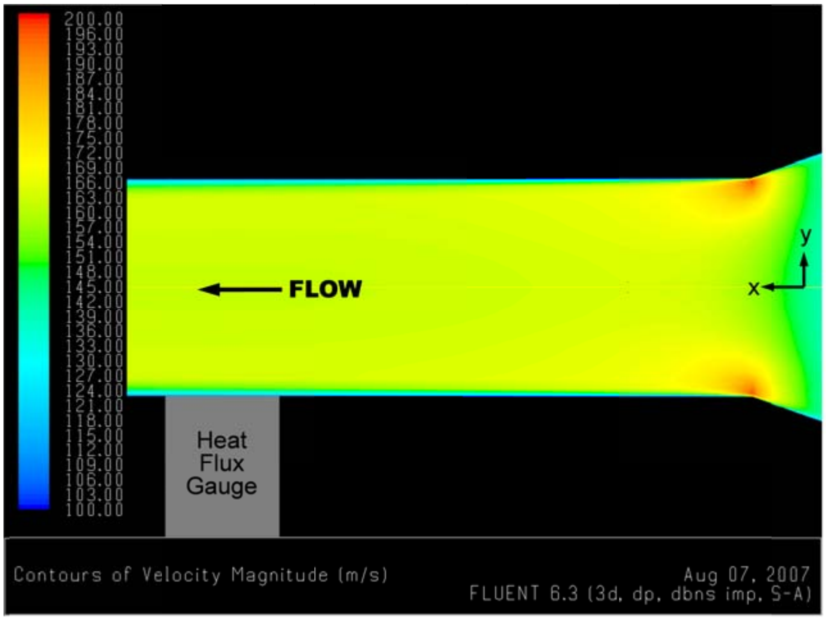

Figure 3-4 Velocity magnitude at entrance of instrumentation section

The instrumentation section, which resides directly downstream of the transition section, houses both the total and radiative heat flux gauges, so the heat transfer environment in this region must be similar to that in the test section, where the ablative material samples reside. Thus, the geometry of the flow channel in the instrumentation section is identical to that in the test section. The choice of configuration and materials in this region was governed by the requirements of the total and radiative heat flux gauges and will be discussed in detail Sections 3.4 and 3.5, respectively.

The ablative material samples that are to be tested in the subscale SRM are situated in its test section, where X-ray translucent windows (aluminum outer and polycarbonate inner) provide optical access for RTR equipment to observe and record the in-depth degradation behavior of the samples. While the ablative samples themselves provide thermal protection for the top and bottom of the flow channel, the sides are insulated, as in other regions of the motor, by graphite. The samples are also instrumented with subsurface temperature sensors, which are plugs of ablative material of interest into which micro-thermocouples have been embedded to measure the in-depth temperature history of the material during its decomposition.

The nozzle transition, located directly downstream of the test section, converts the flow back from 2D-planar to 2D-axisymmetric for entrance into the nozzle. The flow area decreases through this region, thus, the nozzle transition also functions as the nozzle entrance region. This part is also made of graphite.

3.1.3. Water-cooled Nozzle

The nozzle itself is subject to the highest heat-transfer rates of any part of an SRM, as it experiences the highest mass flux of combustion products of any part of the SRM. Since it is desirable to maintain a constant pressure in the motor throughout the duration of a firing to minimize experimental variables, an actively cooled nozzle design was chosen for the subscale SRM, as significant throat erosion is inevitable with uncooled graphite or ablative nozzles particularly for long-duration firings. As shown in Figure 3-5, the nozzle is essentially a thin-walled copper tube situated in the center of an aluminum boss, between which there exists only a small annular space. Water is injected tangentially into this annular space by four injectors (shown in Figure 3-6), creating a strongly swirling flow. The small size of the annulus and the swirl of the flow generate large momentum gradients, which, in turn, enable high heat-transfer rates from the nozzle wall into the water. The nozzle wall was made as thin as mechanically feasible to keep peak wall temperatures as low as possible. If heat-transfer rates from the product gas flow to the nozzle are sufficiently high, flow boiling will be induced on the cooled side of the nozzle, which removes heat rather effectively due to the high latent heat of vaporization of water. Nevertheless, if vapor quality of the water approaches unity (becoming or approximating film boiling) anywhere within the flow annulus, the cooling capacity of the water flow will decrease sharply due to the lower thermal diffusivity of the vapor, causing failure of the nozzle. Therefore, four injectors were employed to eliminate low-velocity recirculation zones in the annular space to avoid local dry-out.

Analytically determining the mass flow rate of water required to adequately cool the nozzle is practically impossible, as widely-applicable heat-transfer correlations do not currently exist for nozzles in metallized SRMs. The most widely used correlation for determining film coefficients in rocket nozzles is that of Bartz [72], which is insufficient to describe the effects of the condensed-phase products present in the exhaust of metallized SRMs [73]. In fact, when the Bartz correlation is applied to metallized SRM

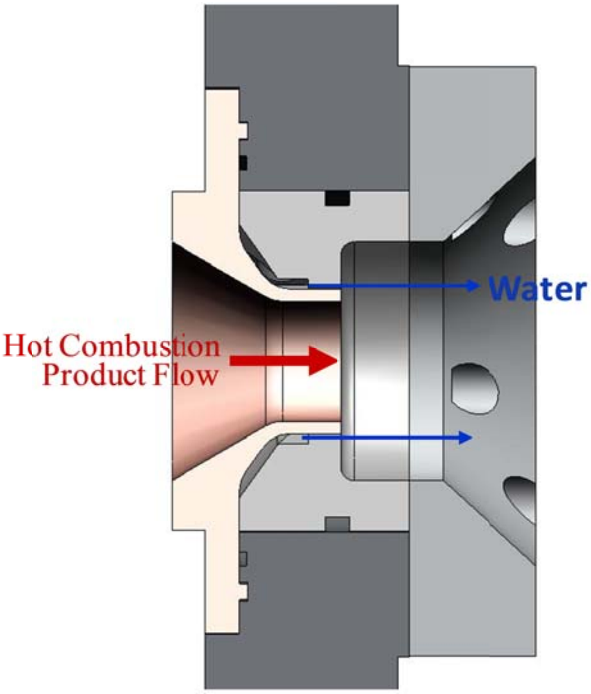

Figure 3-5. Side cross-sectional view of water-cooled nozzle

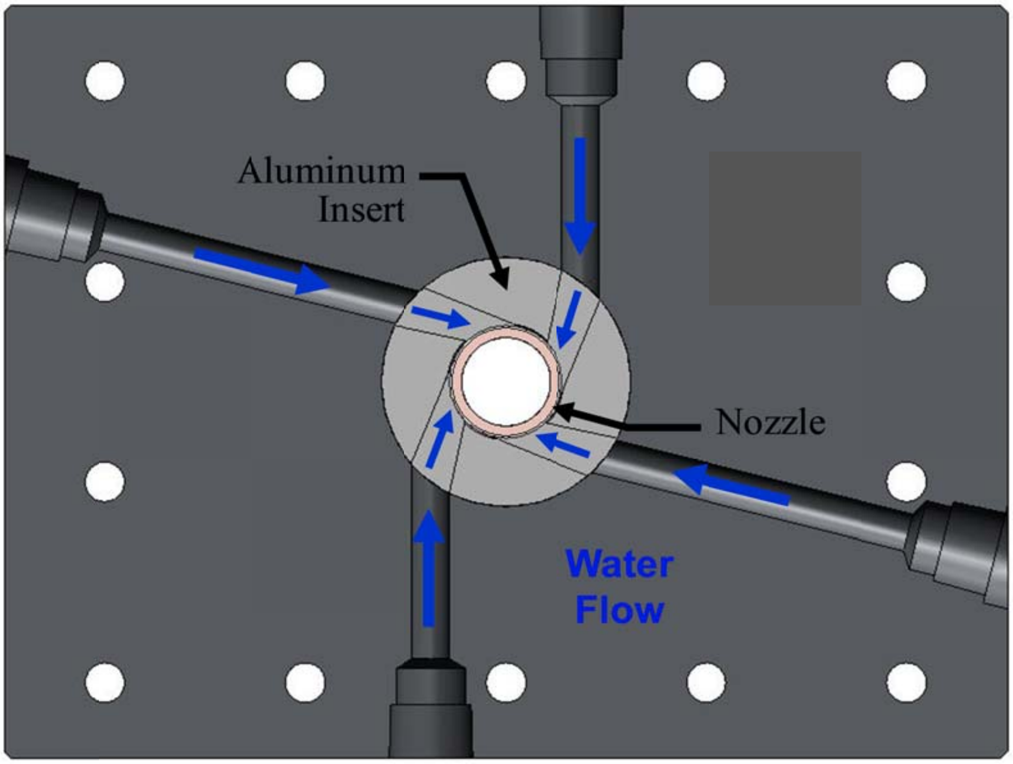

Figure 3-6 Rear cross-sectional view of water-cooled nozzle

nozzles, it has been shown to under-predict heat-transfer rates by as much as a factor of two [73]. Nevertheless, the Bartz correlation was incorporated into the design process for this nozzle to provide an order-of-magnitude-type assessment of the required mass flow rate of water. The temperature distribution through the nozzle wall was calculated for given temperatures and film coefficients via a one-dimensional, steady-state solution of the heat conduction equation for the nozzle wall with Bartz correlation supplying the convection boundary condition to the gas side and a simple internal flow convection correlation supplying the boundary condition to the water side. While several effects were not included in this rudimentary analysis, such as swirl flow and flow boiling on the water side, including this additional complexity was considered superfluous due to the tremendous uncertainty in the calculation of the gas-side heat-transfer rate. In this analysis, the mass flow rate of the water was iterated until the maximum temperature calculated through the nozzle wall was suitably low to allow the copper to preserve sufficient mechanical strength to avoid failure under operating conditions. The mass flow rate of cooling water required to maintain survivable temperatures in the nozzle was near the maximum of the capabilities of the available water delivery system. Unfortunately, resources were not available to over-design the water cooling system to accommodate the uncertainty in the gas-side heat-transfer rate to the nozzle, so the available system was configured to produce its maximum water flow rate for the series of test firings using the CP-grain configuration.

The water flow in the nozzle cooling system was driven by compressed nitrogen supplied by standard industrial cylinders pressurizing a 130-L water reservoir consisting of four repurposed carbon dioxide cylinders. The reservoir pressure was controlled using a pressure-reducing regulator (Tescom Part No. 44-1317-2122-056), whose outlet pressure was set to 10 MPa for the CP-grain-configured firings. Firings of the subscale SRM proved the efficacy of this nozzle-cooling system, as no discernible erosion was detected in the throat of the copper nozzles following the firings.

The nozzle throat size for each type of propellant-grain configuration was determined by varying the throat size parameter in a zero-dimensional interior ballistics code until the desired pressure-time behavior was calculated. For the CP-grain configuration, the design chamber pressure was 4.14 MPa with a maximum of 4.48 MPa, values which broadly correspond to chamber pressures in the RSRM. Since the diameter of the center port of the CP grain increases as it burns, the burning surface area, and, thus, the chamber pressure is not constant in time. Nevertheless, the ends of this particular grain are not inhibited, so the grain also shortens as it burns, creating a pressure-time profile that is essentially neutral, with pressure increasing to a maximum at mid-burn before decreasing to burnout. A throat diameter of 21.8 mm was determined via the interior ballistic code calculations to produce an average pressure of 4.23 MPa and a maximum pressure of 4.35 MPa for the CP-grain configuration; however, the molten alumina in the solid-propellant combustion products freezes on the surface of the cold copper nozzle and forms an insulating layer on the nozzle interior, which grows until the layer's surface temperature is sustained at the melting temperature of the alumina (2327 K). This layer decreases the effective cross-sectional area of the nozzle; therefore, boring the nozzle throat to 21.8 mm results in chamber pressures in excess of that predicted by the interior ballistics code. As the thickness of this alumina layer in dynamic equilibrium with the combustion product flow was indeterminate prior to testing due to the uncertainties in estimating the steady-state heat transfer through the nozzle wall, early CP-grain-configured firings of the subscale SRM were performed with the nozzle bored to 21.8 mm in order to ascertain this value. Post-firing measurements of the frozen alumina layer remaining on the interior of the nozzle revealed an average thickness of 0.3 mm; therefore, the nozzle throat for the CP-grain configuration was bored to 22.4 mm for the remaining CP-grain-configured firings.

Figure 3-7 displays the chamber pressure history computed using the interior ballistics code along with those measured from two CP-grain-configured firings: one using a nozzle whose throat was bored to 21.8 mm and another where the nozzle throat was bored to 22.4 mm. While some variation exists between the calculated and measured pressure histories at early times due to the fact that the zero-dimensional interior ballistics code does not model flame spreading processes or the process of alumina accretion on the nozzle throat, it is evident from Figure 3-7 that accounting for the alumina layer by over-boring the nozzle throat produces good agreement between the calculated and measured pressure histories. In fact, time-averaging the 22.4-mm measured pressure history over the firing duration results in the same 4.23-MPa average pressure as that computed from the 21.8-mm calculated pressure history. Therefore, the zero-dimensional interior ballistics model validated its capability as a nozzle design tool, provided that the alumina layer thickness was accurately estimated. In addition, the agreement between the shapes of the calculated and measured pressure histories demonstrate that the cooled-nozzle design does, in fact, establish a near-constant nozzle-throat area for the duration of these CP-grain-configured subscale SRM firings.

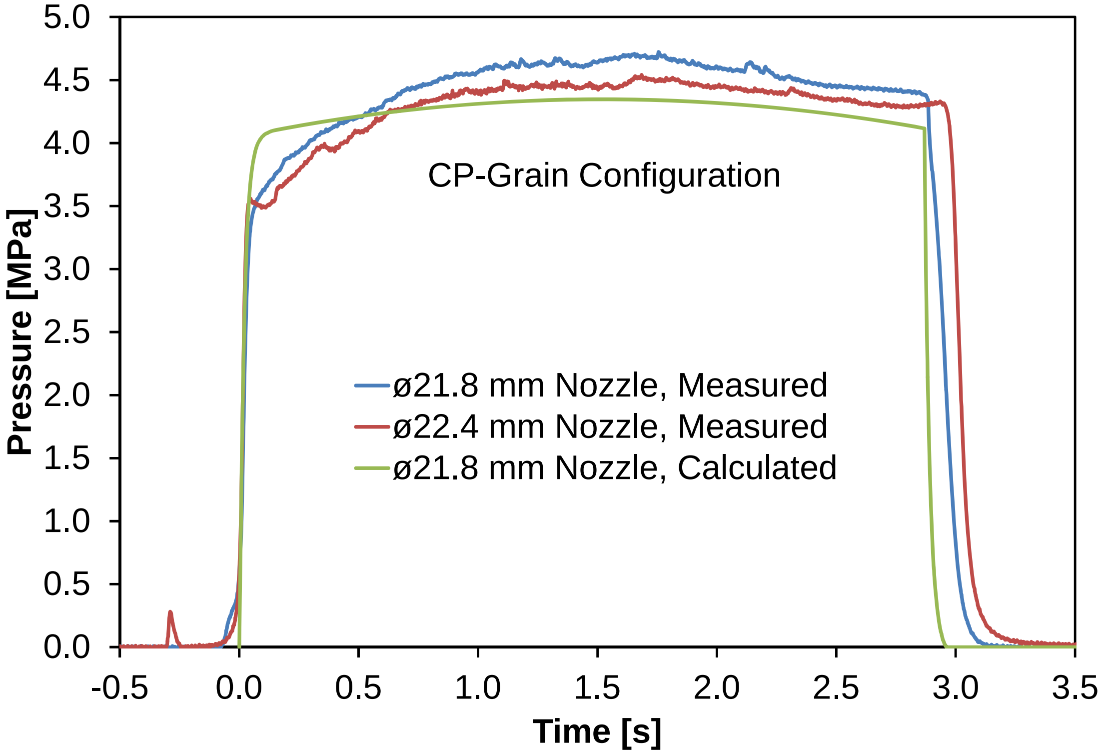

Figure 3-7. Chamber pressure history computed using the interior ballistics code and those measured from two CP-grain-configured firings using different nozzle diameters

The reduced burning surface area of the end-burning solid propellant grains compared to that of the CP grains requires a concomitantly smaller nozzle throat area to maintain the same average chamber pressure. Due to the similarities in the composition of the two different types of solid propellant grains, as well as their desired operating pressures, the heat transfer coefficient to the nozzle interior as calculated from the Bartz correlation for the end-burning grains is only 6% greater than that calculated for the CP grains, a fact indicating that the steady-state thickness of the alumina layer will be perhaps slightly thinner than that present in the CP-grain-configured firings. However, in order to provide additional cooling capacity for the nozzle-cooling system, the width of the water flow annulus around the exterior of the nozzle was kept the same for the end-burning-grain configuration as for the CP-grain configuration, even though the outer diameter of the nozzle became considerably smaller. Maintaining the same annular gap width between the two configurations greatly decreases the cross-sectional area for the water flow around the nozzle in the end-burning configuration, which, for a given pressure in the water reservoir, greatly accelerates the axial component of the water velocity vector around the nozzle, providing an increase in the heat transfer coefficient on the water side. The more-efficacious heat transfer on the water side of the nozzle was expected to increase the thickness of the alumina layer by decreasing the steady-state temperature of the interior surface of the copper, and, thus, requiring a greater thickness of alumina in order to maintain the inner surface of the alumina at its melting temperature. In lieu of reasonably precise knowledge of the heat-transfer rate from the combustion products, the alumina layer thickness was assumed to be identical to that measured from the CP-grain-configured firings (0.3 mm) and added to the diameter for which the interior ballistics code calculated the target pressure (8.3 mm, 4.48 MPa) to generate the appropriate diameter to which to bore the nozzle (8.8 mm). This configuration and its resultant chamber-pressure history was tested by firing the subscale SRM with a shortened end-burning propellant grain designed to provide five seconds of operation, in order to limit the extent of the damage in the event of a nozzle failure. In this firing, the nozzle survived, but the alumina layer grew much thicker than anticipated, resulting in a chamber pressure history that monotonically increased from ignition to burnout, which occurred at a peak pressure of 6.30 MPa. In order to reduce the alumina layer thickness by increasing the nozzle temperature, the mass flow rate of the cooling water was decreased incrementally by reducing the water reservoir pressure in each of nine additional short-duration end-burning-grain-configured firings (from 9.73 MPa in the initial firing to 1.74 MPa in the final firing); nevertheless, the alumina layer thickness proved insensitive to the water flow rate, as the maximum chamber pressure measured in the last test of this series was greater than that measured in the first, and not even a rough correlation was found between the developed chamber pressures and the reservoir pressure. Therefore, the nozzle was simply bored to a larger diameter (9.3 mm) to reduce the maximum chamber pressure by accounting for the observed thickness of the alumina layer (approx. 0.8 mm), and the reservoir pressure was set to a value near the middle of the tested range (5.34 MPa).

3.2. Real-Time X-ray Radiography

For this study, real-time X-ray radiography (RTR) was used as a means of peering into the subscale SRM chamber during operation in order to examine the ablative degradation of the ablative material samples in a time-resolved manner. As shown in Figure 3-8, X-rays produced by the X-ray source (YXLON Y.TU 320-D03) penetrate the SRM through two pairs of X-ray translucent (aluminum outer and polycarbonate inner) windows, then are intercepted by the image intensifier (Precise Optics PS62VHR, manufactured by Thales as TH 9464 VHR), which, in conjunction with a Silicon Video® 1281 CMOS camera, converts the received X-rays into grayscale digital images. As the X-rays pass through the constituent materials of the subscale SRM, some are absorbed or scattered due to their interaction with the atoms comprising these materials, reducing the intensity of the X-rays striking the image intensifier relative to that that would occur in the absence of any intervening media. The magnitude of the attenuation of the X-rays traveling through a particular medium is dependent primarily on the density of the material and the path length of the X-rays through the material, as both factors increase the opportunity for absorbing and scattering interactions with the material's constituent atoms. Therefore, due to the two-dimensional geometry of the SRM test section, contrast in the X-ray images is provided primarily by means of density gradients between and within the ablative material samples in the SRM test section. This contrast mechanism makes X-ray RTR an ideal means for inspecting the degradation of ablative materials in detail, as it is capable of distinguishing not only the material interface between the surface of the char layer and the combustion products, but also the interface between the porous, low-density char layer and the virgin material, as shown in Figure 3-9.

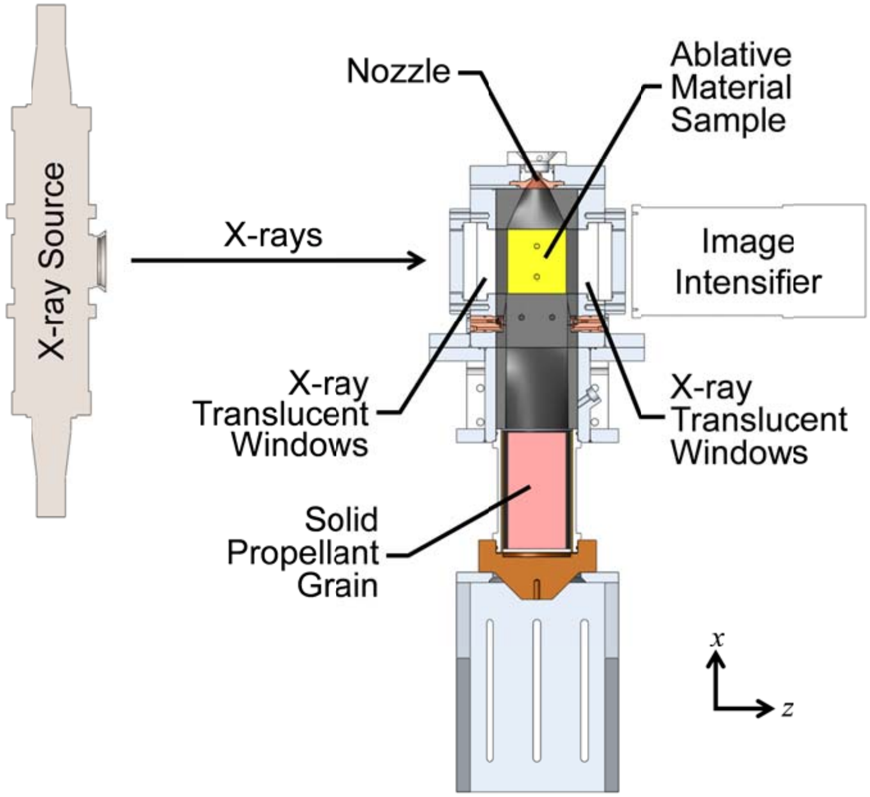

Figure 3-8. Cross-sectional view of the subscale SRM, X-ray source, and image intensifier

Figure 3-9 X-ray radiograph of charred ablative material

3.2.1. SRM Firing Procedure

Prior to an SRM firing, once the X-ray source and image intensifier have been aligned to the SRM test section, and the test section has been assembled, a small steel rod of known diameter is inserted into the center of the test section aligned with the flow direction and imaged with the X-ray system in order to provide a means of determining the resolution of the images during post-test image processing. After these scaling images are recorded, the steel rod is removed from the test section and the remaining preparations for the SRM firing are completed. The X-ray source is energized immediately before the firing sequence is initiated via a manual toggle switch. The initiation of the firing sequence triggers the image capturing software (as well as the data acquisition systems acquiring data for the pressure and temperature measurements), which immediately begins capturing X-ray images. Each time an image is captured, the time that has elapsed from the initial trigger to the moment of image capture is recorded, so that each image can be accurately synchronized to the other quantities (pressure, subsurface ablative material temperature, total heat flux, and thermal radiation flux) measured in the SRM, and so that the time resolution of the resulting X-ray videos is accurately known. Each SRM firing results in 3263 800 × 408 pixel, 8-bit, grayscale images captured at an average rate of 112 frames per second.

3.2.2. X-ray Image Enhancement

The raw images are enhanced using ImageJ open source software [74] in post-processing to decrease noise and increase the contrast among layers of differing material densities. The images captured prior to SRM ignition and after SRM burnout were removed from the image sequence under consideration so that the start of the image sequence would correspond to the ignition of the SRM. Next, due to distortion that inherently occurs near the edges of the image-intensifier-produced images, the raw images were cropped about their geometric center, as outlined with a yellow bounding box in Figure 3-10, resulting in 400 × 360 pixel images to be used for further processing. The brightness and contrast of the images was then manually adjusted to improve the ability of the analyst to distinguish among the virgin ablative material, char layer, and open flow channel. In order to reduce the noise in the images without utilizing a sharpness-compromising spatial smoothing filter, a moving average filter is applied in the time domain that averages together two images to create one image at the average capture time of the two averaged images. The resulting image sequence contained half of the initial number of images with half of the temporal resolution, but a considerable (1.4 ×) improvement in the signal-to-noise ratio of the images. The sacrifice in temporal resolution, however, was minimal as the resultant average rate of 56 frames per second equates to merely 18 ms between frames to observe events occurring on 100-ms timescales. Following the averaging step, another temporal filter, the Kalman stack filter

[75] , is applied to the image sequence to further improve the images' signal-to-noise ratio with little to no loss of temporal resolution. Finally, the initial angle of the ablative material surfaces relative to the image boundaries is measured and adjusted, if necessary, by rotating the image within the frame boundaries so that both ablative material surfaces are initially within 0.5° of parallel to the top and bottom image boundaries.

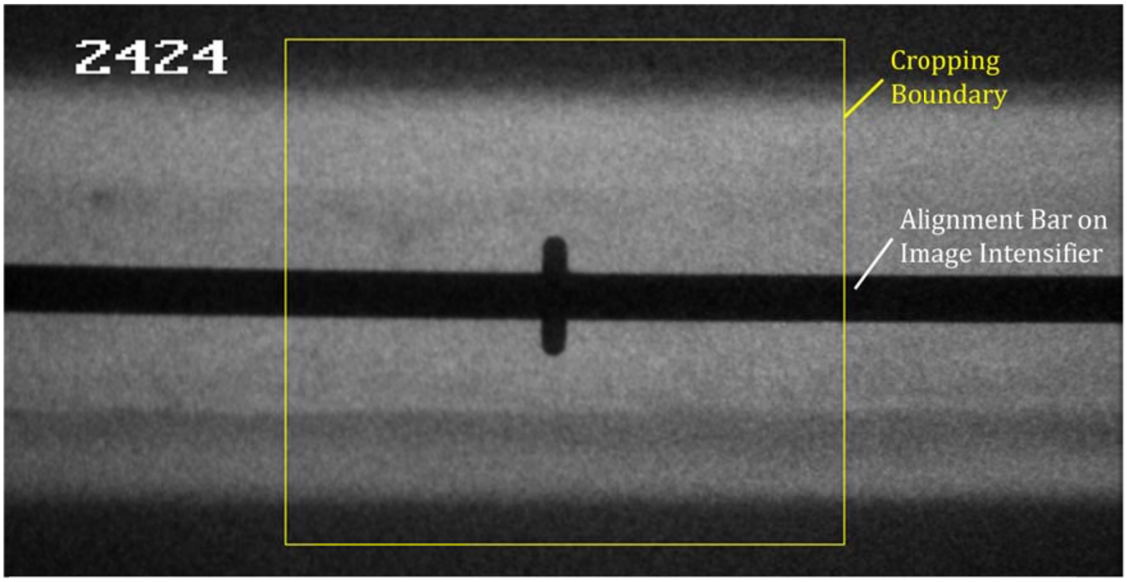

Figure 3-10. Raw X-ray image acquired from a subscale SRM firing showing outline of the region cropped during post-processing

3.2.3. *Edge Detection*

The location histories of the ablative sample surface and char-virgin interface were determined from the RTR images using the edge detection tool in National Instrument's Vision Assistant software. As shown in Figure 3-11, at three discrete streamwise (*x*) locations on each sample, two different edges, one corresponding to the char surface and the other corresponding to the interface between the char and the virgin material (char-virgin interface), were found by searching in the vertical (*y*) direction for the first instance where the gray level crosses a specified value. A simple threshold-based, rather than gradient-based method was employed because it does not require differentiation, and, thus, is less susceptible to noise in the image, providing a more stable discovery of edges with less false positives and negatives. The threshold values are specified independently for each surface and char-virgin interface and for each material used in each test, but are consistent among the various *x* locations for a given sample. Figure 3-11 displays one frame from near the end of Test #ABLMAT-34 with the edges found by the edge detection tool denoted by bright green boxes. For the purposes of tracking the movement of the different edges in time, *y* has been defined as the outward

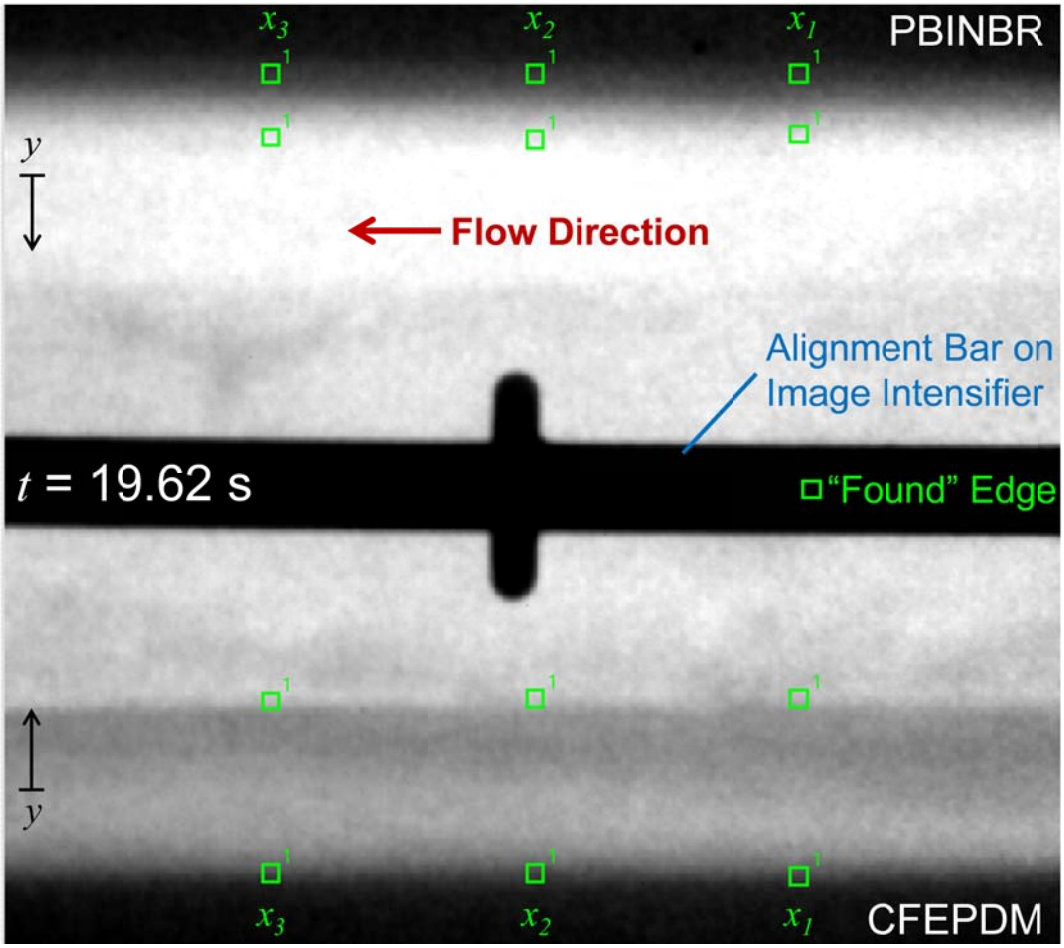

Figure 3-11. X-ray radiograph frame from Test #ABLMAT-34 showing the edges detected by the image analysis software including the definition and zero location of *y* for each material sample

normal of each sample, with the cross-bar on the y-direction arrow in Figure 3-11 denoting the $y = 0$ location for each sample, which corresponds to the sample surface location at the time of SRM ignition. The reported char layer thicknesses are merely the differences between the y locations of the char surface and the char-virgin interface at a given x locations.

3.2.4. Image Calibration and Edge Detection Uncertainty

In order to determine the true resolution of the X-ray images corresponding to a given SRM firing, the series of 16 pre-firing images of the known-diameter rod was cropped and enhanced in ImageJ in the same manner as the images taken during the firing, except that instead of applying a moving-average filter then the Kalman stack filter, all 16 images were simply averaged together to produce a single calibration image for each firing. The pixel width of the known-diameter rod was then determined from each calibration image using the gradient-based straight edge find tool in Vision Assistant, which was then divided by the rod diameter to determine the image resolution.

The uncertainty in the image resolution was calculated based on the uncertainty of the diameter of the steel calibration rod and on the uncertainty in the determination of the pixel width of the rod. The uncertainty in the image resolution calculated for the data from each of the subscale SRM firings is ±1.3% of the resolution. In order to determine the uncertainty in the reported y locations for edges found in the images, the uncertainty of the image resolution was combined with the uncertainty in the determination of the pixel location of the edge.

3.3. Subsurface Ablative Material Temperature Measurements

Since the controlling parameter of ablative degradation is the temperature of the ablator [49], a record of the transient internal temperature profile is essential to understanding and characterizing the ablator's thermal response. This record may be obtained by embedding thermocouples within the ablative material at specified distances from the surface; however, inserting a thermocouple into a material whose thermal diffusivity is much lower than its own, may distort the temperature field in its immediate vicinity [76]. In order to mitigate the intrusiveness of the thermocouple, two primary steps were taken: the size of the thermocouple itself was reduced to the smallest size that was robust and repeatable, and the thermocouple wires were installed perpendicular to the direction of the heat flow. Given the size of the ablative samples used in this experiment as well as other practical constraints, installing the thermocouples in this manner was untenable. Nevertheless, the errors in temperature measurement that occur due to installing thermocouples parallel to the heat flux lines in ablative materials have been shown to be as high as 800 K [77], so perpendicular installation is required. Therefore, three S-type (platinum/platinum-10% rhodium) thermocouples were instead installed in a small plug of the same type of material with the same fiber orientation, which was installed into a corresponding hole of the same diameter in the ablative material sample. The slight mechanical interference was desirable as the sample materials have elastomeric matrices, and so can compress slightly to eliminate any potential gaps between the sample and the plug.

The installed configuration is shown schematically in Figure 3-12, in which multiple thermocouples are installed at different distances from the exposed surface, and the portion of the wire that is installed perpendicular to the heat flow is more than the minimum 25 wire diameters suggested by the relevant ASTM standard [78]. The holes into which the thermocouples were installed were filled with shavings of material recovered from the drilling process to maximize thermal contact between the thermocouple and the sample, and to minimize the disturbance of the temperature field caused by the thermocouple installation. The thermocouple wires are coated with a thin layer of zirconia, in order to prevent them from making electrical contact with one another at any location other than the bead. Though the bead of each thermocouple was intended to be left bare to achieve the fastest possible time response, the surface tension of the zirconia adhesive caused some of the beads to become partially or fully coated by the adhesive as well.

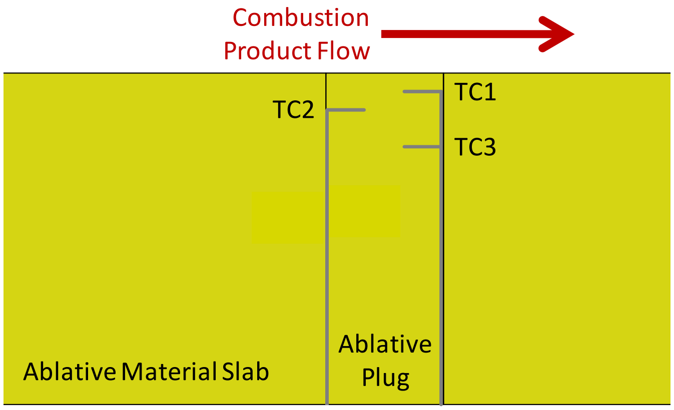

Figure 3-12 Detail cut-away view of installed ablative temperature sensor

High-resolution X-ray radiographs, like that shown in Figure 3-13, were taken of the thermocouple-instrumented cylindrical samples prior to their use in the SRM firings, so that the precise location of the thermocouple beads relative to the initial surface of the sample could be determined. The uncertainty in the measurement of the relative distance of the thermocouples to the front surface of the ablative cylinder was ascertained from the uncertainty in the X-ray image resolution and the uncertainty in determination of the relative pixel locations of the ablative cylinder front surface and the thermocouple bead center in the X-ray image. The uncertainty in the thermocouple depth was found to have an average of 3.3% of the measured distance and a maximum of 3.5% of the measured distance for all of the thermocouples used in the SRM firings.

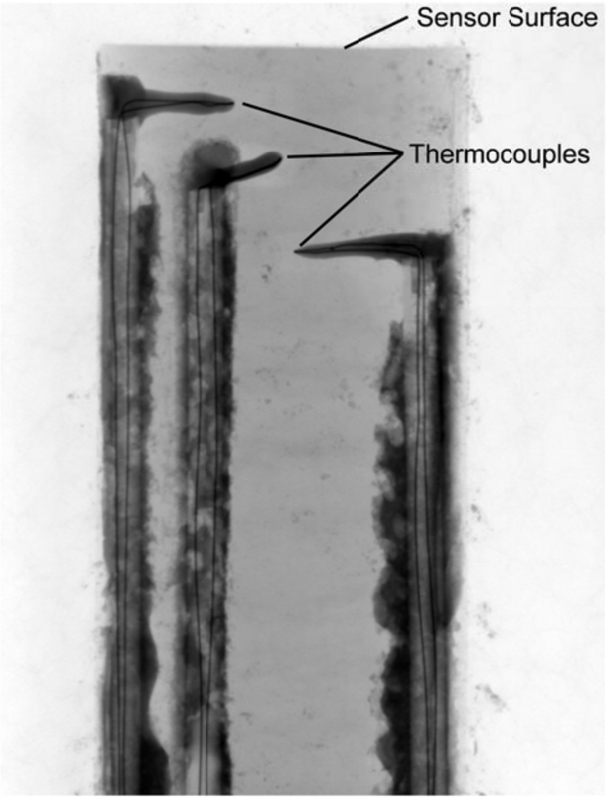

Figure 3-13. High-resolution X-ray radiograph of an ablative temperature sensor

In addition to determining the depth of the thermocouple beads in the samples, the radiographs were also used to determine which thermocouple beads were coated with a discernible layer of zirconia, and to estimate the thickness of that layer should it exist (unquantifiable inaccuracies are introduced into the coating-thickness determination by the fact that many of the thermocouples were not oriented parallel to the image plane). These layer thicknesses were used to calculate the time response of the embedded thermocouples via the method of Rabin and Rittel [79]. For this calculation, the coated beads were conservatively modeled as cylinders composed entirely of zirconia, while the uncoated thermocouple beads were modeled as platinum cylinders. The average time response computed for the center temperature of the thermocouple beads was 15 ms, while the median time response was 3 ms (that of the uncoated bead).

During installation of the ablative temperature sensors, the front surface of each sensor was aligned with that of its respective mounted ablative material sample simply by means of the installer's eye. In post-test examinations of the ablative material sample, it was impossible to distinguish between the ablative temperature sensor and the ablative material sample, and their respective char layers were fused together. Therefore, the temperature histories recorded by the ablative temperature sensors were considered accurate representations of the temperature histories of the ablative material samples at the in-depth locations determined from the high-resolution X-ray radiographs.

3.4. Total Heat Flux Gauges

In the initial phase of the design of the subscale SRM, the instrument of choice for measuring the total heat flux to the interior wall of the motor was a simple slug calorimeter. However, the slug calorimeter was soon eliminated as a potential heat flux gauge design due to its inherent vulnerability to both thermal perturbation and cross-conduction errors.

The only way to eliminate thermal perturbations entirely is to use a gauge consisting of the material into which it will be installed; however, this is not a tenable solution for this study, as it means the gauge must be constructed of ablative material. In such a case, the heat flux gauge would be identical to the ablative temperature sensors, with thermocouples embedded in a plug of ablative material that is installed in the ablative material sample. While the fabrication of such a gauge is clearly practicable, the method of deducing the surface heat flux from the subsurface temperature measurements is rather complex, as it requires the use of an inverse analysis coupled with a thermo-ablative code. One of the primary objectives of this research is to produce realistic erosion rate data to validate existing thermo-ablative codes: if the heat flux measurements used to validate these codes were the result of the application of another code, the validation procedure would serve only to compare the two codes to one another, rather than to compare one code to empirical data. Therefore, the objective of this project precludes the use of not only ablative materials, but any material that decomposes or undergoes surface reactions to a non-negligible degree during the course of a test firing, as modeling any complex process could introduce errors in the deduced heat flux due to the existence of simplifying assumptions or empirical constants present in the model. Thus, the demands of this project guarantee the presence of thermal perturbations in the total heat-flux measurements in the subscale SRM.

Fortunately, the perturbed heat-transfer coefficient decays quickly with downstream distance, so that a sufficiently large gauge causes the average heat-transfer coefficient to be very similar to that which would exist in its absence. This result leads to the ironic conclusion that a larger gauge provides a more accurate measurement than a smaller one. Therefore, the total heat flux gauge designed for use in the subscale SRM (shown schematically in Figure 3-14) forms the leading edge of the flow channel and is almost as long as the ablative material sample located directly downstream of it. In addition, it spans the entire width of the flow channel to ensure that the effect of the inevitable thermal boundary-layer perturbation is one-dimensional.

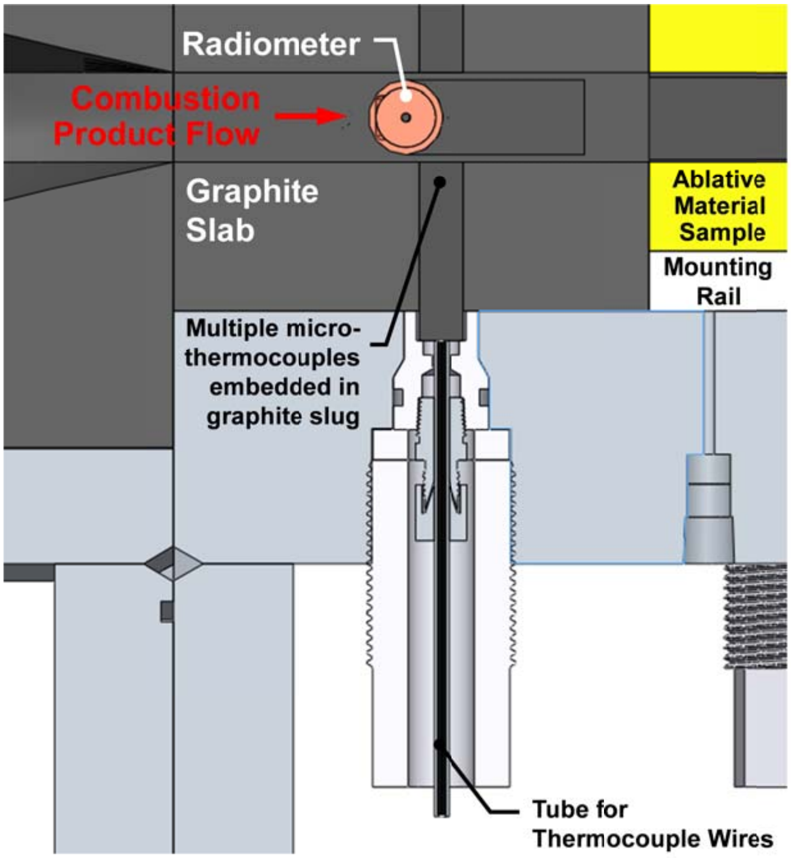

Figure 3-14 Schematic of heat flux gauge installed in subscale SRM

The sensors of the total heat flux gauge are practically identical in construction to the ablative temperature sensors, with multiple micro-thermocouples embedded at different depths, but in a cylinder of graphite, rather than ablative material. Graphite was chosen for this application for its thermal stability and erosion resistance, which are such that phase-change and oxidation phenomena occurring at the surface of the graphite may be neglected in heat transfer analyses of the gauge. This assertion was supported by pre- and post-firing measurements and observations of the graphite slabs from both the short- and long-duration subscale SRM firings, which indicated that no significant degradation or erosion of the graphite was occurring during the firings.

The micro-thermocouples measure the thermal profile within the graphite plug, which is then used to deduce the total heat flux to its surface. The concerns regarding the response time and intrusiveness of the embedded thermocouples in the ablative temperature sensors apply with equal, if not greater, consequence to the heat flux gauges, due to the sensitivity of the heat flux estimate to errors in the temperature measurements. The thermocouples were installed in the graphite plugs in the same manner as in the ablative temperature sensors, with the primary exception being that the thermocouple beads, as well as the wires, were purposely coated with an approximately 150-μm-thick layer of zirconia in order to electrically insulate them from the graphite. While this measure clearly impairs the time response of the thermocouple bead, the results of multiple test firings with uncoated beads proved that it is necessary to obtain reliable temperature measurements. Thermocouple installation guidelines recommend grounding the thermocouple to prevent an accumulation of charge in the thermocouple circuit from causing it to overload the voltage measurement device [80]. A thermocouple circuit that is not tied to ground is termed “floating”. Since the subscale SRM was grounded to an earth ground for safety reasons (to prevent accumulation of static electricity the sudden, unanticipated discharge of which could cause premature ignition of the solid-propellant grain), the bare-bead thermocouple embedded in the conductive graphite plug is also grounded. Pre-firing tests of the bare-bead heat flux gauges in which the SRM-installed heat flux gauges were heated in-situ with a premixed propane-air flame demonstrated proper and reliable behavior of the measured temperature histories; however, the temperature histories recorded during SRM firings were noisy and revealed temperature behavior that was clearly erroneous. Since the erroneous behavior seemed to begin with motor ignition and end shortly after motor burnout, it was determined that the burning of the propellant itself was somehow inducing electrical signals in the thermocouples through their bare beads. To eliminate this failure mode, the beads were coated with zirconia, but were grounded to the data acquisition system (DAQ) ground, which is different from the earth ground of the subscale SRM. Nevertheless, the results were the same, as it is inevitable that at least one thermocouple of the many present in a given test would be broken and therefore shorted to the motor, a condition which allowed this spurious “motor voltage” to be fed into the other thermocouple channels via their common ground. Since it is impractical to attempt to connect each thermocouple to a separate ground, the solution to this problem was to allow the thermocouples to float. This fully-floating configuration, while generally considered bad practice due to the potential for the thermocouple’s electrical potential to float out of the measurement range of the DAQ, as well as its inherent noisiness, finally provided satisfactory temperature histories, and, therefore, was adopted for all subsequent subscale SRM firings.

The presence of the zirconia coating on the thermocouple bead complicated the calculation of its time response; however, this problem was conservatively simplified by approximating the bead as being a cylinder composed entirely of zirconia at the coated diameter (350-μm). Using the data of Rabin and Rittel [79], the time constant of the centerline temperature of these zirconia thermocouples was calculated to be 10 ms when embedded in the sensor graphite. This is more than sufficient time resolution considering the minimum time-steps required for stability of the IHCA are on the order of hundreds of milliseconds.

The theory underpinning the operation of the total heat flux gauges was predicated on the temperature distribution within, and thus, the heat flux at the surface of the graphite plug was identical to that in the surrounding graphite slab. Ideally, the plug would have been press-fit into the slab, so that no gap would exist between the two parts, as is done with the ablative temperature sensors in the ablative material samples. Unfortunately, a press-fit precluded both the installation and removal procedures that were required for use and re-use in the subscale SRM. Therefore, a slip-fit between the plug and the slab was necessary to minimize the gap between the two while allowing the desired installation techniques. The presence of a gap between the plug and the slab threatened to introduce a thermal perturbation error only if the plug established a surface temperature that was significantly different from the slab or if the gap caused a significant disturbance in the momentum boundary layer. Treating the momentum boundary layer over the graphite slab as an external one over a flat plate with its origin at the leading edge of the graphite slab, zero pressure gradient, constant free-stream velocity, and its cross-stream velocity profile described by the 1/7th-power-law, the thickness of the viscous sublayer was calculated to be more than 4.5 times thicker than the gap between the graphite slab and the cylinder; therefore, the disturbance in the momentum boundary layer caused by the presence of this gap was quickly dissipated and did not alter the overall heat transfer rate to or temperature profile within the cylinder vis-à-vis that of a continuous slab at the same longitudinal location.

Since the graphite plug and slab functioned as essentially the same thermal mass, the heat flux gauge is correctly thought of as encompassing both the slab and the plug, functioning as a single unit. This created a gauge that covers the entire width of the flow channel and the length from the end of the flow transition to the leading edge of the ablative sample. The different surface temperatures adopted by the graphite and the ablative material samples introduced a perturbation in the thermal boundary layer that caused the film coefficient to spike to an extremely high value at the interface between the graphite and the ablative sample, just as it would have if it had been the leading edge of the flow. Unlike the effect of the thermal perturbations in the immediate vicinity of a heat flux gauge, this one was of little consequence, as the film coefficient decayed rapidly, such that its average value over the length of the sample was practically identical to that that would have existed if the entire flow channel had been composed of ablative material. Additionally, the graphite/ablative material interface was well defined and thus conductive to being modeled, so that the magnitude of any potential errors could be obtained. Therefore, there was no significant error introduced into the heat flux measurement due to the effects of thermal perturbations in the boundary layer.

Similarly, the effects of cross-conduction due to measuring the heat flux in a conductive material in contact with an insulating material were also mitigated by the size of the heat flux gauge. The thermocouples measuring the thermal profile in the graphite were located near the center of the graphite slab in both directions parallel to the flow, and so were insulated from edge effects.

3.4.1. *Inverse Heat Conduction Analysis*

The heat flux to the surface of the graphite is determined via inverse heat conduction analysis (IHCA) from the measured transient temperature profiles. Conceptually, the IHCA procedure guesses the surface heat flux history, and then uses a numerical heat conduction solver to calculate the corresponding temperature histories through the graphite. The calculated and measured temperatures are then compared, and the surface heat flux estimate is revised based on the magnitude and direction of their differences. The graphite slab is modeled as one-dimensional, due to the geometry of the problem, with constant density, but otherwise variable-temperature properties. Marquardt's modification of the Gauss method of minimization of sum of squares functions [65] was used to simultaneously determine both the front surface (combustion-product-flow-side) and backside (motor-case-side) heat flux histories of the graphite slab. The heat flux through the backside was estimated so that the model was not restricted to the approximation of an adiabatic or constant-temperature backside. The heat conduction equation in the direct problem solver was spatially discretized using a second-order central finite volume method, and the resulting ordinary differential equation was integrated with the DVODE solver [81].

Due to the need for robust mechanical support of the graphite sensor cylinder, the cylinder is 6.4 mm longer at 38.1 mm than the graphite slab is thick at 31.8 mm. As the temperature distributions within the cylinder and slab are considered identical in this one-dimensional formulation, the computational domain length for the IHCA is set as 31.8 mm, where the backside of the graphite slab is considered the backside of the domain.

At least one temperature measurement is required for each surface heat flux estimated, and the nearer a temperature measurement is to a particular surface, the more sensitive it is to the heat flux at that surface; therefore, each of the heat-flux sensors was equipped with at least two thermocouples: one within 2 mm of the front surface and another within 2 mm of the backside. Some sensors were equipped with more than these two thermocouples, causing the problem to be overdetermined: a situation which reduces the sensitivity of the deduced heat flux to the thermocouple measurement errors and increases the stability of the IHCA.

To mitigate the effect of electrical noise on the deduced heat fluxes, the thermocouple-measured temperature histories are smoothed using the robust "lowess" function in MATLAB (version 7.12.0.635) prior to being used in the IHCA. The measured temperatures used in the IHCA are simply taken from these smoothed histories at the time-steps desired for the inverse calculation.

3.4.1.1. Grid Independence of Direct-Solver Solutions

In order to determine the amount of spatial grid refinement required to produce an accurate solution of the heat conduction equation, a grid convergence study was performed on the direct problem solver of the IHCA. The heat flux history derived from the combined convection and radiation anticipated from the higher-heat-flux configuration of the SRM was specified as the input to the direct solver, which then calculated the temperature history of the computational domain, whose length in this instance was equal to that of the heat flux sensor (38.1 mm) and whose thermal properties were those of the sensor graphite. A solution was produced for two different grids: one using 150 cells and the other using 450 cells resulting in a grid ratio of 3. The temperatures calculated at three different locations corresponding to likely thermocouple locations (1.9, 3.4, and 34.7 mm from the front surface of the domain) were compared at each calculated time-step for each grid. Following the method of [82], the maximum fine-grid grid convergence index (GCI) calculated for any of the three temperatures at any of the calculated time-steps was 0.005%. Nevertheless, an even finer grid, comprised of 1270 cells for a domain length of 31.8 mm, was used for the final calculations due to the requirement of the uncertainty analysis that a relatively small perturbation in a specified thermocouple location cause the thermocouple to be located in a different cell.

3.4.1.2. IHCA Code Verification

The direct heat conduction solver was first validated by comparing the results of a test case to exact analytical solutions, which it was able to replicate with negligible error. In order to verify the proper numerical operation of the inverse method itself, the direct heat conduction solver was employed to calculate the temperature history at three discrete locations in the graphite for two given heat flux histories: a triangle on the front surface and a square wave on the backside surface. The material properties used were those of the sensor graphite, and the thermocouples were located at 1.6, 3.2, and 34.9 mm from the front surface of a 38.1 mm domain. Normally-distributed random error equivalent to the bias uncertainty of S-type thermocouples (±1.5°C for $T \leq 600°C$, ±0.25% for $T > 600°C$) was introduced into the calculated temperature histories to provide a realistic challenge for the IHCA. Due to the temperature histories' being smoothed prior to being submitted to the IHCA code, the additional uncertainty of electrical noise was not added to the thermocouple bias error for the verification test. The resulting artificial temperature histories are then used as inputs to the IHCA code in the same way thermocouple measurements from a total heat flux gauge would be, and if the IHCA code works correctly, the resulting surface heat flux histories should match those used to generate the artificial temperatures. The results of the verification exercise are displayed in Figure 3-15. The IHCA replicates both of the specified heat flux histories quite well, with the calculated heat fluxes for the front surface (triangle) matching almost exactly within the region of interest. More deviation is evident for the backside surface (square wave), which is due to its having only one thermocouple as opposed to the two present

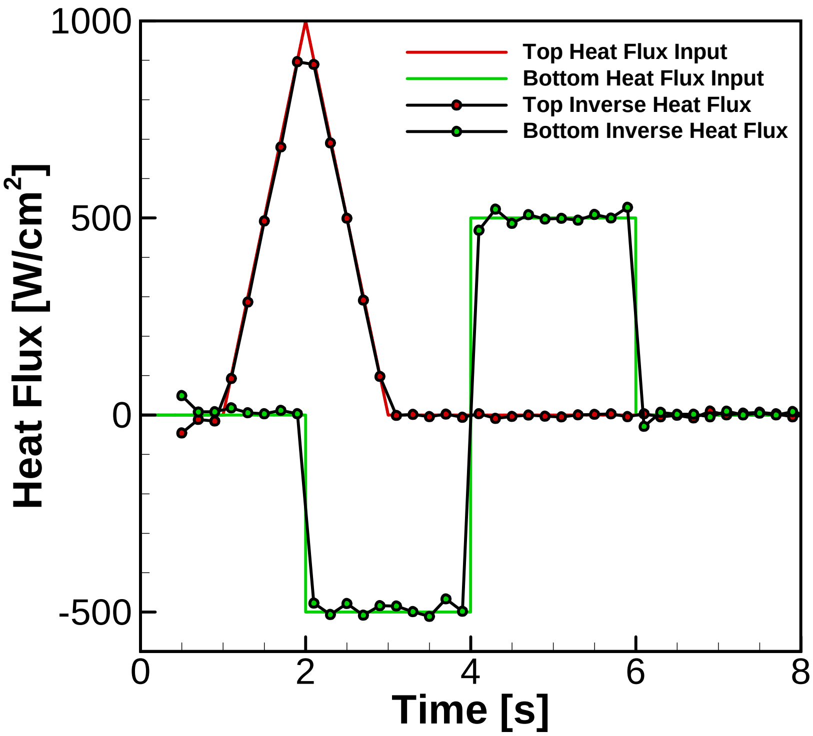

Figure 3-15. Results of the IHCA code verification exercise

near the top surface and that thermocouple being located further from the bottom surface (3.2 mm) than the nearest one to the top surface (1.6 mm). When the verification test is repeated with an additional thermocouple located at 1.6 mm from the backside surface, the mean squared error for the backside heat flux estimate decreases by 56%, indicating this to be the case. Without the addition of error to the thermocouple measurements, the calculated results matched the input heat fluxes exactly (mean squared error < 0.001 W/cm^2 for both flux histories).

3.4.1.3. Uncertainty in Measured Temperatures

In order to determine the uncertainty in the IHCA-deduced total heat flux, the uncertainty in each of its input parameters must be quantified. For this analysis, the temperature measurements were considered to have two sources of bias error: errors in voltage output of the thermocouple itself and the cold junction compensation, voltage measurement, and linearization errors of the data acquisition system used to measure the thermocouple voltage. The former was defined for S-type thermocouples as ±1.5°C for $T \leq 600$°C, ±0.25% for $\mathrm{T} > 600$°C by the thermocouple wire manufacturer (Omega Engineering), and the latter is defined as ±2.8°C for $-50 \leq T \leq 150$°C, ±1.8°C for $150 < T \leq 1768$°C by GW Instruments, Inc. for S-type thermocouples measured by its Instrunet iNet-100B data acquisition system. The random error in the thermocouple measurements was assumed due primarily to electrical noise and therefore estimated from the standard deviation of the residuals calculated from the measured temperature smoothing procedure, with typical values less than ±1.0°C for a given sensor in a particular SRM firing. For temperature, as well as all other measured parameters treated in this work, bias, random, and total uncertainty estimates, whether cited by instrument manufacturers or directly calculated by the author, are reported the 95% confidence level.

3.4.1.4. Precise Location of Thermocouples

Due to the sensitivity of the IHCA to errors in the location of the temperature measurements, high-resolution (64.5 pixel/mm) X-ray radiographs were taken of the sensors prior to their use in the SRM firings. The uncertainty in the image scale was estimated as ±2.1 mm/pixel from the X-ray image calibration process, and the location of the thermocouples could be determined from the radiographs to within less than ±1 pixel. In order to achieve the highest possible resolution radiographs for the thermocouples nearest the front surface, the thermocouples located near the backside surface were not included in the radiographs; therefore, their locations were assumed to be nominal and the uncertainty on those locations was estimated as the radius of the hole drilled in the graphite sensor material (0.397 mm) plus the tolerance on the hole location (0.127 mm). The locations of the thermocouples in the heat flux sensors used in this study relative to the heat flux sensor's front face as well as their estimated random, bias, and total (combined random and bias) uncertainties are detailed in Table 3-I.

Table 3-I. Distances of the embedded thermocouples from the front face of the heat flux sensors (y) and their random (P_y), bias (B_y), and total (U_y) uncertainties

Sensor	TC	y [mm]	P_y [mm]	B_y [mm]	U_y [mm]
1	1	1.58E+00	1.55E-02	5.10E-02	5.33E-02
	2	2.92E+00	1.55E-02	9.41E-02	9.54E-02
	3	3.18E+01	0.00E+00	5.24E-01	5.24E-01
2	1	1.65E+00	1.55E-02	5.32E-02	5.54E-02
	2	1.33E+01	1.55E-02	4.30E-01	4.31E-01
	3	3.18E+01	0.00E+00	5.24E-01	5.24E-01

3.4.1.5. Determination of Sensor Graphite Thermal Properties

Just as the IHCA is sensitive to errors in the temperature measurements, it is sensitive to errors in the thermal properties of the material in which the measurements are taken. As density, thermal conductivity, and the isotropy of these properties vary considerably with the type and grade of graphite, it was deemed necessary to measure these properties of the sensor graphite, so that they were known with reasonable accuracy and so that this accuracy was quantified. The density of the sensor graphite was determined via helium pycnometry to be 2.0557 ± 0.0025 g/cc. An Anter Laser Flash 5000, with manufacturer-reported uncertainties of ±5% on the measurement accuracy and ±3% on the measurement repeatability, was used to ascertain the value of the thermal diffusivity of the sensor graphite by making three measurements at 12 different temperatures. As the specific heat of graphite does not vary significantly among various grades and production methods, the specific heat was not directly measured: instead, the specific heat equation given in Burchall [83] (which states that it is "applicable to all graphites") was used and considered exact for the analyses performed in this study. Multiplying the measured thermal diffusivity at each test temperature by the measured density and polynomial-calculated specific heat yields the thermal conductivity data shown in Figure 3-16, where the vertical error bars represent the total uncertainty in the thermal conductivity. The total uncertainty in the thermal conductivity was calculated from the random and bias uncertainties of the density and thermal diffusivity. The equation displayed in Figure 3-16 was fit using least-squares regression to the measured thermal conductivity data and is represented on the plot by a solid black line. It was from this equation that the IHCA calculated the thermal conductivity of the graphite for a given temperature; therefore, the uncertainty in the regression model was determined via the method described in Coleman and Steele [84], using finite differences to approximate the necessary partial derivatives and using the random and bias uncertainties of the thermal conductivity data as well as that from the thermocouple-measured test temperatures. The resulting uncertainty interval about the regression model is plotted as two dashed lines in Figure 3-16.

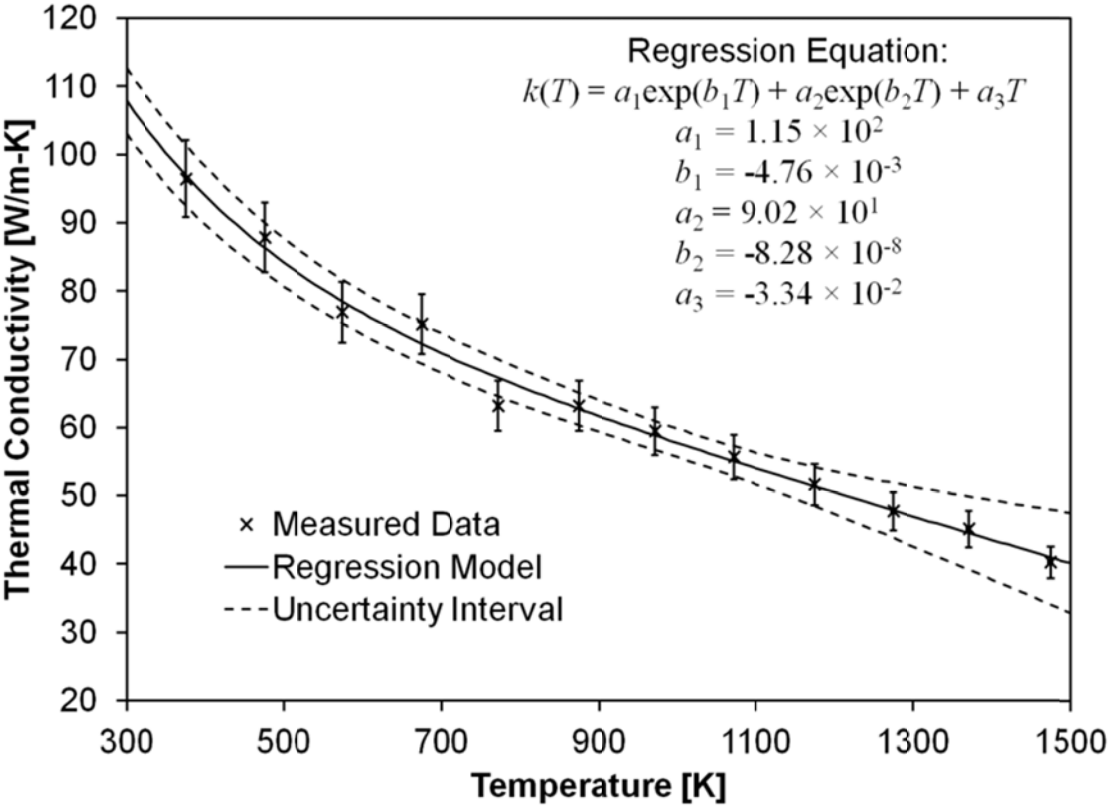

Figure 3-16. Thermal conductivity vs. temperature data for the heat flux sensor graphite

3.4.1.6. IHCA Uncertainty Analysis

The total surface heat fluxes and temperatures calculated through the IHCA are dependent on several input parameters that are measured quantities and, thus, have associated uncertainties that introduce additional uncertainty into the calculated values: subsurface temperature histories, thermocouple locations, and thermal properties (density, specific heat, and thermal conductivity). Given the complexity of calculating the sensitivities of the IHCA-deduced quantities to each of the uncertain input parameters, use of the traditional uncertainty propagation equations was eschewed in favor of uncertainty analysis by direct Monte Carlo simulation as described in Coleman and Steele [84]. In this technique, a random value sampled from the population of possible values of each of the measured input parameters was substituted for the nominal value of that parameter, and the surface flux and temperature histories were deduced from these perturbed input values. The population of possible values for a given parameter was assumed to be normally-distributed about a mean equal to the nominal value of that parameter, and the standard deviation of this distribution was determined from the random and bias uncertainties associated with that parameter. 10,000 Monte Carlo iterations were performed for one representative measurement, that of Sensor #1 in Test #ABLMAT-35, whose configuration was the most common of those used in the SRM test firing series. The standard deviations of the resulting distributions of surface heat fluxes and temperatures were then multiplied by 1.96, the value of the *t*-distribution corresponding to the 95% confidence level for 9999 degrees of freedom, to specify the uncertainty in each of these results.

3.4.2. Calculation of Convective Heat Flux

By modeling the total heat flux as consisting only of the sum of the contributions of convection and thermal radiation, the convective contribution was determined by subtracting the thermal radiation absorbed by the graphite sensor from the measured total flux at each IHCA time-step. In order to calculate the thermal radiation flux absorbed by the graphite sensor, the thermal radiation flux measured by the radiometer was assumed equal to the net radiation flux emitted by the combustion product cloud ($\dot{q}''_p$), which is equal to the irradiation on the surface of the graphite sensor. The heat balance on the surface of the graphite is given by:

$$\dot{q}''_{rad} = \alpha_s \dot{q}''_p - \varepsilon_s \sigma T_s^4 \tag{3.3}$$

where the graphite-sensor-absorbed heat flux ($\dot{q}''_{rad}$) is equal to the difference between the absorbed portion of the incident radiation flux and the graphite surface emission, which is calculated from the IHCA-deduced graphite surface temperature.

For this calculation, the absorptivity is approximated as equal to the emissivity via Kirchoff's Law, and value of the emissivity was estimated as 0.85 [85].

3.4.2.1. Dimensionless Heat Transfer Parameters

In order to characterize the convective flow in the test section of the SRM in terms of the usual dimensionless parameters (Nusselt and Stanton numbers), the heat transfer coefficient was calculated from Newton's Law of Cooling using the deduced convective heat flux and sensor surface temperature histories in conjunction with the CEA-calculated solid-propellant flame temperature as demonstrated by:

$$h_i = \frac{\dot{q}''_{conv,i}}{T_\infty - T_{s,i}} \tag{3.4}$$

(In the foregoing equations, properties of the combustion products, adiabatic flame (free-stream) temperature, T_∞; combustion product density, ρ; dynamic viscosity, μ; thermal conductivity, k; and Prandtl number, Pr, were calculated using NASA CEA [86] for the time-averaged SRM chamber pressure for each firing.) From this heat transfer coefficient, the local Nusselt number was then calculated for each time-step using:

$$\mathrm{Nu}_{x,i} = \frac{h_i x}{k\left(T_{film,i}\right)} \tag{3.5}$$

where the thermal conductivity of the combustion products was evaluated at the film temperature [$T_{film,i} = (T_\infty + T_{s,i})/2$], and x is equal to 57.15 mm, the distance from the leading edge of the graphite slab to the center of the heat flux sensor. The resulting Nusselt number histories were then averaged over the firing duration to produce $\overline{\mathrm{Nu}_x}$ for each sensor in each SRM firing. Similarly, the Stanton number was computed at each time-step for each sensor in each SRM firing from:

$$\mathrm{St}_i = \frac{h_i}{\rho c\left(T_{film,i}\right) u_\infty} \tag{3.6}$$

and an average value was produced by integrating Equation (3.6) over the SRM firing duration.

3.4.3. Total Heat Flux Gauges in SRM Firings

3.4.3.1. Heat Flux Gauge Measurements in Instrumentation Validation Firings

After sorting out the electrical issues with the thermocouple measurements in the total heat flux sensors, subsurface temperature histories of the sensors were successfully measured in three CP-grain-configured short-duration SRM firings during the instrumentation validation firing series. The total heat flux deduced from these temperature histories is displayed in Figure 3-17, where Tests #ABLMAT-15 and #ABLMAT-16 only included one operable heat flux sensor but Test #ABLMAT-17 included two functioning heat flux sensors, which are denoted by the side of the flow channel in which they were installed, either left or right. These heat flux histories vary considerably at early times, but converge toward the same steady-state value as the firing

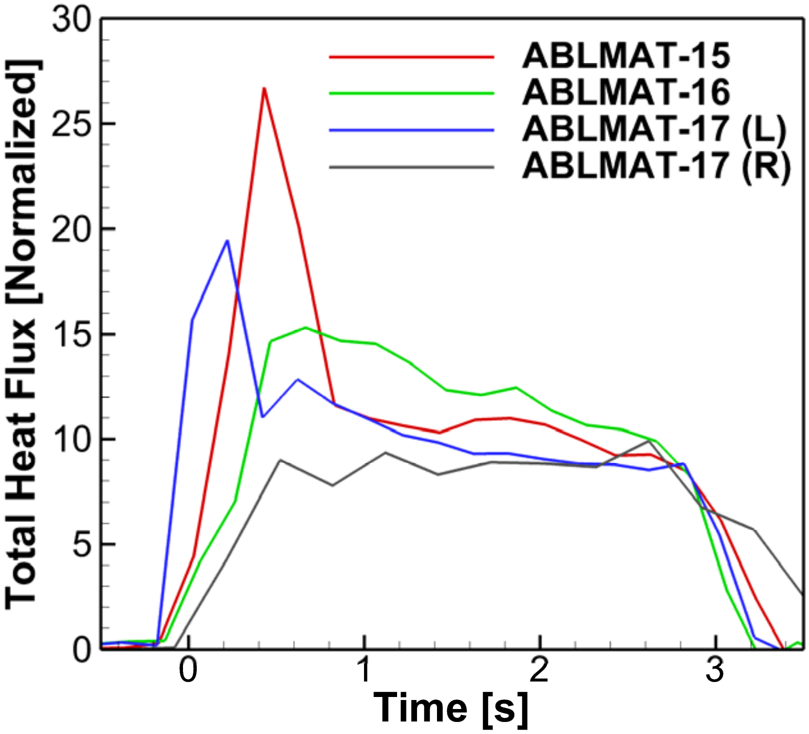

Figure 3-17. Total heat flux histories deduced from three CP-grain-configured SRM firings

progresses. The locations of the thermocouples in the heat flux sensors used in this firing series were not precisely determined using high-resolution X-ray radiography as they were for the long-duration firings, and no uncertainty analysis was performed for these cases. Nevertheless, the successful acquisition of temperature measurements and deduced total heat fluxes from these firings established the efficacy of this technique for use in the long-duration ablative material performance assessment firings.

3.4.3.2. Heat Flux Gauges in SRM Firings for Ablative Material Assessment

Two different heat flux sensors were installed in each of the six subscale SRM test firings used to assess the performance of the ablative internal insulators. Data from a second sensor, however, is not available for three of the six firings (Tests #ABLMAT-33, #ABLMAT-37, and #ABLMAT-38) due to damage incurred by these sensors during either installation or the firing itself. While three thermocouples were installed in each of these sensors produced useful results at the locations given in Table 3-I, TC #2 for Sensor #2 was apparently damaged during handling or installation into the SRM, as it never provided meaningful data, and TC #2 for Sensor #1 only produced useful data for Test #ABLMAT-36. Therefore, in all cases except for Sensor #1 in Test #ABLMAT-36, only two temperature histories were available for use in deducing the front surface and backside heat fluxes. For the remainder of this report, the individual heat flux measurement cases will be denoted by the test number followed by the sensor number (e.g. ABLMAT-36 (1): Sensor #1 in Test #ABLMAT-36).

3.5. Thermal Radiation Flux Gauge (Radiometer)

3.5.1. Overview of Key Features

For this study, a radiometer was designed and fabricated for use in an SRM with test durations greater than 20 s. This design, depicted schematically in Figure 3-18, consists of a thermal radiation sensor isolated from convective heat transfer from the combustion products flow by a window, which was recess-mounted in the combustion chamber wall to prevent thermal damage to the window from convection. This recess introduces a backward-facing step into the flow channel wall, which induces a particle-trapping recirculation zone directly in front of the radiometer. A jet of inert gas injected into the SRM at an oblique angle to the combustion product flow was incorporated into

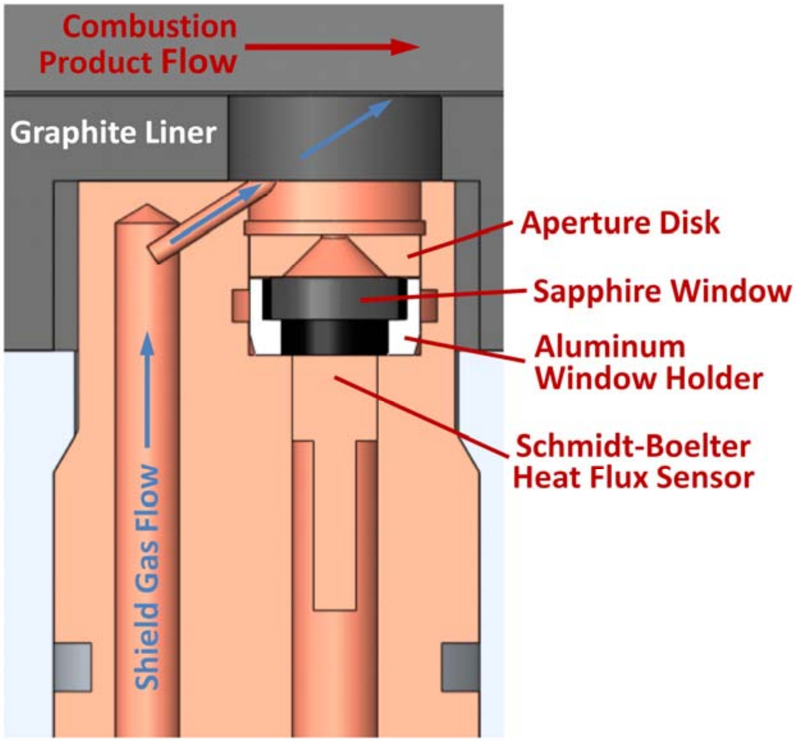

Figure 3-18. Schematic of radiometer with single oblique shield-gas jet installed in subscale SRM

the initial design to divide this recirculation zone into two regions: an upper one consisting of hot gaseous combustion products and Al_2O_3 particles and a lower one consisting almost entirely of cold inert gas. In this configuration, the window was expected to be exposed only to the cold inert gas, protecting it from both thermal damage and view obstruction due to alumina deposition. Helium was initially selected as the purge gas due to its low molecular weight, which allowed for a higher momentum shield gas flow than heavier gases with minimal addition of mass to the system. In addition, being a monatomic gas, helium does not absorb or emit radiation in the infrared spectrum, so it would not interfere with the radiation measurement.

3.5.2. Thermal Radiation Sensor

A Schmidt-Boelter-type heat flux sensor [87] was chosen for this application because it was commercially available, had good sensitivity to radiative heat fluxes of the expected magnitudes in a relatively small size, produced an output voltage that is directly proportional to the incident flux, and, provided it was in good thermal contact with a sufficient heat sink, was capable of delivering continuous measurements for an indefinite time. The front (sensing) surface of the sensor was coated with black paint with a reported absorptance of 0.94 to maximize the sensor’s absorption of thermal radiation. The body of the radiometer was designed as a large copper heat sink, so that the sensor, which was press-fit into the radiometer body to minimize thermal contact resistance, could be maintained at a relatively constant temperature throughout the test duration, thereby mitigating drift in the sensor response due to changes in the sensor temperature. In order to quantify the temperature change of the radiometer body, and, thus, the potential for thermal drift in the sensor response during the course of an SRM firing, a K-type thermocouple was installed from the backside of the radiometer with its bead located about 2 cm behind the Schmidt-Boelter sensor.

In order to determine the required flux measurement range and sensitivity of the thermal radiation sensor, the anticipated thermal radiation flux from the combustion products was estimated from available data. As the condensed-phase particles are easily the largest contributor to the radiative heat flux to the ablative material surface [68], the narrow-band contributions from infrared-active gaseous species present in the combustion products (primarily CO_2, CO, H_2O, and HCl) [68] were ignored in estimates of radiation flux from the combustion products. A detailed study of the radiative environment of a similar SRM by Jung and Brewster [88], determined that the representative extinction coefficient for the combustion products in the interior of the motor was 3150 m^{-1}, and that this value was due almost entirely to the contributions of the 1-µm alumina smoke particles because of their overwhelming number density. Since the extinction coefficient is directly proportional to the number density of the radiatively-participating particles [89] and the number density itself is assumed directly proportional to motor pressure [68], the extinction coefficient for the current study's subscale motor was computed to be 2300 m^{-1}, which equates to a photon mean free path of merely 0.43 mm. Since the flow channel was 115 mm wide in the viewing direction, the optical thickness of the channel was 270, which is much greater than unity, meaning that the flow channel was optically thick. Dombrovskii [90] defines the integral hemispherical degree of blackness of a uniform isothermal plane-parallel layer of a dispersed medium as the ratio of the integral flux of thermal radiation to the radiation of a blackbody at the same temperature. This same reference reports the calculated values of this degree of blackness for optically thick, monodispersed systems of alumina particles of various sizes (between 0.5 and 5.0 μm) at three different temperatures (2500, 3000, and 3500 K). A linear model of the variation of the integral degree of blackness with temperature for a cloud of 1-μm alumina particles was derived by fitting this data using linear least-squares regression. This model was then used to determine the integral degree of blackness for a cloud of 1-μm alumina particles at 3600 K (the adiabatic flame temperature of the TP-H1148 solid propellant at the median SRM chamber pressure as calculated by NASA CEA [86]) and yielded a value of 0.68. Using this information, the anticipated total hemispherical flux emanating from the hot combustion product flow was computed to be 640 W/cm^2. This was not, however, the heat flux incident on the sensor, as the aperture significantly decreases the flux of the incoming radiation by constricting the size of the solid angle of rays that was directly viewed by the sensor, a fact which necessitated the assumption that this reduced solid angle of thermal radiation that was incident on the sensor was representative of the entire hemisphere, i.e. that the radiation from the combustion products was diffuse. From the point of view of the sensor, the combustion product flow channel appears as a gray, diffuse, opaque surface with the same heat flux as the combustion products, but at the size and location of the aperture; therefore, the equation for calculating the net radiation heat transfer between any two diffuse, gray, and opaque surfaces can be used:

$$\dot{q}_{a\to s} = F_{a\to s} A_a \left(J_a - J_s \right) \tag{3.7}$$

Beginning with the definition of absorptivity [89] and assuming that the irradiation on the surface of the slug from all other sources was negligible compared to that originating from the combustion products, the rate of radiation heat transfer to the sensor was related to the net radiation heat transfer between the artificial surface at the aperture location and the sensor:

$$\alpha = \frac{\dot{q}_s}{\dot{q}_{a\to s}} \tag{3.8}$$

Applying Kirchoff's Law and rearranging Equation (3.8), yielded:

$$\dot{q}_s = \varepsilon_s \dot{q}_{a\to s} \tag{3.9}$$

Substituting Equation (3.7) into Equation (3.9) and accounting for the attenuation of the radiation through the window yielded:

$$\dot{q}_s = \tau_w \varepsilon_s F_{a\to s} A_a \left(J_a - J_s \right) \tag{3.10}$$

Given the relatively low temperature of the thermal radiation sensor vis-à-vis that of the combustion products as well as its high value of absorptance, the sensor surface was approximated as cold and black; thus, the sensor radiosity term in Equation (3.10) was eliminated. In addition, the magnitude of any radiation incident on the combustion product cloud was assumed negligible so that the radiosity of the artificial surface at the aperture location was approximated as equal to the product of its effective emissivity (the integral hemispherical degree of blackness of the 1-μm alumina cloud) and its blackbody emissive power, resulting in the following relation:

$$\dot{q}_s = \tau_w \varepsilon_s F_{a \to s} A_a \varepsilon_a \sigma T_a^4 \tag{3.11}$$

The view factor from the aperture to the sensor was calculated from Tanaka [91] to be equal to 0.107, and the open area of the aperture was 3.09×10^{-2} cm^2, values which, when combined with the other variables in Equation (3.11) yielded an expected thermal radiation flux of 5.4 W/cm^2 at the surface of the sensor. Given the number of gross assumptions involved in this analysis and the vagaries involved in the estimation radiative properties in general, the sensor was specified to have a maximum range of 10 W/cm^2 to reduce the likelihood that the sensor would be saturated (and/or damaged) under the true SRM firing conditions, while still maintaining sufficient sensitivity to lower fluxes.

3.5.3. Window

Sapphire was chosen as the window material because it has an essentially constant spectral transmittance (approximately 0.84) over a relatively wide range of wavelengths in the infrared spectrum (about 0.4 to 4 μm), as well as excellent mechanical strength for withstanding the pressure loads to which it was subjected in the SRM. The window was affixed by means of an epoxy adhesive into an aluminum holder whose outer surface created a piston seal with an O-ring installed in the radiometer body. This assembly ensured that pressurized gases, whether from the hot SRM products or the cold shield gas jet could not enter the sensor region and affect the radiation measurement.

3.5.4. Radiometer Aperture and Interior Surfaces

In order to prevent the thermal radiation sensor from exchanging radiant energy with any external source other than the combustion products, a relatively small aperture was positioned on the side of the window opposite the sensor, which, in conjunction with the sensor's depth in the gauge, fixes its viewing angle with respect to the combustion products in the flow channel. The diameter of the aperture was sized to furnish a view angle such that no radiation emitted from the SRM walls could reach the sensor without passing through a thickness of hot combustion products greater than 20 times the calculated photon mean free path. Due to the depth of the sensor's recess into the flow channel wall and the relatively short height (y dimension) of the flow channel, this viewing angle was required to be rather narrow, meaning that the vast majority of the total hemisphere that the thermal radiation sensor views was comprised of the interior surfaces of the radiometer; consequently, it was of singular importance to minimize any radiative exchange between the sensor and these surfaces. Radiation heat transfer due to emission and absorption between the interior surfaces of the radiometer and the sensor can be eliminated by constantly maintaining them thermal equilibrium; therefore, each of the components with a surface in view of the sensor was composed of either copper or aluminum and were in contact with the copper radiometer body, so that their temperatures were maintained as near as possible to that of the sensor. As an additional measure, both surfaces of the copper aperture disk were polished between SRM firings to keep them free of oxidation in order to minimize thermal radiation absorption from the combustion products and to minimize radiation emissions to the sensor. As the interior surface of the aluminum window holder was exposed to direct radiation from the combustion products through the radiometer aperture, this surface was capable of reflecting this combustion product radiation to the sensor surface, potentially causing errors in the radiation measurement; therefore, the interior surface of the aluminum window holder was painted black (reflectance = 4% for wavelengths < 5 μm) to minimize these reflections.

3.5.5. Shield Gas Flow

The radiometer was installed in the subscale SRM in the configuration shown in Figure 3-18 and fired in a CP-grain-configured firing with the mass flow rate of helium shielding gas set to 2.7 g/s by means of a pressure-reducing regulator and a critical flow orifice located upstream of the radiometer. The post-firing examination of the radiometer revealed that its front surface, including the window, to be thoroughly coated with alumina. This fact was considered to be due to disruption of the radiometer port flow field by alumina accretion on the downstream side of the radiometer port, which was observed after the firing to fill about half of the port area. In order to eliminate this occurrence in subsequent tests, an alumina accumulation relief was cut into the chamber liner downstream of the radiometer port, as shown in Figure 3-19, to allow the molten particles to flow downstream and prevent them from disrupting the radiometer port flow field or obstructing the radiometer's view of the combustion products. It should be noted that the shielding gas was successful in keeping the radiometer body and mask cool, as no part of the radiometer exhibited signs of significant heating.

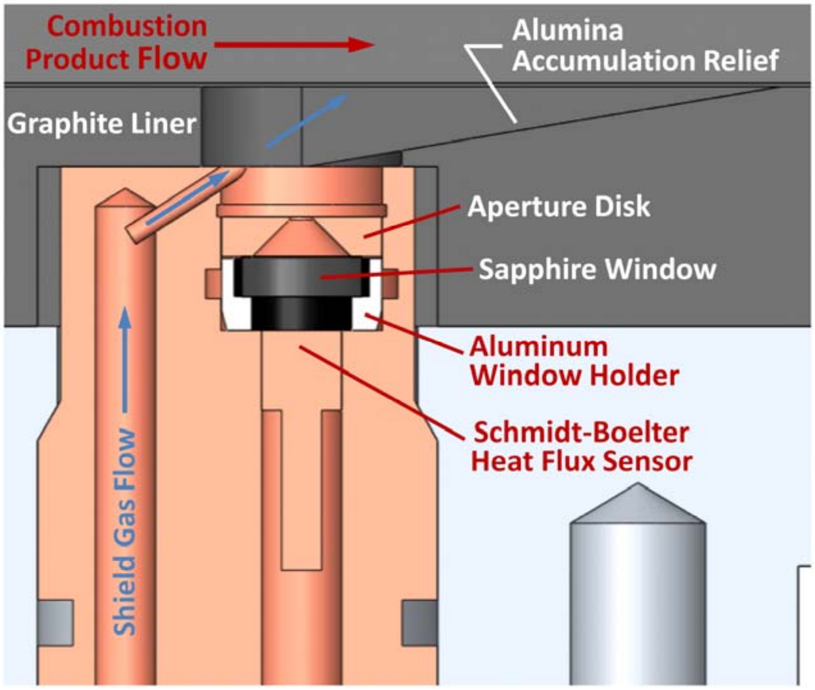

Figure 3-19. Schematic of radiometer with alumina accumulation relief

The ensuing test in which the alumina slag relief was employed resulted in the radiometer port remaining clear of alumina slag, while the surface of the radiometer and window exhibited a thin, powder-like coating of what appeared to be alumina particles as illustrated in Figure 3-20. As this layer was easily removed from the radiometer simply by wiping the affected surfaces, the particles likely froze while traveling through the cold helium region in the radiometer port before striking the window. In subsequent firings, the mass flow rate of the shield gas was increased to 3.3 then 4.0 g/s, with little apparent effect on the post-firing condition of the radiometer. The composition of the shielding gas was then changed to hydrogen, which retains the infrared-radiation-invisibility of helium, but produces higher velocity jets with lower mass flow rates than helium for the same feed gas system. CP-grain-configured SRM firings were then performed with hydrogen mass flow rates in the radiometer of 6.7 and 8.2 g/s, with the latter equivalent to three times the mass flow rate of the initial SRM firing with six times its jet velocity. However, these drastic increases in shield gas mass flow rate and jet velocity counter-intuitively yielded increases, rather than decreases, in the amount of alumina deposited on the front surface and window of the radiometer. Analysis of the material deposited on the copper aperture disk with SEM-EDS, a micrograph from which is shown in Figure 3-21, revealed that the deposition consisted solely of fine (~1-μm) alumina particles. This behavior was likely due to streamwise vortices induced by the finite-width oblique shield gas jet, which drew small (low-momentum) particles behind the jet and into the radiometer port. A stronger jet induces stronger vortices, thus increasing the number of alumina particles trapped in the radiometer port. In addition, periodic vortex shedding from the upstream edge of the radiometer port may cause the shield gas jet to flutter, intermittently sweeping alumina particles from the product flow channel into the port.

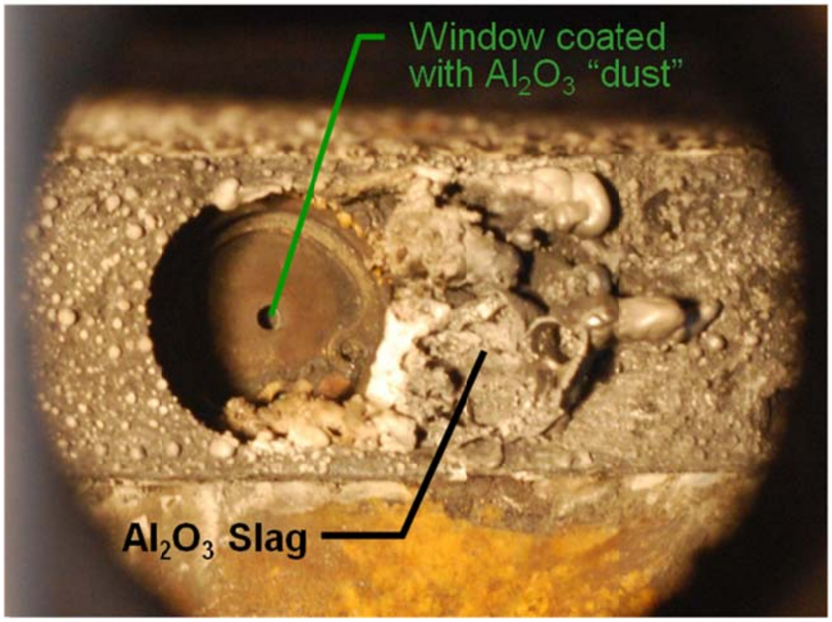

Figure 3-20. Post-firing photograph of in-situ radiometer with single oblique shielding jet

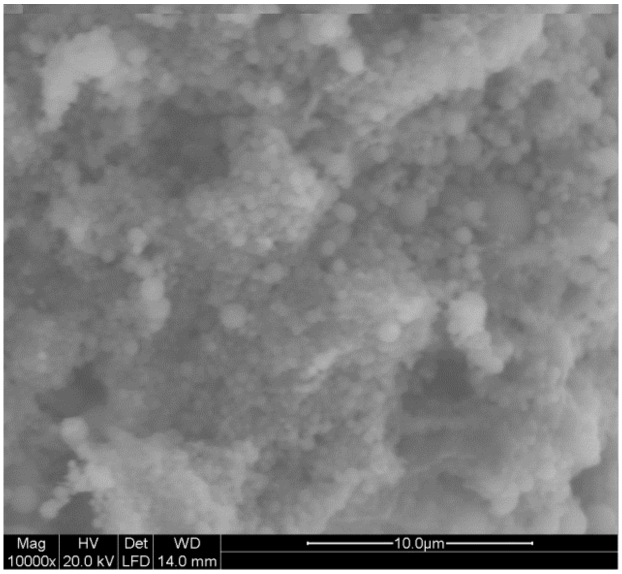

Figure 3-21. SEM micrograph of alumina deposited on aperture disk.

Since, based on these experiments, the oblique shield-gas jet was capable of preventing large alumina particles from entering the radiometer port, yet was incapable of keeping the easily-entrained alumina smoke particles out of the radiometer port, a secondary shield-gas jet, shown in Figure 3-22, was introduced. This jet flows through the radiometer aperture, and therefore has momentum in the direction normal to the window, directly opposing the momentum of any particles attempting to enter the radiometer cavity.

When this configuration was tested in a 5-sec end-burning-grain-configured subscale SRM firing with a total shield gas mass flow rate of 6.3 g/s, there was still a significant deposition of alumina particles on the surface of the copper aperture disk, but the window surface remained absolutely clear of alumina particles. Therefore, this dual-jet shielding system was used to protect the radiometer in the long-duration ablative material characterization SRM firings. In this dual-jet configuration, the vertical jet gas mass flow rate is only 10% of the total flow rate of the shield gas.

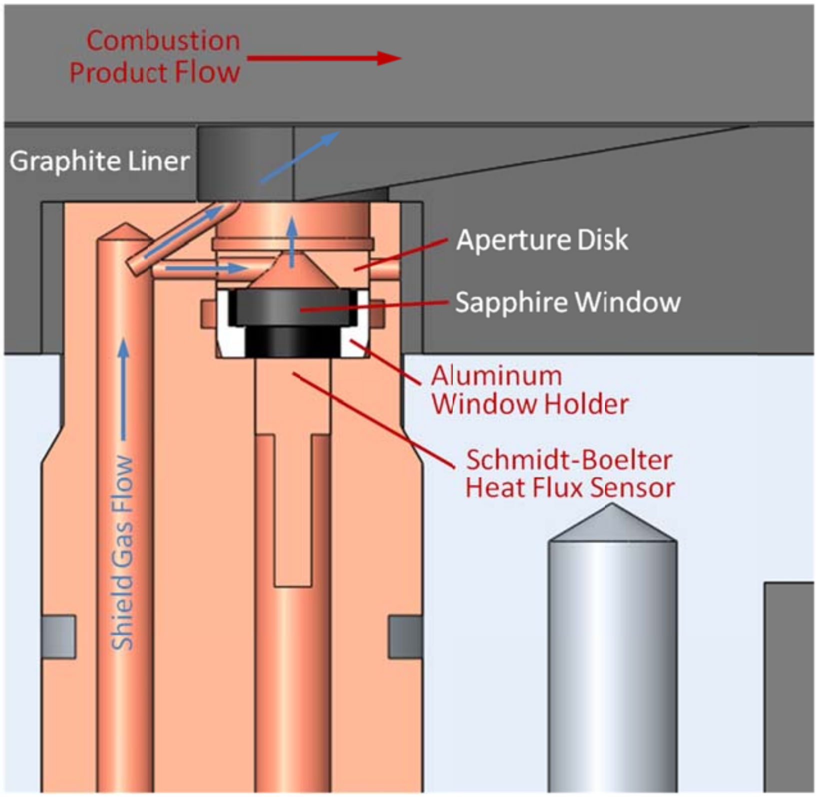

Figure 3-22. Cross-sectional view of radiometer with dual shielding gas jets

3.6. Subscale SRM Test Firing Series for Ablative Material Performance Assessment

The subscale SRM test firing series used to assess the performance of the ablative internal insulators consisted of five test firings (Tests #ABLMAT-33 through #ABLMAT-37) employing all instrumentation (X-ray radiography of ablative samples, embedded thermocouples in samples, total heat flux gauges, radiometer, and pressure transducers) plus an additional sixth firing (Test #ABLMAT-38) operated without a radiometer or subsurface temperature measurements to serve as a control for determining the intrusiveness of those measurement techniques.

Chapter 4 Results & Discussion

Due to export-control restrictions placed on this work, certain results presented in the foregoing section are presented in length, mass, temperature, and flux units that have been normalized by an arbitrary, yet consistent factor.

4.1. Subscale SRM Performance

The excessive thickness of the alumina layer that formed on the interior of the water-cooled copper nozzle in the end-burning-grain-configured subscale SRM firings was responsible for two undesirable characteristics of the five chamber pressure histories seen in Figure 4-1 (the data acquisition system used to record the pressure measurements failed to properly trigger for Test #ABLMAT-36.): one is a very long initial pressurization period (~4 s) and the other is an extreme variability in the pressure histories both throughout the course of a single firings as well as among the six firings. Each of these effects was amplified by the relatively small diameter of the nozzle throat for the end-burning-grain configuration, which causes minor changes in the absolute throat area to be large changes in the relative throat area and thus chamber pressure. The protracted pressurization period was due largely to the time required for the alumina layer to accumulate sufficient alumina to attain its quasi-equilibrium thickness, as ignition, flame-spreading, and initial volume-filling appear to be complete after approximately 0.4 s. The beginning of the quasi-equilibrium portion of an SRM firing is evinced by a marked decrease in the slope of the pressure-time curve and is reasonably consistent among the five firings; however, despite the consistency of the nozzle cooling water flow and other associated test conditions, substantial variation exists among the pressure histories of the firings after the commencement of this period. Tests #ABLMAT-34 and #ABLMAT-38 both proceed to produce relatively constant chamber pressures for the remainder of the firing, while the other three firings tend to continually increase, but at different rates and with different maximum pressures. In addition, each pressure history

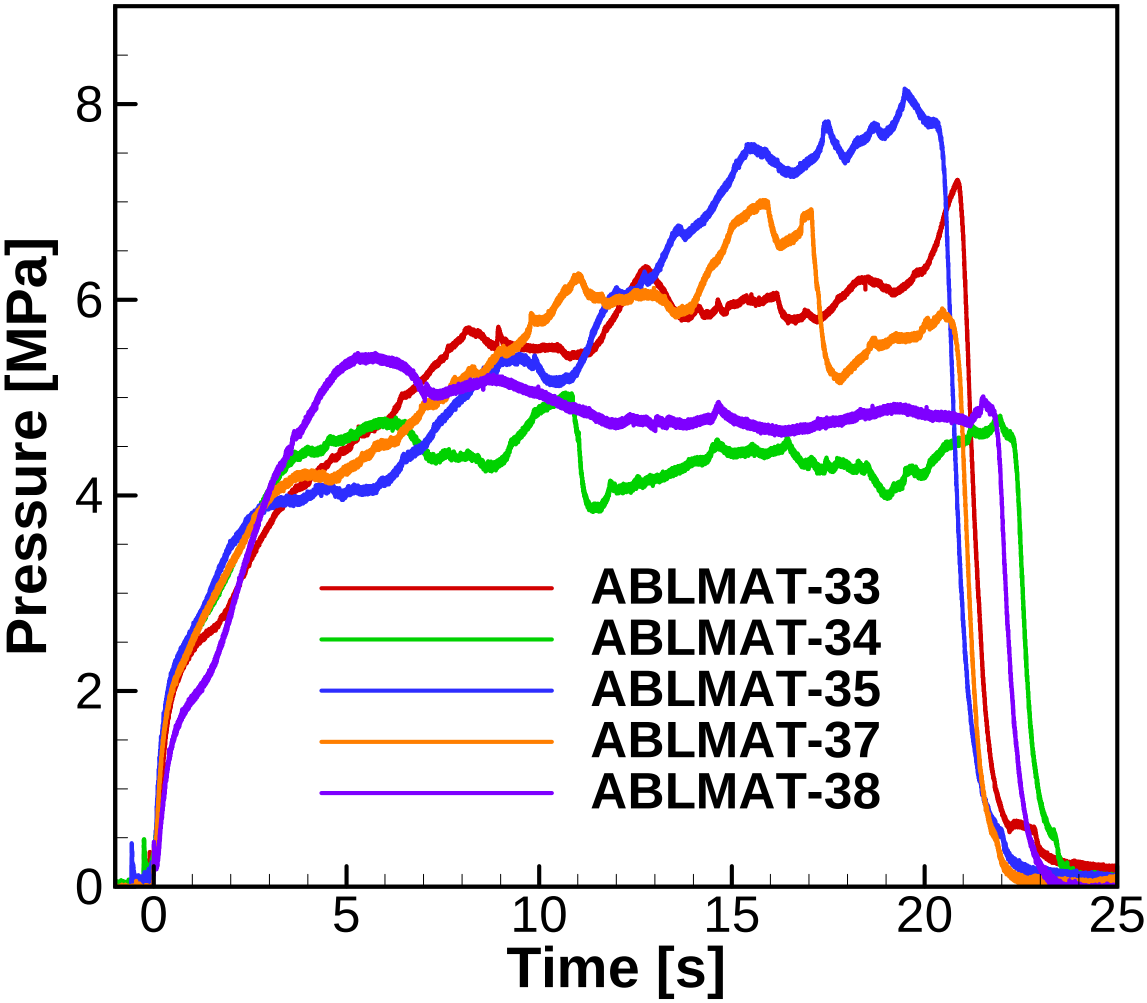

Figure 4-1. Chamber pressure histories from five of the six SRM firings

is subject to many sudden, sharp changes in pressure throughout the quasi-equilibrium portion of the firing, apparently due to the sudden accumulation or discharge of alumina deposits on the nozzle throat.

The variation in the pressure histories among the SRM firings led to variations in average chamber pressures and total firing durations as shown in Table 4-I. Since no pressure data was acquired for Test #ABLMAT-36, its firing duration was determined from its thermal radiation flux history as acquired from the radiometer. The average chamber pressure of Test #ABLMAT-36 was then determined by fitting the P_c vs. Δt data from the other five firings with a least-squares regression line then using this model to determine the average chamber pressure for Test #ABLMAT-36 from its firing duration. In addition to the firing durations and average chamber pressures, Table 4-I displays the adiabatic flame temperature (and, thus, assumed free-stream temperature of the combustion product flow in the SRM), density, dynamic viscosity, and Prandtl number of the combustion products as calculated with NASA CEA [86] for combustion of TP-H1148 for the average chamber pressure of each SRM firing. The tabulated free-stream flow channel velocities were calculated by simply dividing the solid propellant grain mass by the firing duration to determine the average combustion product mass flow rate then dividing this value by the product of the flow channel area and the density of the combustion products. The Reynolds numbers were calculated using the densities, free-stream velocities, and dynamic viscosities listed in the table along with a length scale equal to the distance from the leading edge of the graphite slab to the downstream edge of the ablative material samples (22 cm). As the values of the Reynolds numbers given in Table 4-I do not exceed the usual critical Reynolds number of 5×10^5 for transition to fully turbulent flow, it may be expected that the flow in the SRM test section remains primarily laminar; nevertheless, the SRM environment contains too many sources of fluctuations and instabilities to permit the existence of a perfectly smooth, laminar flow, and is, therefore, considered to be, if not fully turbulent, at least a sort of transitional hybrid flow.

Table 4-I. Properties of the internal environment of the subscale SRM

Test No.	Δt [s]	P_c [MPa]	T_∞ [K]	ρ [kg/m^3]	u_∞ [m/s]	μ [Pa-s]	Re_L	Pr
ABLMAT-33	20.9	5.14	3599	5.3984	14.2	1.19E-04	1.4×10^5	0.4136
ABLMAT-34	22.4	4.21	3576	4.4375	16.1	1.18E-04	1.3×10^5	0.4125
ABLMAT-35	20.3	5.50	3607	5.7606	13.8	1.19E-04	1.5×10^5	0.4139
ABLMAT-36	22.2	4.33	3580	4.5587	15.9	1.18E-04	1.4×10^5	0.4127
ABLMAT-37	20.9	5.15	3599	5.4055	14.3	1.19E-04	1.4×10^5	0.4136
ABLMAT-38	21.9	4.55	3585	4.7866	15.4	1.18E-04	1.4×10^5	0.4129

4.2. *Time-Resolved Ablative Material Decomposition Behavior*

4.2.1. *Ablative Decomposition and Charring Behavior of CFEPDM*

The images acquired via X-ray RTR from the six subscale SRM firings reveal that upon heating under SRM conditions, the decomposition of the polymer matrix generates a porous char layer that continuously swells throughout the duration of heating, such that the thickness of the sample is continually increasing while it is continually losing mass. As illustrated by the y = 0 location for the CFEPDM sample in Figure 3-11, the heated surface of the char layer has advanced into the SRM flow channel between the ablative material samples, while the char-virgin interface has receded. This phenomenon is elucidated in more detail in Figure 4-2, where the average location histories of the char surface and char-virgin interface are plotted and show simultaneous monotonic *y*-position increases for the char surface and decreases for the char-virgin interface. The uncertainty in the X-ray-RTR-derived *y* locations of the char surface and char-virgin interfaces presented in each of the foregoing figures is ±0.04 normalized units. Interestingly, while the char-virgin interface histories exhibit a decreasing-magnitude slope with increasing time, due to increasing thermal insulation from the ever-thickening char layer, the rate of

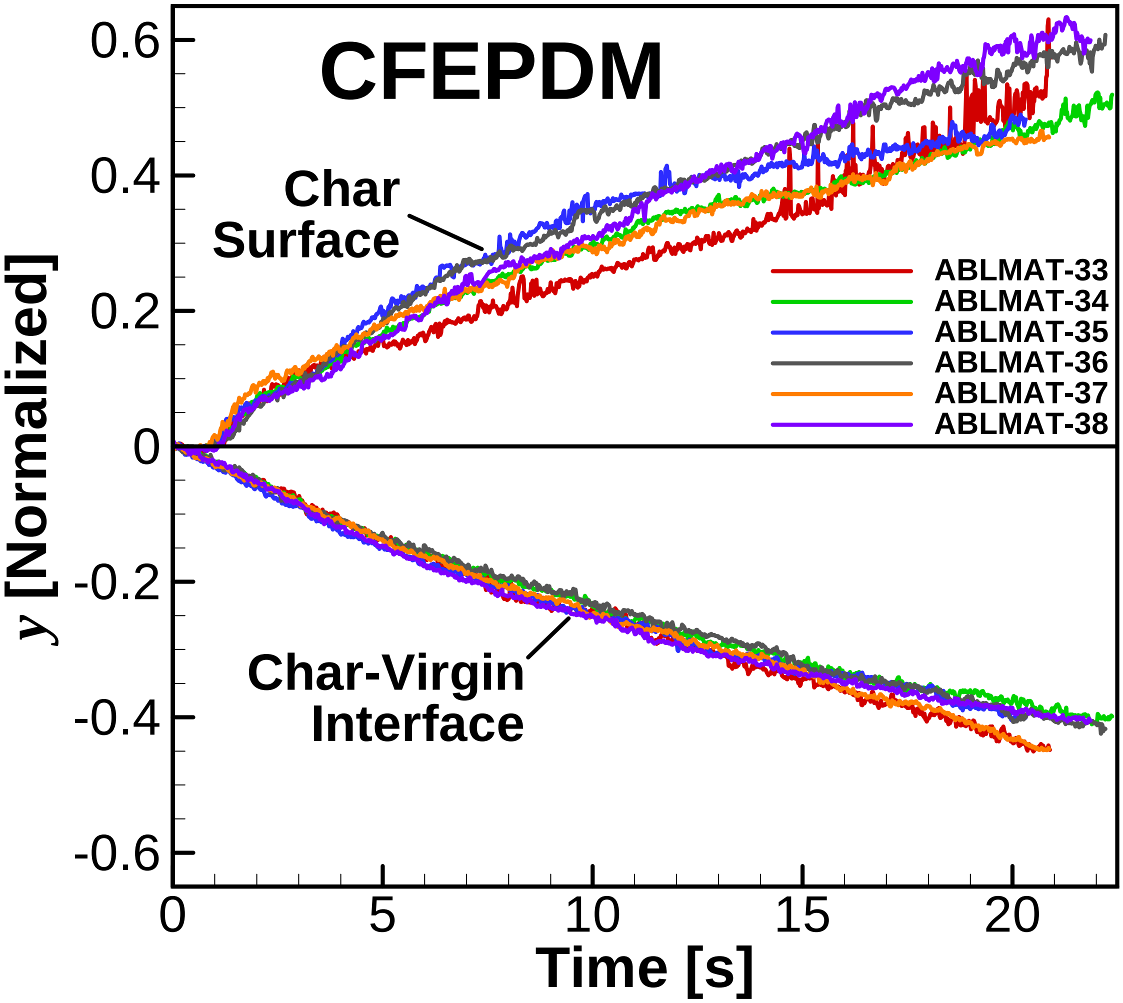

Figure 4-2. Average *y* location histories for CFEPDM samples for all SRM firings

expansion of the char surface does not necessarily exhibit a decreasing slope as time increases for all cases.

As evident from the X-ray images shown in Figure 4-3, as the char layer of the CFEPDM sample develops, the portion nearest the heated surface becomes darker, not only relative to the portion nearer the virgin material, but also in absolute terms: a fact which indicates that the near-surface region of the char layer is becoming denser as time progresses. This observation is consistent with coking behavior, which has been observed to occur in the char layers of ablative materials and is due to the precipitation of carbon from the pyrolysis gases onto the porous char through which they must pass to escape from the material [92]. This increasingly-dense surface layer is less permeable to the pyrolysis gases and, therefore, is likely increasing the pore pressure within the char layer, which could be driving the continued movement of the char surface in the *y* direction. For a longer-duration SRM firing, increasing pore pressure could eventually lead to wholesale sloughing of the char layer from the CFEPDM sample, as the

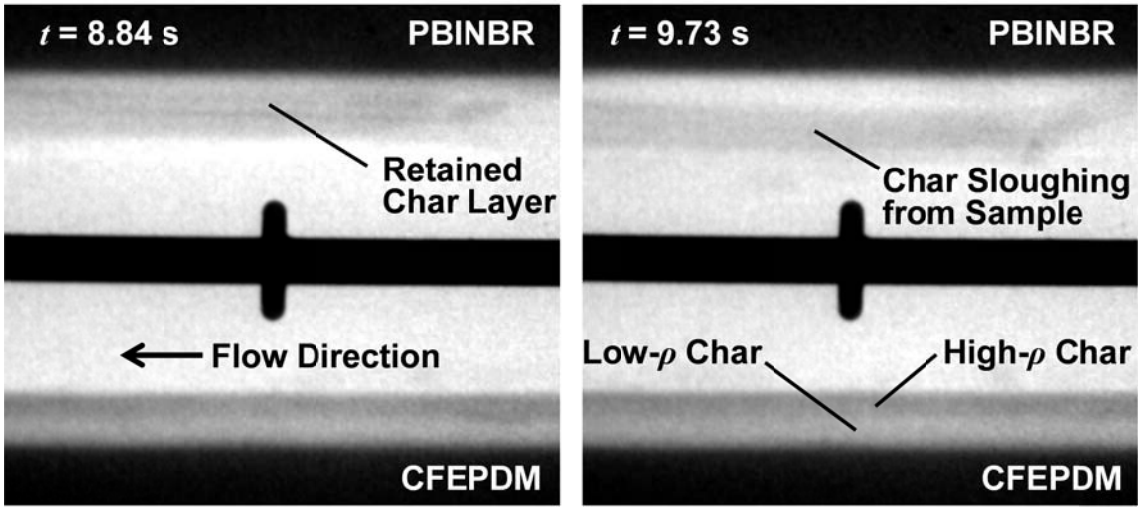

Figure 4-3. Two post-processed X-ray radiographs from Test #ABLMAT-34 depicting the observed behavior of the char layers for each ablative material type

mechanical stress due to the pressure differential through the char layer overcomes the tensile strength of the char.

Due to the continual movement of the char surface into the flow channel, it was impossible to determine from the X-ray RTR images precisely how much, if any, erosion of the char surface was occurring. A CFEPDM sample was included in only one of the 3-s CP-grain-configured SRM firings used for instrumentation testing, but, unlike the samples tested in the end-burning-grain-configured firings, it demonstrated a noticeable amount of erosion – the final thickness of the sample was thinner than the initial thickness. Given that the velocity of the combustion products in the test section flow channel was about 123 m/s for the CP-grain-configured firings (~8× that of the end-burning-grain-configured firings), and the measured heat fluxes were between 5 and 6× those measured in the end-burning-grain-configured firings, dramatically augmented erosion of the CFEPDM sample under the conditions present in the CP-grain-configured SRM is to be expected. It should be noted that the average chamber pressure in the SRM for the CP-grain-configured firing in which the CFEPDM sample was tested was 4.40 MPa, which falls within the range of those of the end-burning-grain-configured firings. Therefore, perhaps in certain regions in an SRM where adequate viscous shear forces and heat transfer are present, CFEPDM will experience surface erosion that is sufficiently fast to overcome its char surface expansion mechanism, and the insulation thickness will continually decrease, rather than increase, as observed in the end-burning-grain-configured subscale SRM firings.

4.2.2. Ablative Decomposition and Charring Behavior of PBINBR

As shown in Figure 4-4, at early times (< approx. 3 s) during an SRM firing, the charring behavior of the PBINBR samples appears very similar to that of the CFEPDM samples: as the material decomposes a char layer forms whose surface advances into the SRM flow channel while the char-virgin interface recedes into the sample. In fact, as evident in Figure 4-5, the char layer thicknesses developed for the two materials are approximately equal for the first 2.6 s of SRM operation. However, after the char layer

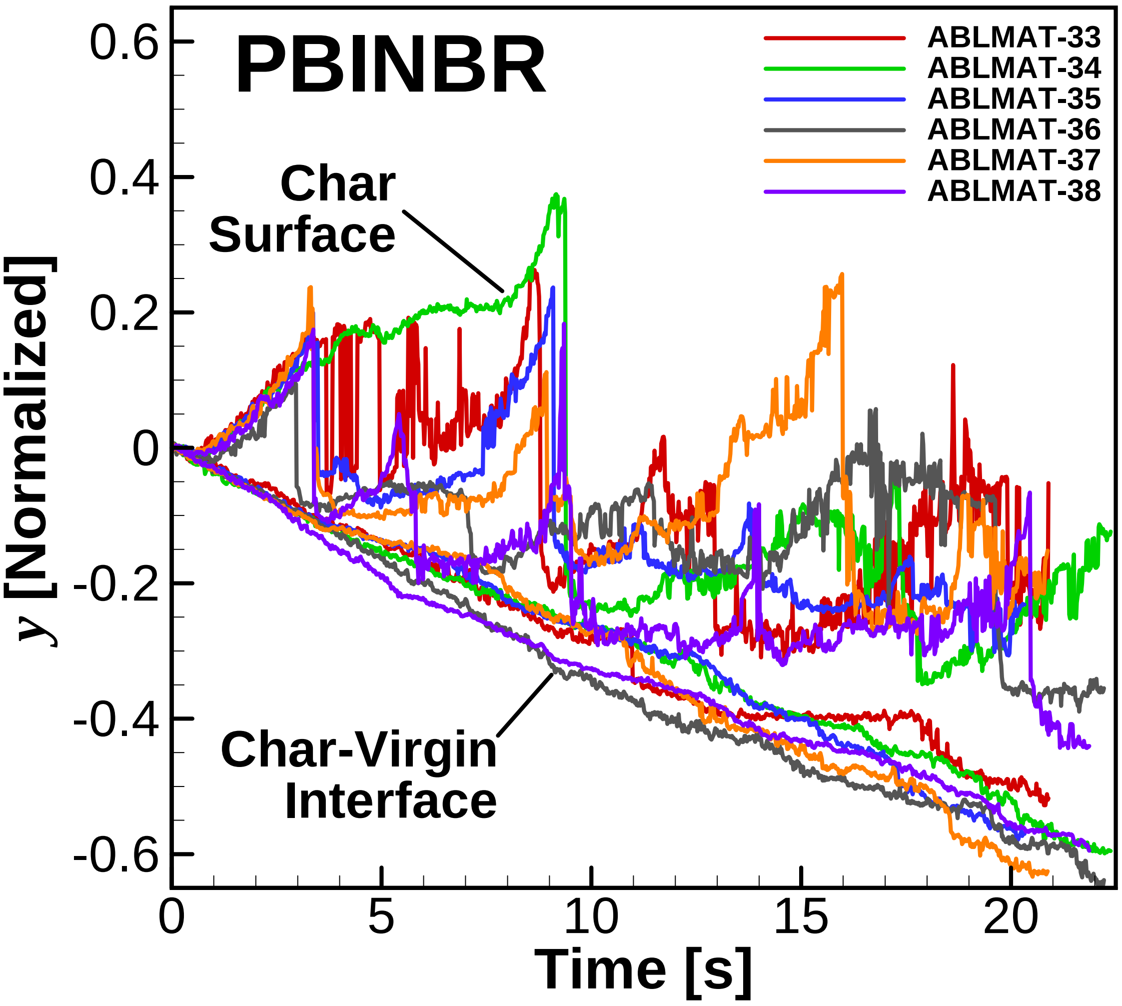

Figure 4-4. Average *y*-location histories for PBINBR samples for all SRM firings

attains a particular thickness, it suddenly sloughs from the sample, exposing the practically virgin material beneath. This sloughing phenomenon is illustrated by the two X-ray images in Figure 4-3, one of which shows the PBINBR sample exhibiting a thick char layer on its surface and the other from 0.89 s later in the same SRM firing showing the charred material being discharged from the surface. This process occurs repeatedly throughout the duration of an SRM firing, as demonstrated by the char thickness histories from Test #ABLMAT-37 in Figure 4-6 where three sloughing events occur during the course of the firing.

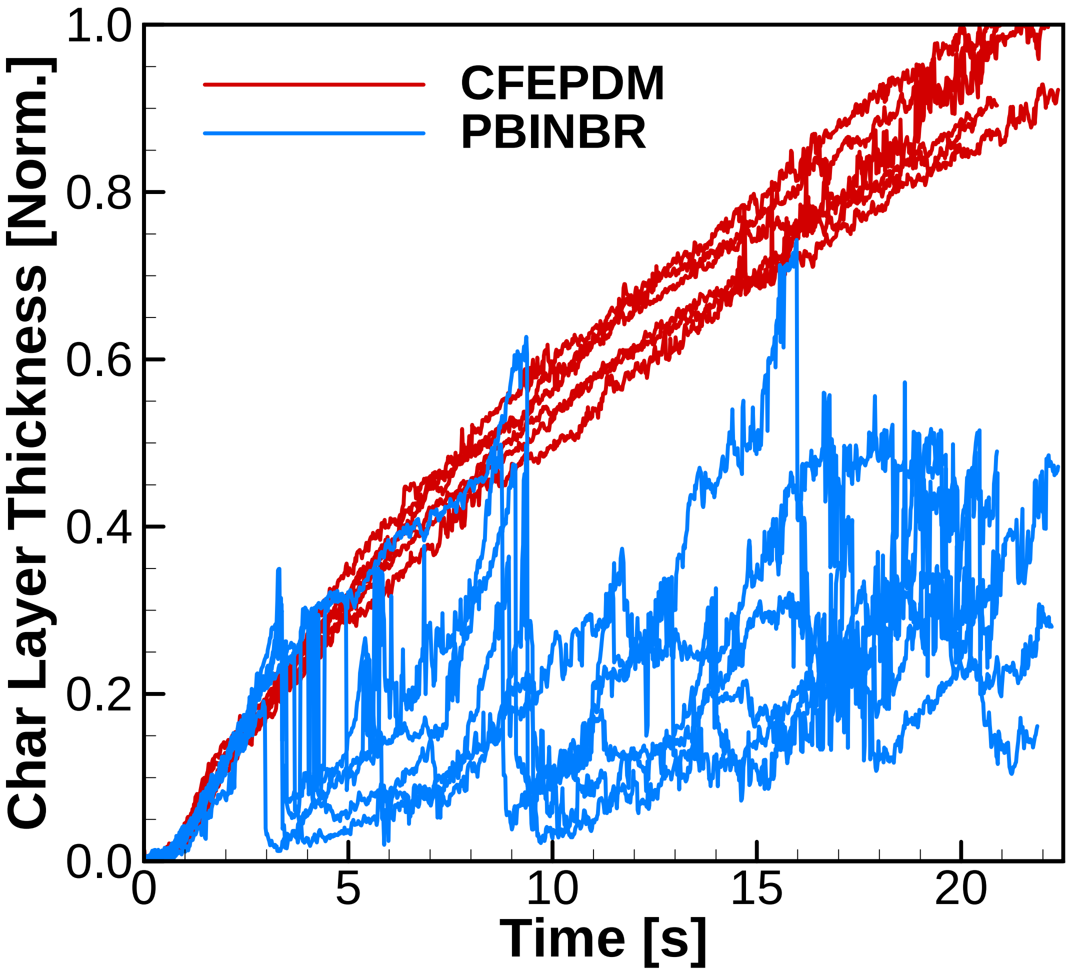

Figure 4-5. Char layer thickness histories for CFEPDM and PBINBR for all SRM firings

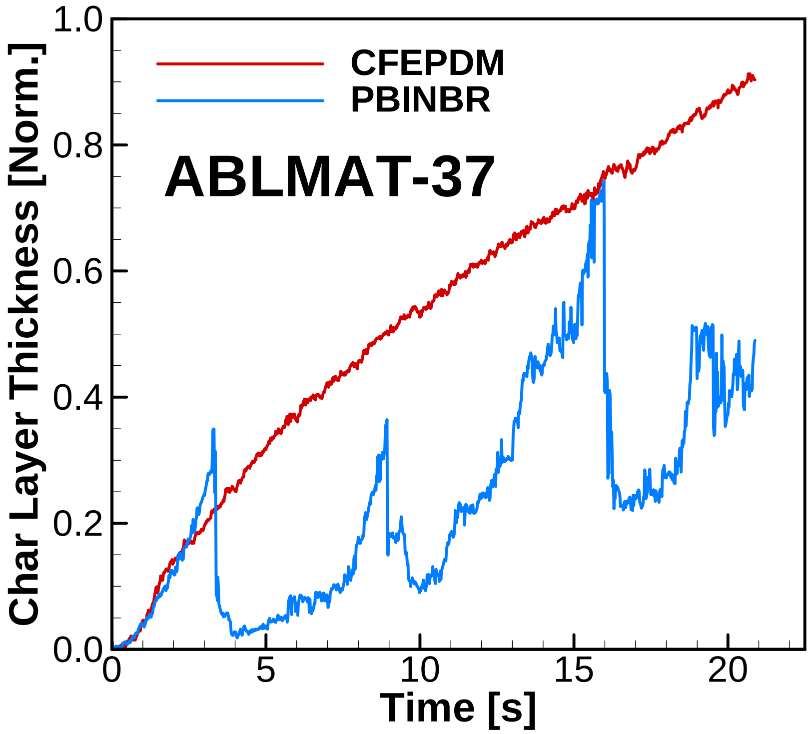

Figure 4-6. Average char layer thicknesses for CFEPDM and PBINBR from Test #ABLMAT-37

Also visible from the data in Figure 4-6 is a trend of increasing amounts of charred material remaining on the surface of the PBINBR sample after each successive sloughing event. This trend is present to some degree in each of the other five SRM firings in addition to Test #ABLMAT-37 and is possibly due to the presence of an increasingly full density profile within the char, which broadens the region of partially decomposed material between the fully charred and virgin regions that is still sufficiently dense (and, thus, has sufficient mechanical strength) to be retained on the sample, yet insufficiently dense to be considered “virgin”. However, it is also possibly illusory, due to the fact that each X-ray image displays the *z*-direction-averaged density of the ablative material, yet the erosion behavior of the material is not strictly constant in the *z* direction. One potential cause of the illusory, yet apparently increasing amount of post-slough char is that the sloughing events do not necessarily occur instantaneously or evenly across the entirety of the sample, as illustrated by the first sloughing event occurring in Test #ABLMAT-33 shown in Figure 4-7. In this firing, the char layer sloughs completely from the x_1 location about 3 sec into the firing, while the char layer continues to grow at the x_3 location, and the indicated char layer thickness at the x_2 location dithers between the x_1 and x_3 thicknesses. In this instance, only the upstream portion of the char layer was discharged from the sample. The boundary between the downstream region where the char was retained and the upstream region where the char was removed is not constant in the z direction, resulting in decreased contrast in the X-ray image at the x_2 location. Post-test observations of the fired samples reveal both large areas that are rather evenly eroded as well as smaller patches where additional sloughing has occurred, which further supports the evidence of non-uniform sloughing present in the X-ray images. As time progresses in an SRM firing, the non-uniformity of the char surface increases, resulting an increasingly vague surface location appearing in the X-ray images, which could be construed as char.

Another potential cause of an illusory, yet the apparently increasing amount of post-slough char is the effect of the boundary layers of the flow along the side walls of the flow channel, which cause char to be retained at the edges of the ablative material samples in excess of that retained nearer the center of the flow channel. This edge effect is exacerbated in SRM firings that use the radiometer, as the relatively cool hydrogen shield gas is essentially injected along one of the side walls of the flow channel, thickening that boundary layer and reducing its temperature and concentration of oxidizing species. The z-direction variation in char surface location induced by this edge

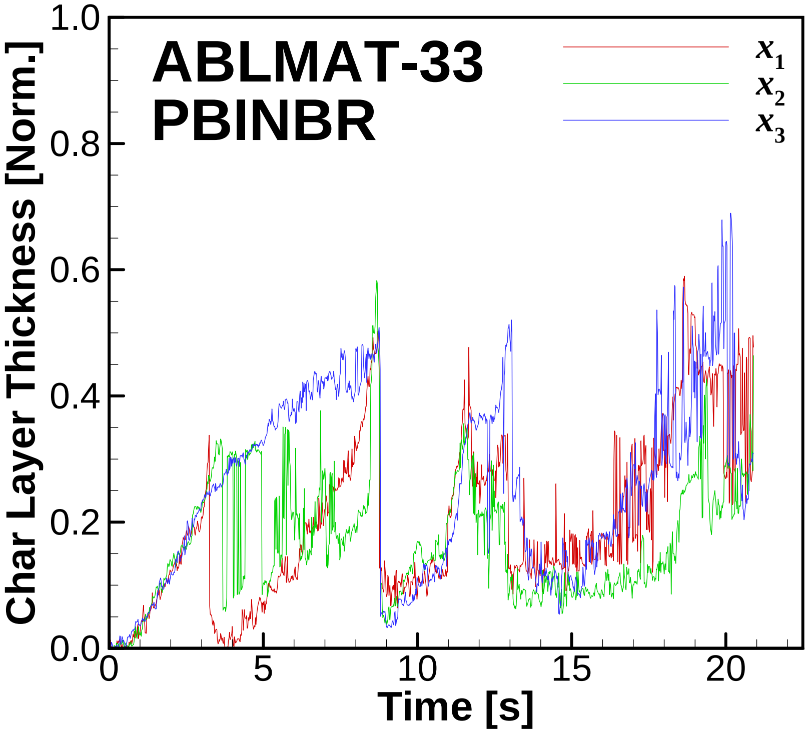

Figure 4-7. Char layer thickness histories for each *x* location on the PBINBR sample measured in Test #ABLMAT-33

effect decreases the contrast between the char surface and combustion product flow, which could appear in the image as additional char thickness. As the magnitude of the edge effect increases as an SRM firing progresses in time, it becomes another potential culprit to cause an illusory increase in the perceived thickness of post-slough char.

In addition to decreasing the contrast between the heated surface of the char and the combustion product flow, the retention of surplus char in the region near the flow channel wall, combined with the fact that the PBI fibers are primarily oriented in the *z* direction, can cause a sheet of charred material that has been sloughed from the sample in the mean-flow region of the flow channel to remain anchored to the sample near the flow channel wall. Based on their appearance in the X-ray images, the resulting char flaps may be sustained for several seconds, potentially reducing the heat transfer to the area of the sample directly below them. Such a char flap is evinced in Figure 4-8 at the x_1 location between about 11 and 14 sec, where y varies between about -0.10 and 0.55 normalized units due to the existence of a flap that detached from the surface at about 9.5 sec. This rapid cycling of the y value should not be regarded as mere noise, as both locations represent physical features present in the X-ray radiographs, but features that are likely not constant in the z direction and therefore appear equally plausible to the edge detector, as both are likely true, but at different z locations.

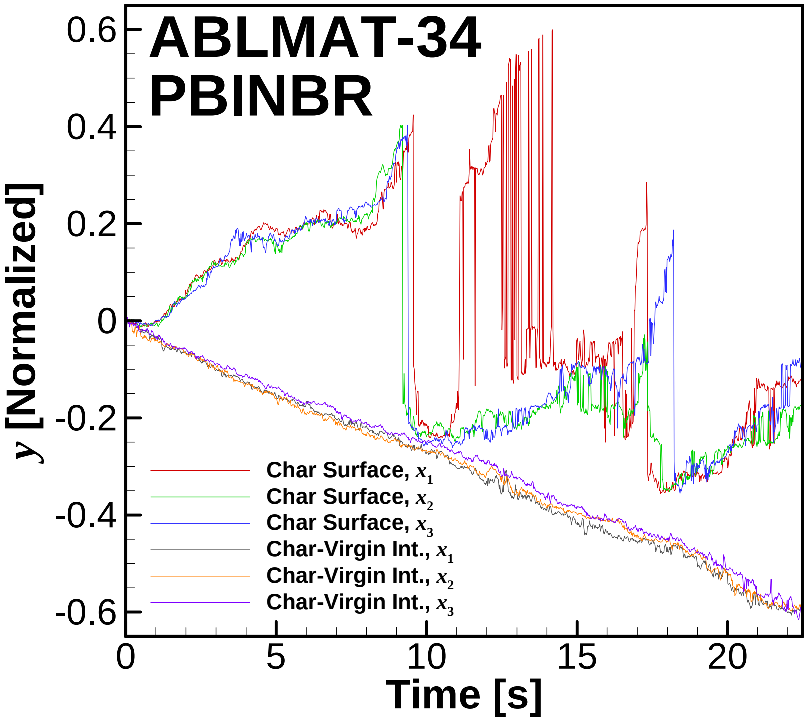

Figure 4-8. Plot of both char surface and char-virgin interface *y* location histories for the PBINBR sample in Test #ABLMAT-34

4.2.2.1. Mechanism of Char-Sloughing Events

The occurrence of char sloughing from the PBINBR samples is likely due to the structure of the material. PBINBR is fabricated by mixing chopped PBI fibers into uncured NBR, which is then extruded into relatively thin sheets and cured. The extrusion of the PBINBR sheets causes the PBI fibers to become preferentially oriented in the direction of the extrusion, that is, in the plane of the sheet. To produce the requisite thicknesses for SRM use, these sheets are adhesively bonded to one another; therefore, no mechanical linkage exists between adjacent plies in the material. This type of installation results in the PBI fibers being oriented largely perpendicular to the direction of char formation, and, thus, incapable of supporting the char layer beyond the thickness of a single ply; therefore, once the char layer attains this thickness, the shear stress imposed by the flow peels it from the sample.

As seen in the average char thickness histories displayed in Figure 4-9, the X-ray-RTR-derived char layer thickness occurring immediately prior to a sloughing event is rather inconsistent both within a particular SRM firing as well as among the various SRM firings. This fact may simply indicate inconsistencies in the control of the PBINBR manufacturing process, or it may imply that the sloughing mechanism is augmented or diminished by additional factors, such as decomposition of the PBI fibers, pore pressure, coking reactions, or non-one-dimensional effects.

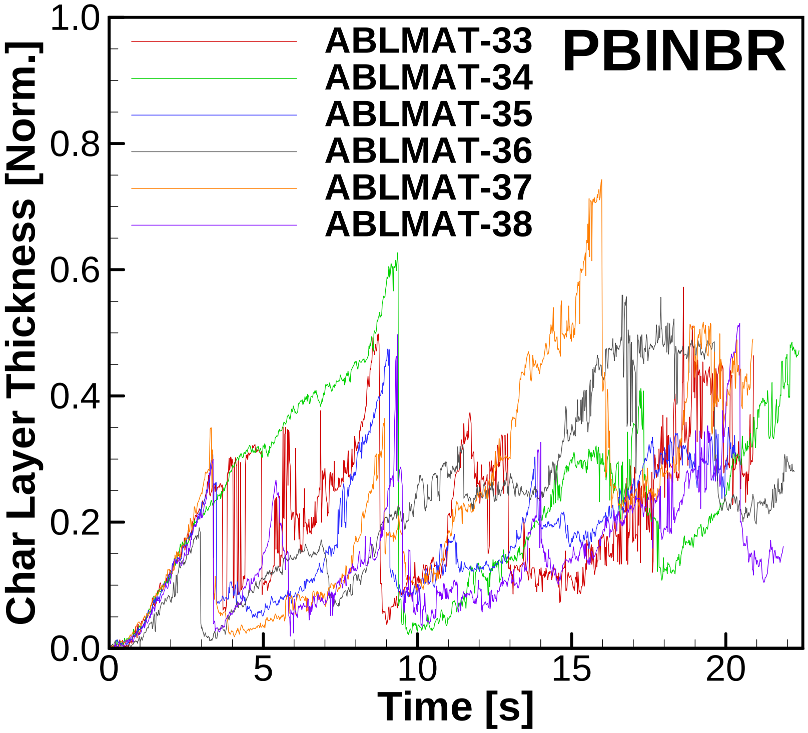

Figure 4-9. Normalized *x*-averaged char layer thickness histories for PBINBR samples in each subscale SRM firing

4.2.3. Comparison of Material Heat-Affected Depths

The repeated removal of a PBINBR sample's thermally-insulating char layer has an obvious impact on the depth of the heat-affected region within the sample. This heat-affected depth is characterized by the *y* location of the char-virgin interface, the history of which, in Figure 4-8, can be seen to experience noticeable increases in the magnitude of its slope in response to char-sloughing events. The effects of the sloughing events are cumulative and are the primary reason for the poor performance of the PBINBR vis-à-vis CFEPDM, as shown in Figure 4-10, which displays the char-virgin interface *y* location histories for each ablative material averaged over all six SRM firings overlaid on the *x*- location-averaged histories for each SRM firing. The average char-virgin interface *y* location, and, thus, heat-affected depth for the PBINBR samples is 39% greater than that of the CFEPDM sample after 20 s of SRM operation. In addition, due to the inconsistency of the sloughing mechanism, the spread of char-virgin interface histories among the individual SRM firings is considerably wider for the PBINBR data than for the CFEPDM data, indicating that the total heat-affected depth for the PBINBR is less predictable than that for the CFEPDM as well.

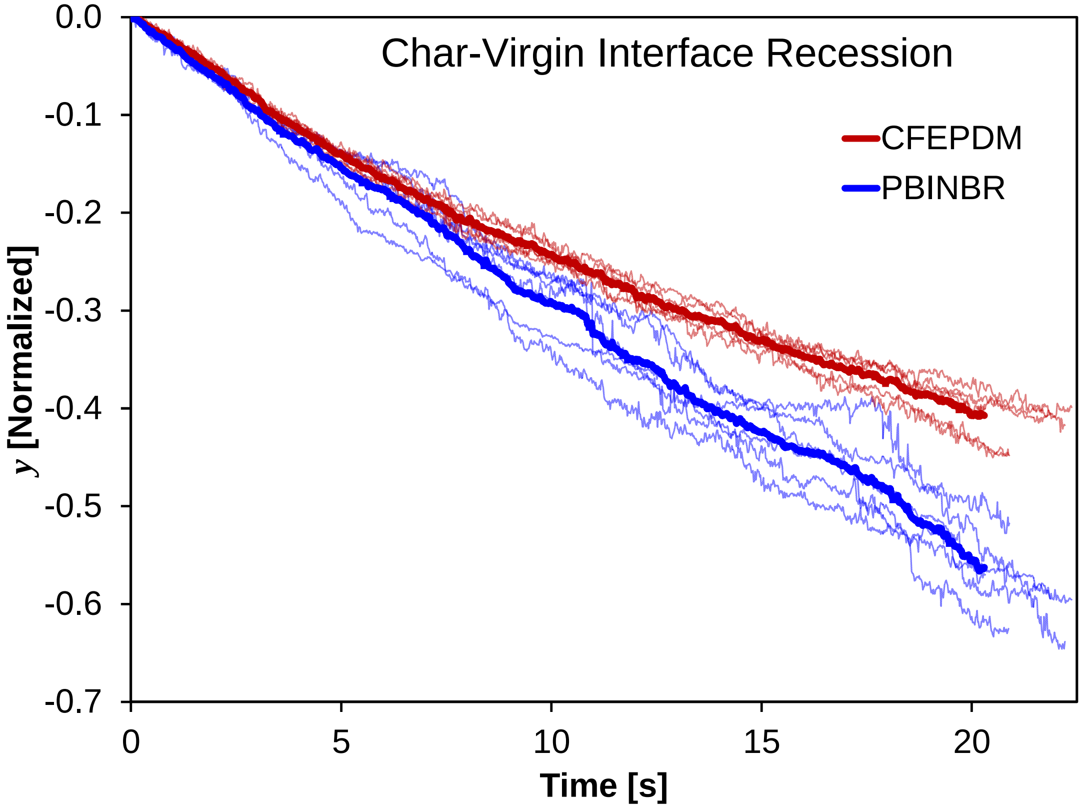

Figure 4-10. Average char-virgin interface *y* location histories for CFEPDM and PBINBR

It is interesting to note that, as shown in Figure 4-10, the average *y* location of the char-virgin interface of the PBINBR samples is deeper than that of the CFEPDM samples even prior to the first sloughing event, indicating that though the sloughing phenomenon is primary cause of the more profound heat-affected depths exhibited by the PBINBR samples vis-à-vis the CFEPDM samples. There also exists a difference in the properties of the matrix polymers, filler fibers, or char that would produce heat-affected depths for the PBINBR samples that are deeper than those for the CFEPDM samples in the absence of sloughing as well.

4.2.4. *Total Sample Mass Loss*

Each material sample was weighed before and after every SRM firing to determine the amount of mass lost due to ablative decomposition. The results of these measurements are included in Table 4-II, along with the average value for each material and its uncertainty reported at the 95% confidence level. Due to its superior char retention, the average mass lost from the CFEPDM samples is only 62% of that from the PBINBR samples.

Table 4-II. Mass loss from each sample from each SRM firing

	Total Mass Loss [Normalized]	
Test No.	CFEPDM	PBINBR
ABLMAT-33	0.576	0.806
ABLMAT-34	0.459	0.773
ABLMAT-35	0.543	0.847
ABLMAT-36	0.548	0.882
ABLMAT-37	0.605	0.878
ABLMAT-38	0.506	1.000
Average	0.540 ± 0.054	0.864 ± 0.083

4.2.5. *Effect of Radiometer Shielding Gas Flow on Sample Ablation*

As seen from the char-virgin interface histories for each tested material in Figure 4-2 and Figure 4-6, the total heat-affected depth for Test #ABLMAT-38 is about average for each material, indicating that the presence of the radiometer shield gas flow along the side wall of the SRM flow channel did not significantly affect the ablation of the samples. For PBINBR, the sample from Test #ABLMAT-38 exhibited the greatest mass loss of any of the PBINBR samples; nevertheless, the mass loss of the CFEPDM sample in Test #ABLMAT-38 was slightly less than average for the CFEPDM samples. Therefore, it is concluded that the radiometer shield gas flow did perhaps cause the PBINBR samples to retain more char in the near-wall region than they would in the absence of the flow, but that this effect was not sufficient to influence the average ablation behavior of the samples or its appearance in the X-ray images.

4.3. Subsurface Ablative Material Temperature Measurements

The normalized subsurface temperature histories plotted in Figure 4-11 are labeled according to their depth below the ablative material sample surface in normalized length units followed by the number of the test from which they were obtained. The histories for the PBINBR samples exhibit similar slopes regardless of initial depth for all firings, and the thermocouples seem to reliably break upon reaching the normalized temperature of 1.0. The normalized subsurface temperature histories acquired from the CFEPDM samples are plotted in Figure 4-12. For both materials, the timing of the measured temperature rises is generally ordered according to the embedded depth of the thermocouples, with the deeper thermocouples experiencing later temperature rises. In addition, for the thermocouples that remain intact throughout the firing, the deeper thermocouples exhibit lower maximum temperatures than those nearer the surface.

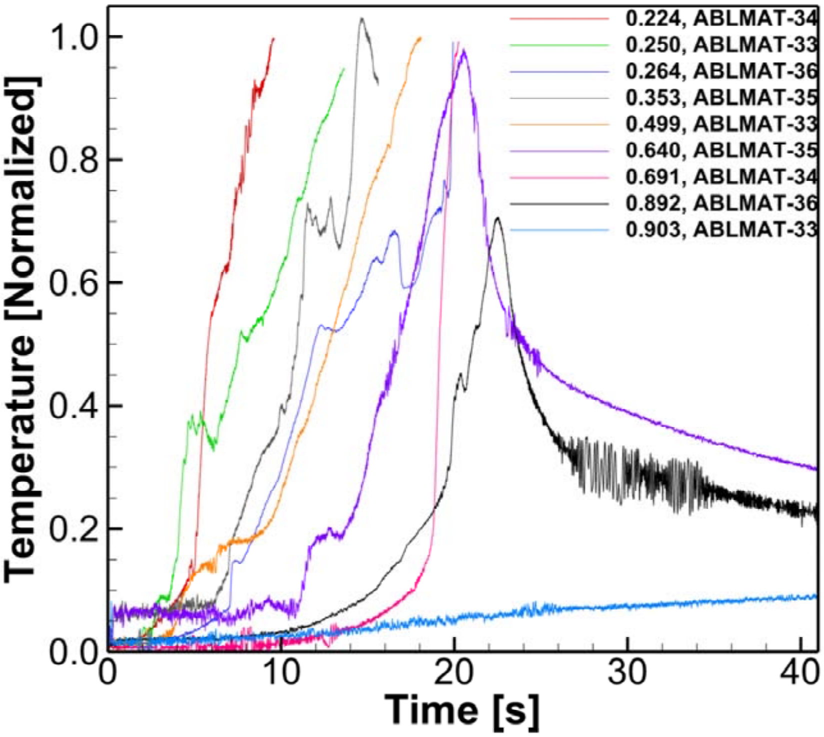

Figure 4-11. Subsurface temperature histories of PBINBR samples

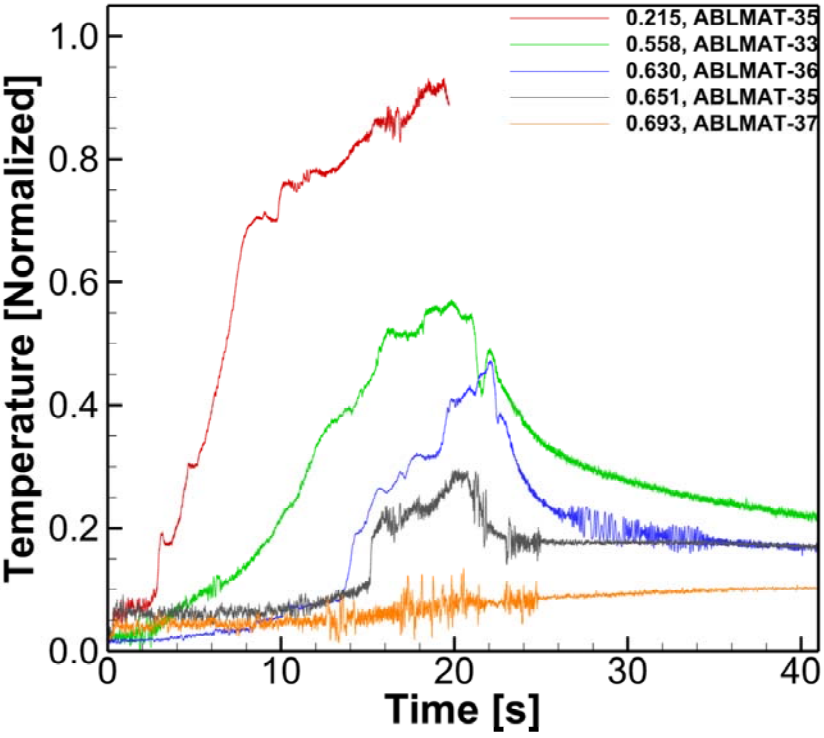

Figure 4-12. Subsurface temperature histories of CFEPDM samples

When the subsurface temperature histories plotted in Figure 4-12 are compared with the *y*-location histories of the their respective ablative material samples, it is found that the slope break in the temperature history for the 0.215-units-deep thermocouple embedded in the CFEPDM sample in Test #ABLMAT-35 corresponds to the time of arrival of the char-virgin interface at that *y*-location (8.6 s). This instance, however, the only one in which the char-virgin interface, as deduced from the X-ray images, reaches the depth of one of the thermocouples in one of the CFEPDM samples, as the deepest penetration of the char-virgin interface for any of the CFEPDM samples, as seen in Figure 4-2, was 0.444 units, while the second-shallowest thermocouple was positioned 0.558 units deep. For Test #ABLMAT-35, the 0.215-units-deep thermocouple was visible in the X-ray RTR images acquired during the firing once char-virgin interface had receded beyond its depth. Examination of these images revealed that, while the thermocouple remains in its initial horizontal orientation as the char-virgin interface is receding past it, the swelling of the char layer of the CFEPDM sample eventually causes the thermocouple to bend at its shoulder, resulting in the once-horizontal portion of the thermocouple wire acquiring an increasing angle relative to horizontal. This thermocouple-stretching process begins for the 0.215-units-deep thermocouple at approximately 17.8 s and continues until the thermocouple apparently breaks at about 19.7 s. From the X-ray images, it appears that the thermocouple bead actually moves faster in the positive-*y* direction than the char surface during this stretching, so that the bead is moving nearer to the char surface. The measured temperature history appears little affected by the movement of the thermocouple, as its slope remains essentially constant; however, the bending of the thermocouple wire induced by the swelling phenomenon is likely responsible for ultimately breaking the thermocouple.

For the PBINBR samples, four of the thermocouples are embedded at sufficiently shallow depths (0.224, 0.250, 0.264 and 0.353 units) to be crossed by the char-virgin interface during the course of a firing. For these thermocouples, the measured temperature histories do not exhibit a noticeable change in slope at the X-ray-RTR-indicated time of arrival of the char-virgin interface, as does the 0.215-units-deep thermocouple embedded in the CFEPDM sample in Test #ABLMAT-35; nevertheless, in the cases where a PBINBR-embedded thermocouple is visible in the X-ray images captured from the SRM firings (Tests #ABLMAT-34 and # ABLMAT-35), the breaking time of these thermocouples as apparent from the temperature data does reliably synchronize with char sloughing events observed in the thermocouple location in the X-ray images.

4.4. Total Heat Flux Gauges

4.4.1. Calculated vs. Measured Temperature Histories

In Figure 4-13, the temperature histories calculated by the IHCA for its estimated heat flux history are plotted with the thermocouple-measured temperature histories for a typical two-thermocouple case, ABLMAT-35 (1), and the lone three-thermocouple case, ABLMAT-36 (1). It is immediately apparent that for the two-thermocouple case, the calculated temperatures match the measured temperatures exactly for all intents and purposes. This is due to the fact that the thermocouples are located very near one particular surface of the sensor, while being rather far from the opposite surface, causing them to be very sensitive to one of the estimated fluxes and rather insensitive to the other. Therefore, each estimated heat flux history can be manipulated to match the calculated and measured temperatures for the nearest thermocouple location without materially affecting the temperature or flux on the opposite side. As ABLMAT-36 (1) recorded the measurement for the additional thermocouple near the front sensor surface, the estimated heat flux history was required to satisfy two measured temperature histories rather than one, and since the numerical model of the heat flux sensor is apparently imperfect, the calculated temperature histories do not match the measured ones exactly. The modeling imperfections that lead to the differences in the calculated and measured temperatures could include some combination of the following: opposite biases for the individual thermocouples, errors in thermal properties, and differences in thermal contact resistance between the thermocouple and the sensor graphite between the different thermocouples. Notwithstanding these imperfections, ABLMAT-36 (1) exhibits good agreement between

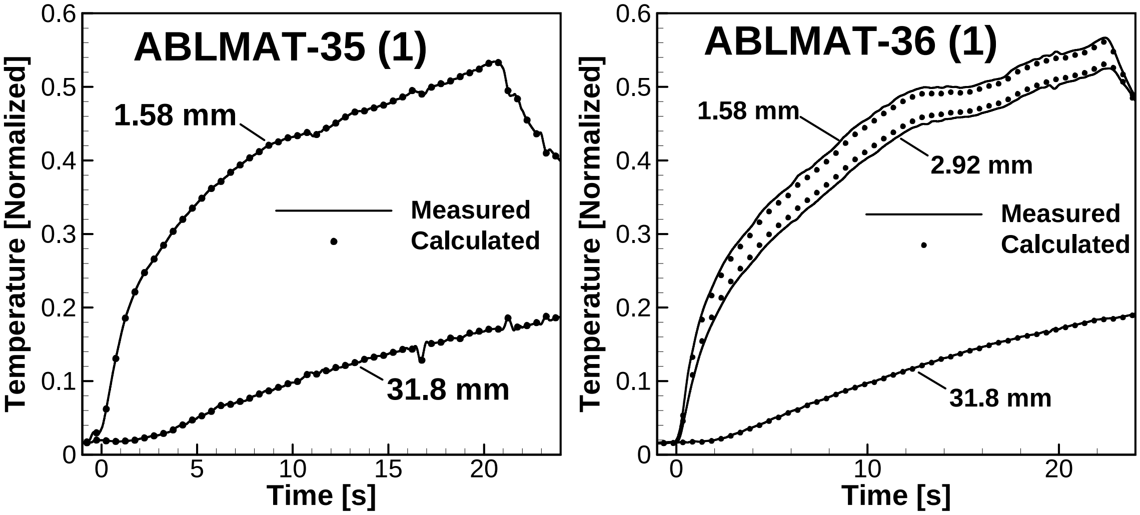

Figure 4-13. Comparison of measured and calculated temperature histories for two heat flux measurements

the measured and calculated temperatures and instills confidence in the capability of the IHCA to deduce the true surface heat fluxes.

4.4.2. Total Heat Flux Measurements

The ICHA-estimated heat flux histories for all sensors and SRM firings are displayed in Figure 4-14. The test-to-test variation among these histories (~±20%) is certainly well within reason given the test-to-test variability of general SRM conditions. While smoothing of the thermocouple-measured temperature histories prior to their use in the IHCA eliminated the effects of electrical noise on the IHCA-deduced quantities, the deduced heat flux histories still exhibit some apparent "noise", with the plotted curves having a jagged rather than smooth appearance. Comparisons of the heat flux histories with the smoothed temperature histories reveal that each of these jagged features in a given heat flux history corresponds to a feature in a measured temperature history that possesses a sufficiently long timescale that it cannot be dismissed as belonging to a non-thermal process. Another potential source of noise in the estimated heat flux histories is numerical instability of the IHCA code; however, the time-step size employed for these inverse calculations, 0.5 s, was specifically chosen because it was observed to be the smallest stable time-step during testing of the IHCA code and therefore cannot be the source of the ostensible "noise". It is the trend of each of the heat flux histories shown in Figure 4-14 to decrease with increasing time: a fact primarily due to the continually increasing surface temperature of the graphite, but perhaps also due to decreasing total enthalpy of the flow at the sensor location due to the recession of the burning surface of the end-burning solid propellant grain. During the course of an SRM firing, the distance between the burning surface of the propellant grain and the heat flux sensor more than doubles, increasing the surface area to which the combustion products can lose heat, and thus decreasing the sensible enthalpy of the products that arrive at the heat flux sensor location.

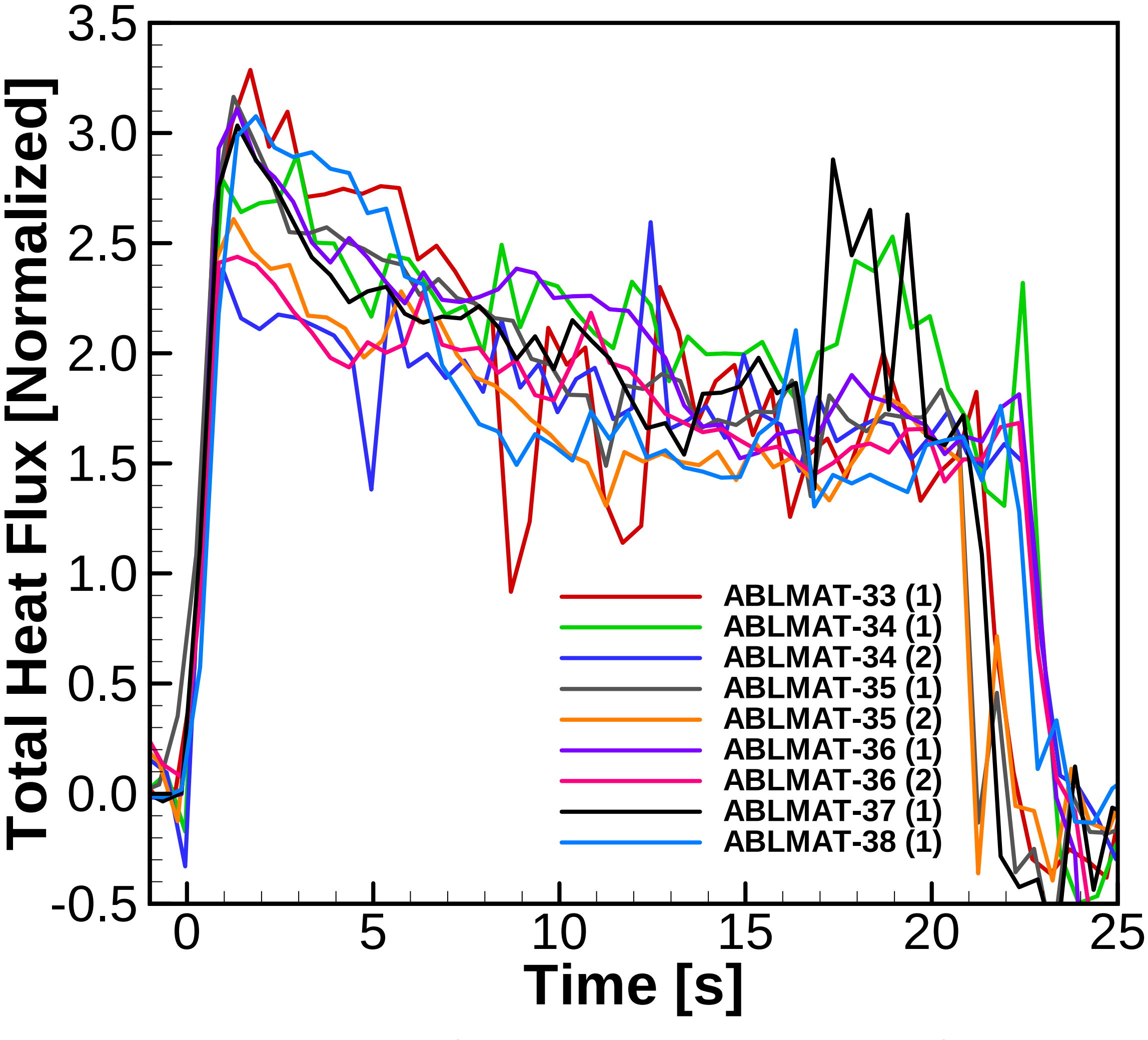

Figure 4-14. Total heat flux histories measured in six SRM firings

4.4.3. Surface Temperature Measurements

Having estimated the surface heat flux history and calculated the resulting temperature distribution throughout the graphite sensor, the IHCA computes the surface temperature of the sensor using a second-order extrapolation from the temperatures of the first two cells and the deduced surface heat flux. The resulting normalized surface temperature histories for each sensor in each SRM firing are displayed in Figure 4-15, and demonstrate the behavior commensurate with the corresponding total heat flux histories.

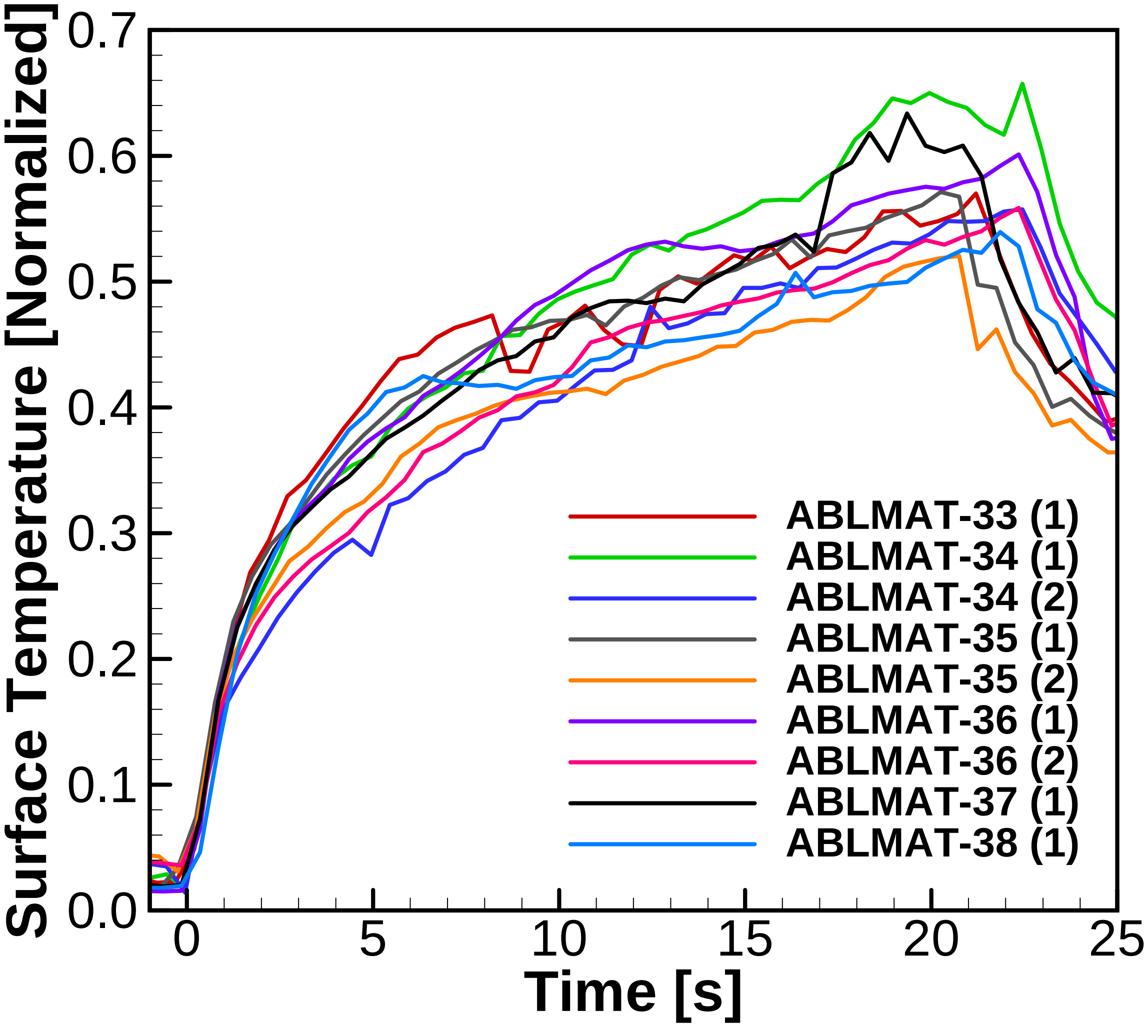

Figure 4-15. Surface temperature histories for each graphite heat flux sensor

4.4.4. Convective Heat Flux

The convective heat flux histories deduced from the measured total heat flux, graphite sensor surface temperature, and measured thermal radiation flux are displayed in Figure 4-16. For Tests #ABLMAT-35 and #ABLMAT-38, reliable thermal radiation measurements were not available; therefore, no convective heat flux histories were produced for those tests.

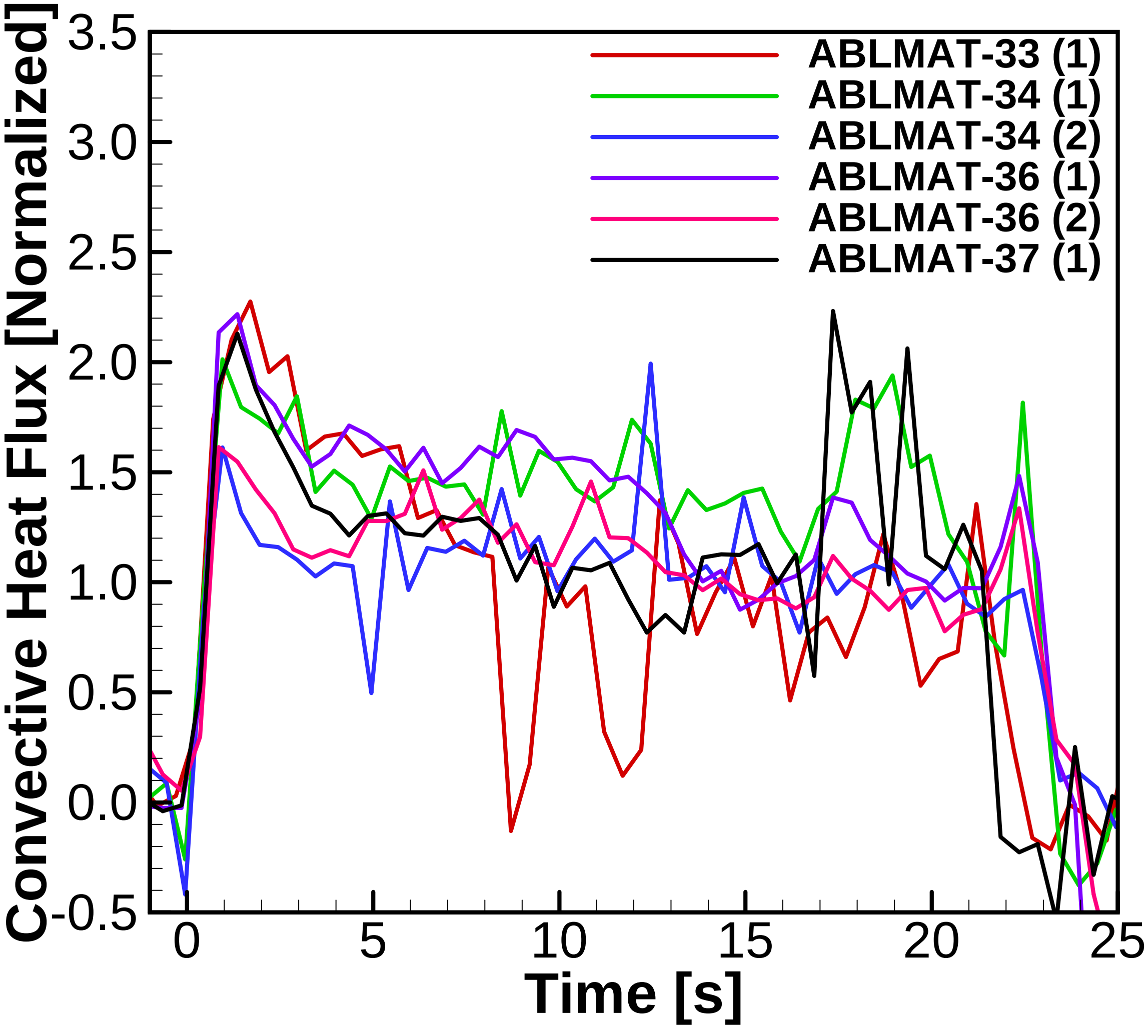

Figure 4-16. Convective heat flux histories deduced from total and radiative heat fluxes

Calculation of the dimensionless heat transfer parameters revealed that the calculated Nusselt numbers for Test #ABLMAT-33 (1), #ABLMAT-34 (2), and #ABLMAT-36 (2) are much (~24%) lower than those for the other three sensors. An examination of the convective heat flux histories in Figure 4-16 suggests that the two “dips” near 8 and 12 s in the ABLMAT-33 (1) trace are at least partially responsible for its low temporal average; however, if these are removed and replaced with interpolated values the average Nusselt number remained significantly lower than the those from Tests #ABLMAT-34 (1), #ABLMAT-36 (1), and #ABLMAT-37 (1). As all three of the sensors exhibiting the lower Nusselt number values were located on the same side of the flow channel, that nearest the radiometer, it is possible that they all were actually exposed to a reduced convective heat flux due to the nearby jet of relatively cold, radiometer shielding gas. While post-test observations of the graphite slab into which the total heat flux sensors were inserted indicate that the shielding gas jet does not pass directly over the total heat flux sensor, it may be sufficiently near to induce heat flow in a second dimension, and reduce the heat flux perceived by the sensor. Nevertheless, given the similarities in shape of the two convective heat flux histories deduced from Sensor #2 and the difference between those and that deduced from ABLMAT-33 (1), as seen in Figure 4-17, it seems more reasonable to conclude that there exists a bias between the two different sensors. Figure 4-18 displays the total heat flux histories for both sensors for each of the SRM firings in which data was obtained for two sensors. For each firing, the total heat flux histories share the same general shape, but with the total heat flux history measured by Sensor #2 being offset to slightly lower values than that measured by Sensor #1. The consistency of this offset among the SRM firings, despite differing measured total fluxes and radiometer shield gas flow rates as well as the close similarity of the shape of and features in the traces for the two sensors for each SRM firing suggests that this offset is due to inherent opposite biases in the two sensors, rather than an effect of radiometer shield gas flow.

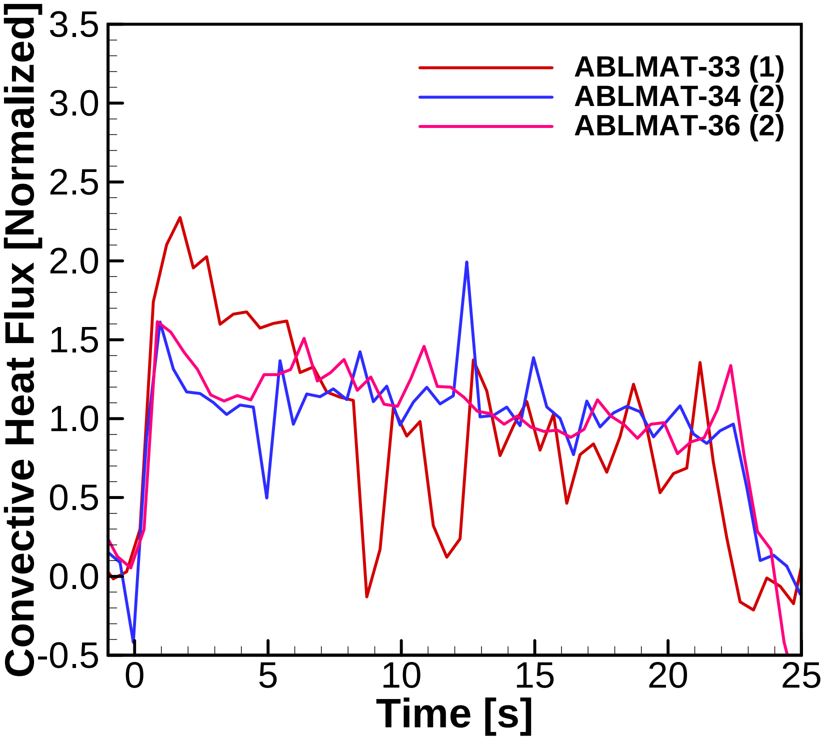

Figure 4-17. Convective heat flux histories for gauges located on the radiometer side of the SRM flow channel

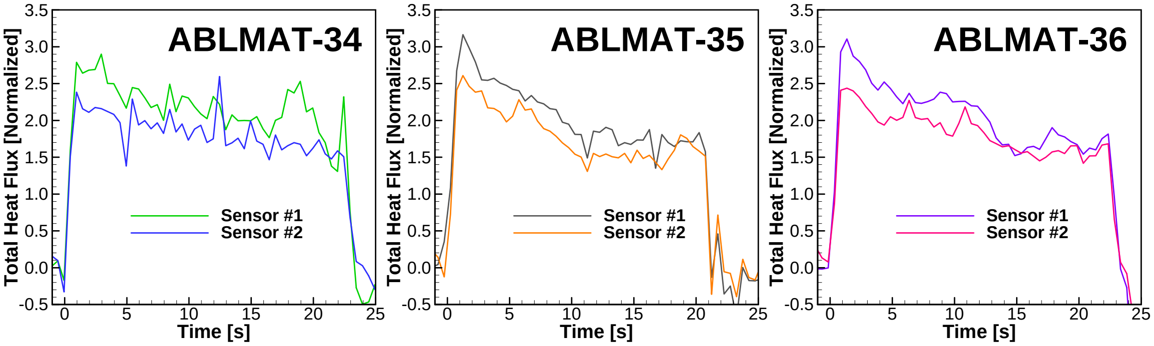

Figure 4-18. Comparison of the total heat flux histories from different sensors in the same SRM firing

4.4.5. Measurement Uncertainties

The results of the IHCA uncertainty analysis are shown in Figure 4-19 and Figure 4-20, where the calculated uncertainty intervals are displayed as thin solid lines above and below the total heat flux and surface temperature histories as computed from the data from Test #ABLMAT-35. For the period of the firing duration, the uncertainty in the estimation of the total heat flux due to the aforementioned uncertainties in the temperature measurements, thermocouple locations, sensor graphite density, and sensor graphite thermal conductivity averages 5% of the deduced flux at a particular time-step and is never greater than 7%. For the surface temperature, this uncertainty averages 1% and is never greater than 2%. These values indicate that these heat flux sensors are measuring the quantities of interest with a level of accuracy suitable to their purpose. These uncertainties, however, do not include the effect of uncertainties in the specific heat data and/or its regression model or certain imperfections in thermocouple installation such as thermal contact resistance between the thermocouple and the sensor graphite and the thermocouple wire not being installed perfectly parallel to the sensor surface. Nevertheless, this analysis accounts for the vast majority of the sources of uncertainty in the total heat flux and surface temperature estimates, and thus provides confidence in the accuracy of the results.

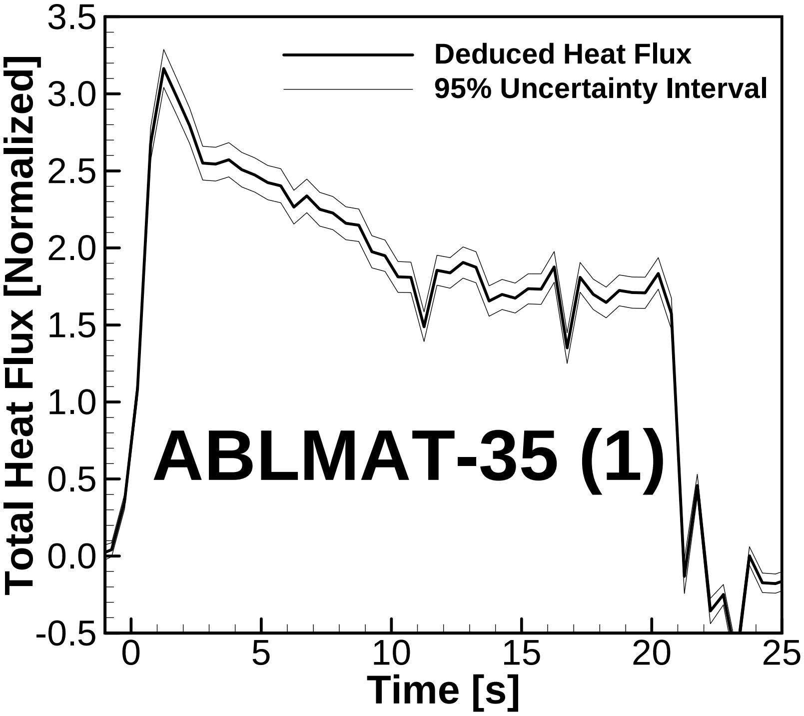

Figure 4-19. 95% uncertainty interval for deduced total heat flux and surface temperature for Sensor #1 Test #ABLMAT-35

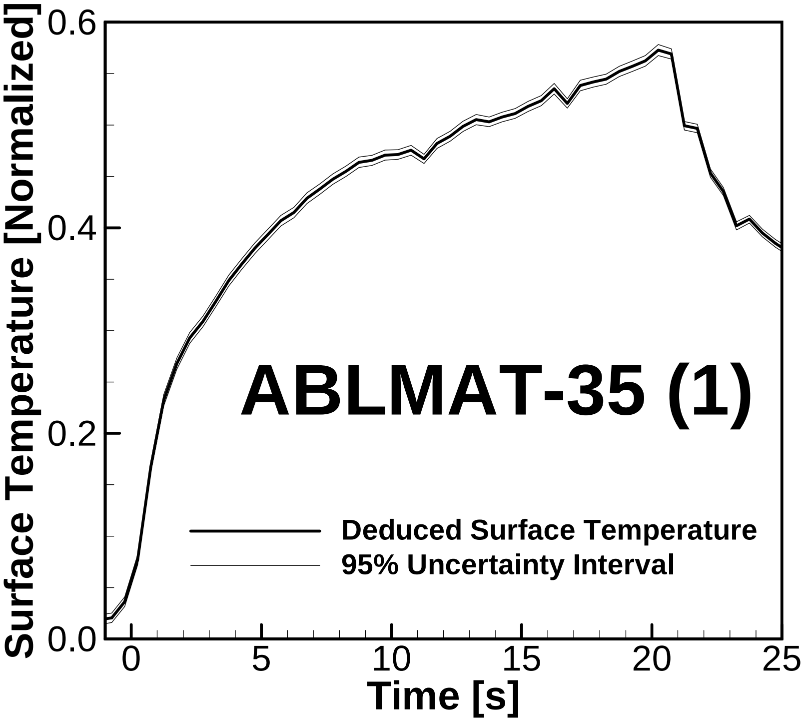

Figure 4-20. 95% uncertainty interval for deduced heat flux sensor surface temperature for Sensor #1 in Test #ABLMAT-35

4.5. Radiometer

4.5.1. Shield Gas Flow Rates

Figure 4-21 displays the pressure histories of the SRM chamber as well as those measured upstream of the critical flow orifice used to regulate the mass flow rate of the radiometer shield gas for four of the five firings of this series. The higher-than-design chamber pressures due to the thicker and more irregular alumina layer that formed on the inner diameter of the water-cooled nozzle had a profound impact on the mass flow rate of the radiometer shield gas, as the critical flow orifice clearly became unchoked about 6 s into the firing duration for Test #ABLMAT-33, causing the flow rate to be reduced from the design condition. In the post-test examination of the radiometer window, it appeared "dusty", having an irregular pattern of particles present on its surface. This coating of particles was sufficiently light that in its most heavily coated regions it remained translucent, while in other locations (including near the center) it remained transparent. In view of these results, the shield gas delivery system was modified to deliver a 1.4-MPa higher pressure upstream of the orifice, while the size of the orifice was maintained. The maximum chamber pressure achieved in Test #ABLMAT-34 was only 70% of that achieved in Test #ABLMAT-33, an effect that, combined with the higher pressure upstream of the orifice, allowed the orifice to remain choked throughout the duration of the firing. Nevertheless, upon post-test examination, the radiometer window appeared to be fouled in the same manner as in Test #ABLMAT-33. Further investigation led to the conclusion that the source of the fouling material was actually the shield gas feed system rather than the SRM chamber, so the feed system was cleaned thoroughly prior to Test

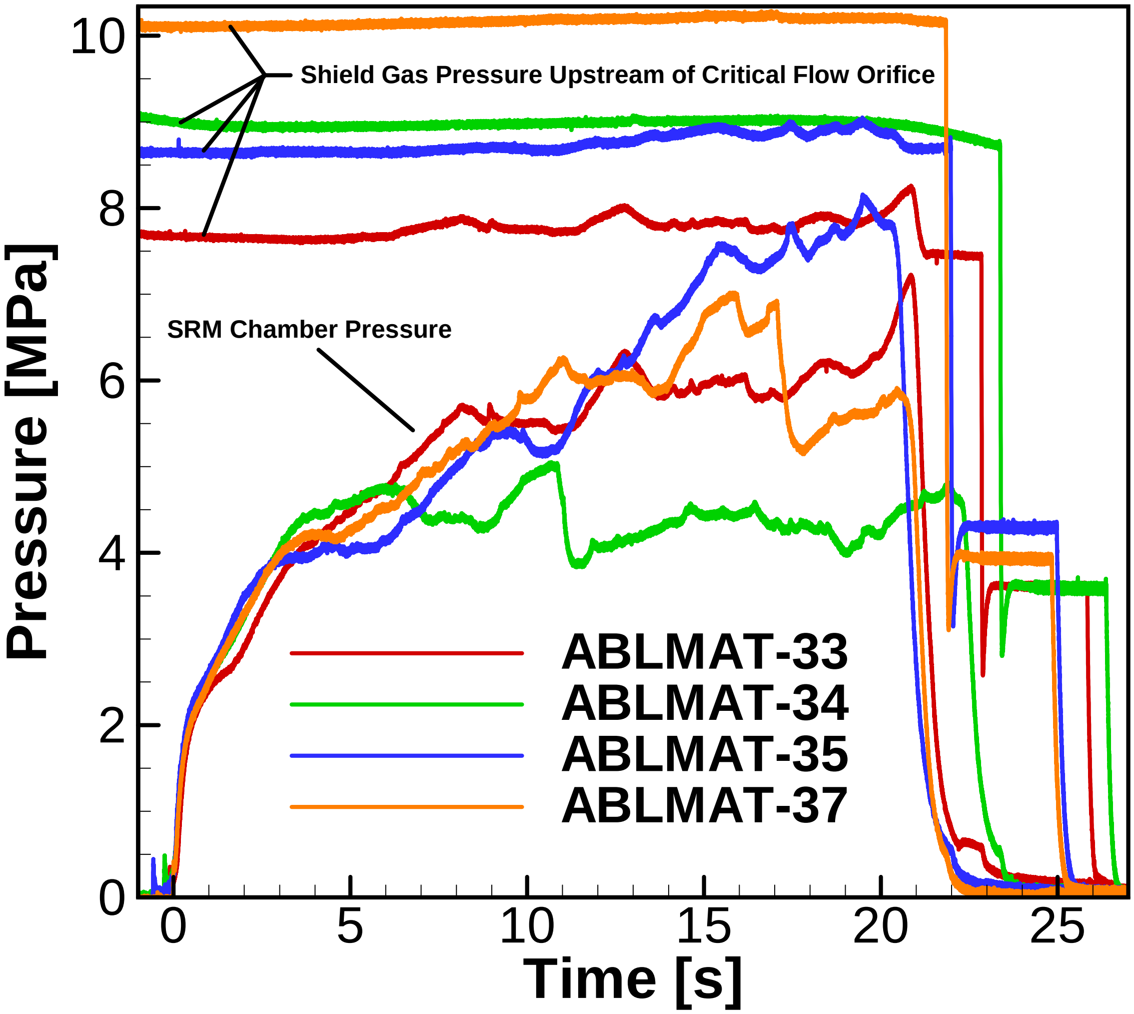

Figure 4-21. SRM chamber and critical flow orifice upstream pressure histories.

#ABLMAT-35. The maintenance of the high mass flow rate of shield gas throughout the firing in Test #ABLMAT-34, while beneficial for the operation of the radiometer, had a noticeable influence on the erosion of the ablative insulation samples located downstream of the radiometer; therefore, a smaller critical flow orifice was installed in the shield gas delivery system to inject a lower mass flow rate of cold hydrogen into the SRM while maintaining high upstream pressures to prevent unchoking of the orifice. The chamber pressure developed in Test #ABLMAT-35, however, was higher than either of the previous firings, unchoking the orifice and ultimately reducing the shield gas flow rate below its effective value, as evinced by the fact that the window was coated with an opaque layer of alumina. The pressure upstream of the orifice was then increased for Tests #ABLMAT-36 and #ABLMAT-37, which resulted in radiometer windows that remained absolutely clean throughout the firing. The orifice does appear to have become unchoked about 15 s into the firing duration of Test #ABLMAT-37, however, the increase in the upstream pressure was slight and this period lasted for only 2 sec. For the choked-flow condition of the orifice in Tests #ABLMAT-36 and #ABLMAT-37, the mass flow rate of the hydrogen injected into the SRM is 6.1 g/s.

4.5.2. Radiation Measurements

Figure 4-22 displays the dimensionless radiative heat flux histories measured from the five test firings performed in this series. The sharp increases and decreases in these radiation histories correspond exactly to the initial pressurization and final depressurization events, shown in Figure 4-22, for respective firings, indicating that the source of the radiation measured by the sensor is that of the combustion products. The blinding of the radiometer that occurred in Test #ABLMAT-35 is obvious from its radiative heat flux history, which exhibits a sharp decrease in measured radiation about 16 s after SRM ignition that likely corresponds to the alumina coating on the window becoming opaque. The radiometer continues to measure a non-zero, positive radiative heat flux for the remainder of the firing duration due to the relatively high temperature of the deposited alumina and its subtending a much larger solid angle with respect to the sensor than to that of the combustion products. Prior to this sharp decrease at 16 s, the radiative heat flux history from this test is rather similar to those from Tests

#ABLMAT-34 and #ABLMAT-36, but the extent of the useful data acquired from this test is questionable, as the degree of particle coating of the window is uncertain at any given moment during the firing. Nevertheless, it is reasonable to assume that shield gas flow was effective during the time the orifice was choked, so the first 7 s of data is considered reliable for Test #ABLMAT-35. By contrast, the dust that was discovered on the window surface following Tests #ABLMAT-33 and #ABLMAT-34 appears to have had a negligible effect on the radiation measurement, as the magnitude of those radiative

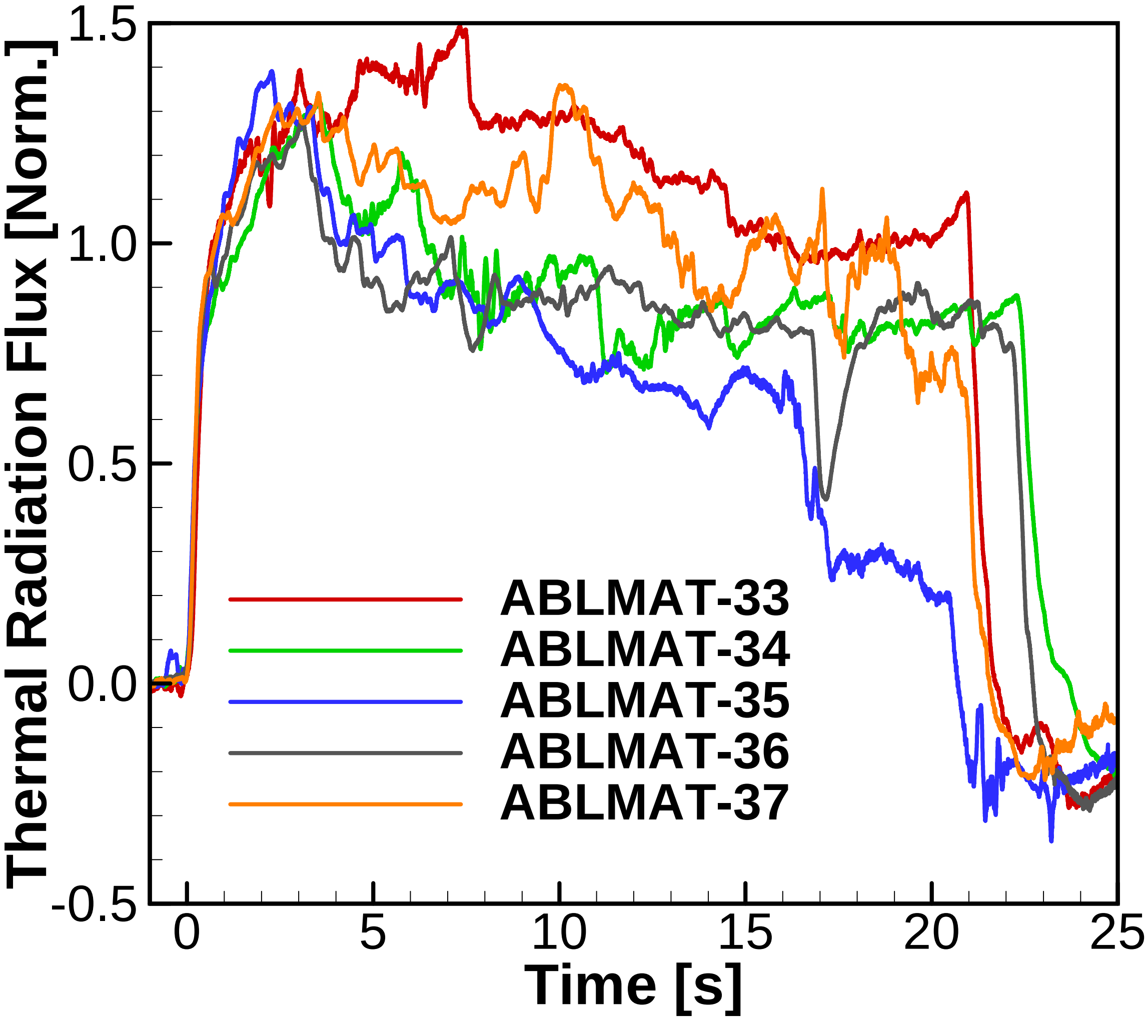

Figure 4-22. Measured radiative heat flux histories from five SRM firings

heat flux histories are similar to or greater than those from Tests #ABLMAT-36 and #ABLMAT-37, whose windows remained absolutely free of any debris.

Much like the pressure histories, the radiative heat flux histories trace very similar paths for the first 3 s of these firings, before their behaviors deviate somewhat. While these data are rather noisy and exhibit many large oscillations (~20% of mean value), the general trend of each is to decrease throughout the firing duration after an initial peak, which occurs between 2 and 3 s after SRM ignition, with the final measured radiative heat flux being, on average (excluding Test #ABLMAT-35), 26% lower than the peak value. This behavior could be due to the end-burning nature of the propellant grain – as the grain burns, its burning surface recedes further towards the fore-end of the SRM, more than doubling the time required for the alumina particles to travel from the burning surface to the radiometer location, as well as exposing increasing amounts of the ablative propellant grain liner to the hot combustion product flow.

Unlike the nonmetallic constituents of the solid propellant, aluminum does not complete its combustion within microns of the propellant surface, but burns relatively slowly after departing the propellant surface, a process potentially extending throughout the internal port of the motor [93]. According to the aluminum burning time correlation of Beckstead [94], particles with a diameters larger than 75 μm (between 14 and 28% of condensed-phase particles [95]) will be undergoing combustion within view of the radiometer when the burning surface of the propellant is at its initial location, and particles with diameters larger than 107 μm (between 10 and 22% [95]) will be burning within view of the radiometer just before burnout. As burning aluminum droplets are potentially a significant source of thermal radiation from the flow channel to the SRM wall [96], the presence of a larger number of these droplets within the view of the radiometer will likely increase the radiation measured by the radiometer relative to a smaller number. Therefore, the temporally-decreasing number density of burning aluminum particles within view of the radiometer is one potential source of the temporal decrease in measured radiation. Additionally, the exposure of ever-increasing amounts of the ablative propellant grain liner will inject increasing amounts of relatively cool, fuel-rich species into the combustion products, including radiatively-participating soot particles, which can absorb and in-scatter a portion of the radiation that would otherwise be incident on the SRM walls. Therefore, the temperature of the combustion product flow will be decreasing with time, and, consequently, the thermal radiation measured by the radiometer.

Two possible processes exist that could cause the radiometer to erroneously accentuate the observed temporal decrease in measured radiation: 1) an increasing number of alumina particles trapped in radiometer port region between the oblique shielding jet and the radiometer and 2) an increasing thickness of alumina deposition on the surface of the aperture disk. Particles trapped in the radiometer port region during the firing are exclusively small and thus quickly cooled by the shielding gas. Any of these particles entering into the radiometer's view will absorb and scatter some of the radiation that would otherwise be incident on the radiometer sensor. The significance of this effect is dependent on the concentration of these particles in the radiometer port at a given time, which can only be accurately quantified through detailed modeling that is unavailable at this time. Post-firing examinations of the aperture disk have revealed a thin layer of alumina deposited on its surface. While the aperture diameter remained completely open, the increasing thickness of this deposition layer can decrease the viewing angle of the radiation sensor with respect to the combustion products, resulting in a reduction in indicated radiation flux. Nevertheless, this layer was measured to be less than 0.03-mm thick, which corresponds to a maximum 0.7% reduction in indicated flux as calculated from the change in the view factor from the aperture to the detector. [91]

In Figure 4-22, the radiative heat flux histories for each of the five firings exhibit a considerable undershoot of zero after the SRM depressurization, the magnitude of which is not correlated to the magnitude of the measurement occurring immediately before SRM depressurization. This behavior is due to redistribution of the interior temperature profile of the sensor, which is not necessarily one-dimensional, as is required for accurate measurement of the incident heat flux, and is not indicative of processes or conditions external to the radiometer.

As an increase in the sensor temperature can cause an artificial decrease in the measured radiation, the temperature history of the radiometer body was measured using a K-type thermocouple for the final four SRM firings. These histories reveal that the largest temperature increase measured during a firing was 18 K, which is negligible with regard to the radiation measurement.

The radiometer was calibrated by Medtherm Corporation using a heated plate, yielding an expanded uncertainty (coverage factor = 2, 95% confidence level) of the radiometer responsivity of ±3% with a test uncertainty ratio (TUR) of less than 4:1. The data acquisition system used to record the radiometer output during the SRM firings possesses and absolute accuracy of ±30 μV, which, when combined with the calibration uncertainty produces an uncertainty of ±3.2% for the average radiation measurement.

Using the same calibration apparatus, the time response of the radiometer was measured by instantaneously exposing the radiometer (by means of a shutter located between the heated plate and the radiometer) to a constant radiant flux equivalent to 72% of the average flux measured in the SRM firings. The time response of the radiometer was thereby determined to be 167 ms – more than adequate considering the SRM firing durations were longer than 20 s.

Chapter 5 Summary & Conclusions

In order to generate empirical data for use in validating ablation models, a subscale SRM for assessing the performance of ablative internal insulation materials was designed, built, and tested. In this subscale SRM, flat ablative material samples, one of PBINBR and one of CFEPDM, were located in a planar, two-dimensional flow channel downstream of an aluminized solid propellant grain, so that they were exposed to an environment nearly identical to that present in a full-scale SRM. For each subscale SRM firing, the degradation behavior of the ablative material samples was imaged with real-time X-ray radiography, so that time-resolved locations of the char surface and char-virgin interface on each ablative sample were identified. Transient subsurface temperatures in the ablative material samples were measured with micro-thermocouples located at various depths within the samples as well. Both the total heat flux and thermal radiation flux to the SRM wall were measured in each subscale SRM firing to characterize the thermal environment. Two series of subscale SRM firings were conducted: one utilizing center-perforated solid-propellant grains for short-duration (~3 s) qualification of the subscale SRM systems and instrumentation and another utilizing end-burning solid-propellant grains to provide more lengthy firing durations (~21 s) for the fully-instrumented ablative insulator assessment firings.

From the results of the six subscale SRM firings and subsequent data analysis performed in this study, it is concluded that:

1. The char layer formed on the surface of CFEPDM under applied SRM conditions expands more rapidly than it erodes, causing the material thickness to increase even as the sample is losing mass. The thermal degradation resistance of the carbon fibers within the material allows the char layer to be retained at large thicknesses, which leads to reduced rates of virgin material pyrolysis and shallower heat affected depths. As evinced by its density stratification, a coking process is occurring within the CFEPDM char layer that is likely increasing the pore pressure within the char layer and for a longer-duration firing, could cause pocketing or sloughing of charred material. A CFEPDM sample included in one of the CP-grain-configured subscale SRM firings, which produce much greater viscous shear and heat-transfer rates in the test section, exhibited observable surface erosion, indicating that the overall behavior of the CFEPDM, not merely the erosion rate, can change depending on the local shear-flow and heat-transfer environment.
2. Under SRM firing conditions, PBINBR develops a char layer that, upon reaching a certain thickness, suddenly sloughs from the surface of the material, exposing the practically virgin material underneath. This process is cyclic, recurring repeatedly throughout the duration of an SRM firing and functions to increase the average rate of material erosion and, thus, increasing total heat-affected depth as compared to a material with better char retention. In addition, the sloughing phenomenon occurring for the PBINBR samples, due primarily to their laminar

construction, increases the variability in total heat affected depth among the various SRM firings, as well, reducing predictability and increasing the necessary design conservatism.

3. Precisely-located micro-thermocouples were successfully used to measure subsurface temperatures in the ablative material samples, the behavior of which correlates well to the ablative sample decomposition behavior observed from the X-ray RTR images.
4. A total heat flux gauge utilizing inverse heat conduction analysis to deduce the total heat flux to the surface of a graphite slab from subsurface temperature measurements within the slab was successfully designed and implemented in a series of subscale SRM firings. The total wall heat fluxes measured using this technique were demonstrated to be reliable, with successful measurements from nine of 11 sensor installations in the long-duration subscale SRM firings, and accurate, exhibiting a maximum calculated measurement uncertainty of 7% of the measured total heat flux.
5. A narrow-view-angle radiometer for measuring the radiation incident on the internal walls of an SRM was successfully designed, fabricated, and implemented. A dual-jet shield gas injection design was demonstrated to be capable of maintaining a clean window throughout the complete duration of SRM firings of greater than 20 s, and the radiation measurements obtained from these firings exhibited good repeatability and physically reasonable temporal behavior. This radiometer design was proven to be robust and capable of providing accurate

(±3.2% uncertainty) measurements of thermal radiation fluxes with quick response (167 ms) within an SRM.

Chapter 6 Future Work

- Use measured convective and radiative heat fluxes, in conjunction with measured thermal properties of both virgin ablative materials and their chars, as inputs to thermo-ablative code and compare computed char surface and char-virgin interface locations and subsurface temperatures with the values measured in the subscale SRM.
- Improve estimate of total heat flux gauge uncertainty by measuring the specific heat of the sensor graphite using differential scanning calorimetry and including the uncertainty in this measurement in the uncertainty analysis of the IHCA. In addition, a three-dimensional model of the heat transfer through the heat flux sensor should be created including the thermocouples and their cavities to produce an estimate of the maximum thermal contact resistance between the sensor graphite and the thermocouple, as well as the disturbance of the temperature profile within the sensor by the thermocouple installation.
- Determine a scaling law for radiometer shielding gas flow, so that the radiometer can be successfully implemented in larger-scale SRMs. This effort would involve CFD modeling of the radiometer installed in various SRM configurations, the definition of an appropriate dimensionless number, and testing of the radiometer under multiple flow conditions with multiple shielding gas mass flow rates.

- Perform long-duration subscale SRM firings with the PBINBR and CFEPDM samples subject to several different heat-transfer and viscous shear rates, as well as to different proportions of convection and thermal radiation. This can be accomplished by using different diameter end-burning solid-propellant grains and/or different propellant formulations.

References

[1] R. W. Humble, Space Propulsion Analysis and Design, New York: McGraw-Hill Primis Custom, 1995, p. 297.

[2] J.-F. Guery, I.-S. Chang, T. Shimada, M. Glick, D. Boury, E. Robert, J. Napior, R. Wardle, C. Perut, M. Calabro, R. Glick, H. Habu, N. Sekino, G. Vigier and B. d'Andrea, "Solid propulsion for space applications: An updated roadmap," *Acta Astronautica,* vol. 66, pp. 201-219, 2010.

[3] A. Biancotti and D. Pastrone, "Modeling Combustion Instability in Aluminized Hybrid Propellants," in *43rd AIAA/ASME/ASEE Joint Propulsion Conference & Exhibit*, Cincinnati, OH, 2007.

[4] G. P. Sutton, Rocket Propulsion Elements, New York: John Wiley and Sons, Inc., 1963, p. 235.

[5] J. H. Koo, D. W. Ho and O. A. Ezekoye, "A Review of Numerical and Experimental Characterization of Thermal Protection Materials - Part I. Numerical Modeling," in *42nd AIAA/ASME/SAE/ASEE Joint Propulsion Conference*, Sacramento, CA, 2006.

[6] P. Reynier, "Convective Blockage during Earth Re-entry: A Review," in *40th Thermophysics Conference*, Seattle, WA, 2008.

[7] D. L. Schmidt, "Ablative Polymers in Aerospace Technology," in *Albative Plastics*, New York, Marcel Dekker, Inc., 1971, pp. 1-39.

[8] C.-L. Hsieh and J. Seader, "Surface Ablation of Silica-Reinforced Composites," *AIAA Journal,* pp. 1181-1187, 1973.

[9] R. D. Mathieu, "Mechanical Spallation of Charring Ablators in Hyperthermal Environments," *AIAA Journal,* vol. 2, no. 9, pp. 1621-1627, 1964.

[10] D. Boury, J. Rey and A. Cronier, "Rubber Materials and Solid Propulsion General Overview & Technical Challenges," in *41st AIAA/ASME/SAE/ASEE Joint Propulsion Conference and Exhibit*, Tucson, Arizona, 2005.

[11] B. Evans, K. K. Kuo, E. Boyd and A. C. Cortopassi, "Comparison of Nozzle Throat Erosion Behavior in a Solid-Propellant Rocket Motor and a Simulator," in *45th AIAA/ASME/SAE/ASEE Joint Propulsion Conference & Exhibit*, Denver, Colorado, 2009.

[12] M. Covington, J. Heinemann, H. Goldstein, Y.-K. Chen, I. Terrazas-Salinas, J. Balboni, J. Olejniczak and E. Martinez, "Performance of a Low Density Ablative Heat Shield Material," in *37th AIAA Thermophysics Conference*, Portland, Oregon, 2004.

[13] Y. Shih, F. Cheung, J. Koo and B. Yang, "Numerical Study of Transient Thermal Ablation of High-Temperature Insulation Materials," *Journal of Thermophysics and Heat Transfer,* vol. 17, no. 1, pp. 53-61, 2003.

[14] V. W. Fitch and N. F. Eddy, "Space Shuttle Solid Propellant Rocket Motors, Asbestos Filled Insulation Replacement," in *33rd AIAA/ASME/SAE/ASEE Joint Propulsion Conference and Exhibit*, Seattle, Washington, 1997.

[15] R. E. Morgan, A. S. Prince, S. A. Selvidge, J. Phelps, C. L. Martin and T. W. Lawrence, "Non-Asbestos Testing Using a Plasma Torch," in *36th AIAA/ASME/SAE/ASEE Joint Propulsion Conference and Exhibit*, Huntsville, Alabama, 2000.

[16] W. Tam and M. Bell, "ASRM Case Insulation Development," in *29th AIAA/SAE/ASME/ASEE Joint Propulsion Conference and Exhibit*, Monterey, California, 1993.

[17] G. W. Russell and F. Strobel, "Modeling Approach for Intumescing Charring Heatshield Materials," *Journal of Spacecraft and Rockets,* pp. 739-749, 2006.

[18] J. F. Maw, R. C. Lui and P. D. Totman, "Verification of RSRM Nozzle Thermal Models With ETM-3 Aft Exit Cone In-depth Temperature Measurements," in *40th AIAA/ASME/SAE/ASEE Joint Propulsion Conference and Exhibit*, Fort Lauderdale, Florida, 2004.

[19] W. D. Brewer, "Graphite and Ablative Material Response to CO2-Laser, Carbon-Arc, and Xenon-Arc Radiation," NASA, Washington, D.C., 1976.

[20] R. T. Swann, W. D. Brewer and R. K. Clark, "Effect of Composition and Desity on the Ablative Performance of Phenolic-Nylon," in *VIII National Meeting of the Society of Aerospace Materials and Process Engineers*, San Francisco, California, 1965.

[21] J. H. Lundell, R. R. Dickey and J. W. Jones, "Performance of Charring Ablative Materials in the Diffusion-Controlled Surface Combustion Regime," *AIAA Journal,* pp. 1118-1126, 1968.

[22] W. W. Congdon, D. M. Curry and T. J. Collins, "Response Modeling of Lightweight Charring Ablators and Thermal Radiation Testing Results," in *39th AIAA/ASME/SAE/ASEE Joint Propulsion Conference and Exhibit*, Huntsville, Alabama, 2003.

[23] K. Skokova and B. Laub, "Experimental Evaluation of Thermal Protection Materials for Titan Aerocapture," in *41st AIAA/ASME/SAE/ASEE Joint Propulsion Conference & Exhibit*, Tucson, Arizona, 2005.

[24] Y. Kobayashi, T. Sakai, T. Suzuki, K. Fujita, K. Okuyama, S. Kato and K. Kitagawa, "An Experimental Study on Thermal Response of Low Density Carbon-Phenolic Ablators," in *47th AIAA Aerospace Sciences Meeting Including The New Horizons Forum and Aerospace Exposition*, Orlando, Florida, 2009.

[25] A. Chaboki, M. Kneer, M. Schneider and J. Koo, "Supersonic Torch Facility for Ablative Testing," in *26th AIAA/SAE/ASME/ASEE Joint Propulsion Conference*, Orlando, Florida, 1990.

[26] J. Koo, S. Lin, M. Kneer and M. Miller, "Comparison of Ablative Materials in a Simulated Solid Rocket Exhaust Environment," in *32nd SDM Structures Structural Dynamics and Materials Conference*, Baltimore, Maryland, 1991.

[27] J. Koo, S. Venumbaka, M. Miller, D. Wilson, D. Beckley and D. Calamito, "Effects of Major Constituents on the Performance of Silicone Polymer Composite," in *30th International SAMPE Technical Conference*, San Antonio, Texas, 1998.

[28] J. Koo, S. Venumbaka, M. Miller, J. Siebunshuh, D. Wilson, D. Beckley, D. Calamito and C. Blackmon, "Thermal Performance of a Class of Silicone Matrix Composites," in *44th International SAMPE Symposium*, Long Beach, California, 1999.

[29] G. Beall, Z. Shirin, S. Harris, M. Wooten, C. Smith and A. Bray, "Development of an Ablative Insulation Material for Ramjet Applications," *Journal of Spacecraft and Rockets,* vol. 41, no. 6, pp. 1068-1071, 2004.

[30] J. H. Koo, L. A. Pilato and G. E. Wissler, "Polymer Nanostructured Materials for Propulsion Systems," in *41st AIAA/ASME/SAE/ASEE Joint Propulsion Conference & Exhibit*, Tucson, Arizona, 2005.

[31] J. H. Koo, M. J. Kneer, S. Lin and M. E. Schneider, "A Cost-Effective Approach to Evaluate High-Temperature Ablatives for Military Applications," *Naval Engineers Journal,* pp. 166-177, 1992.

[32] E. Wernimont, "48-Inch Sub-Scale Motor Material Testing of Space Shuttle Advanced Solid Rocket Motor Carbon Cloth Phenolic Ablatives," in *29th AIAA/SAE/ASME/ASEE Joint Propulsion Conference and Exhibit*, Monterey, California, 1993.

[33] J. McComb and J. Hitner, "Technique for Evaluating the Erosive Properties of Ablative Internal Insulation Materials," in *The 1989 JANNAF Propulsion Meeting*, 1989.

[34] J. Mathis and R. Laramee, "Development of Low Cost Ablative Nozzles for Solid Propellant Rocket Motors," NASA CR-72641, Thiokol Chemical Corporation, Brigham City, Utah, 1970.

[35] P. J. LeBel and J. M. Russell, "Development of Ablation Sensors for Advanced Reentry Vehicles," in *20th Annual ISA Conference and Exhibit*, Los Angeles, California, 1965.

[36] B. McWhorter, M. Ewing, K. Albrechtsen, T. Noble and M. Longaker, "Real-Time Measurements of Aft Dome Insulation Erosion on Space Shuttle Reusable Solid Rocket Motor," in *40th AIAA/ASME/SAE/ASEE Joint Propulsion Conference and Exhibit*, Fort Lauderdale, Florida, 2004.

[37] B. McWhorter, M. Ewing, D. Bolton, K. Albrechtsen, T. Earnest, T. Noble and M. Longaker, "Real-Time Inhibitor Recession Measurements in Two Space Shuttle Reusable Solid Rocket Motors," in *39th AIAA/ASME/SAE/ASEE Joint Propulsion Conference and Exhibit*, Huntsville, Alabama, 2003.

[38] J.-C. Traineau and P. Kuentzmann, "Ultrasonic Measurements of Solid Propellant Burning Rates in Nozzleless Rocket Motors," *Journal of Propulsion,* vol. 2, no. 3, pp. 215-222, 1986.

[39] F. Cauty, "Ultrasonic Method Applied to Full-Scale Solid Rocket Motors," *Journal of Propulsion and Power,* vol. 16, no. 3, pp. 523-528, 2000.

[40] J. Godon, J. Duterque and G. Langelle, "Solid-Propellant Erosive Burning," *Journal of Propulsion and Power,* vol. 8, no. 4, pp. 741-747, 1992.

[41] F. Cauty, J. C. Demerais and C. Erades, "Determination of Solid Propellant Burning Rate Sensitivity to the Initial Temperature by the Ultrasonic Method," *International Journal of Energetic Materials and Chemical Propulsion,* vol. 3, pp. 642-653, 1994.

[42] M. J. Chiaverini, N. Serin, D. K. Johnson, Y.-C. Lu, K. K. Kuo and G. A. Risha, "Regression Rate Behavior of Hybrid Rocket Solid Fuels," *Journal of Propulsion and Power,* vol. 16, no. 1, pp. 125-131, 2000.

[43] N. Paulus, Y. Martin, P. LeHelley and F. Cauty, "Ultrasonic Measurement: An Experimental Way to Improve the Design Method of Internal Thermal Insulators in Solid Rocket Motors," in *35th AIAA/ASME/SAE/ASEE Joint Propulsion Conference and Exhibit*, Los Angeles, California, 1999.

[44] R. A. Frederick, J. Nichols and J. Rogerson, "Slag Accumulation Measurements in a Strategic Solid Rocket Motor," in *32nd AIAA, ASME, SAE, and ASEE, Joint Propulsion Conference and Exhibit*, Lake Buena Vista, Florida, 1996.

[45] Y. Xiao, R. Amano, T. Cal and J. Li, "New Method to Determine the Velocities of Particles on a Solid Propellant Surface in a Solid Rocket Motor," *Journal of Heat Transfer,* vol. 127, pp. 1057-1061, 2005.

[46] G. Young, "Characterization of Combustion and Propulsive Behavior of Difluoroamino Based Solid Propellants," (Master's Thesis) The Pennsylvania State University, University Park, PA, 2001.

[47] R. J. Rollbuhler, "Experimental Investigation of Rocket-Engine Ablative-Material Performance after Postrun Cooling at Altitude Pressures," NASA TN D-1726, National Aeronautics and Space Administration, Lewis Research Center, Cleveland, Ohio, 1963.

[48] E. R. Doering, "Enhancement and Analysis of Real-Time Radiography Images," NASA Marshall Space Flight Center, Huntsville, Alabama, 2004.

[49] J. H. Lundell, R. M. Wakefield and J. W. Jones, "Experimental Investigation of a Charring Ablative Material Exposed to Combined Convective and Radiative Heating," *AIAA Journal,* vol. 3, no. 11, pp. 2087-2095, November 1965.

[50] J. W. Kordig, "Captive-Fired Testing of Solid Rocket Motors," NASA SP-8041, National Aeronautics and Space Administration, Lewis Research Center, Cleveland, Ohio, 1971.

[51] D. Baker, M. Wool and J. Schaefer, "Development of Total and Radiative Heat Flux Measurement Systems for Rocket Nozzle Applications," AFRPL-TR-70-82, Aerotherm Corporation, Edwards, California, 1970.

[52] N. Kimmel, "Alternate Nozzle Ablative Materials Program," NASA CP-175638, Jet Propulsion Laboratory, California Institute of Technology, Pasadena, California, 1984.

[53] C. L. Goldey, W. T. Laughlin and L. A. Popper, "Radiometric Probe Design for the Measurement of Heat Flux within a Solid Rocket Motor," in *SPIE*, 1996.

[54] C. E. Brookley, "Measurement of Heat Flux in Solid Propellant Rocketry," AD428728, Allegany Ballistics Laboratory, Cumberland, Maryland, 1963.

[55] J. D. Moore, R. B. Wehrman, K. K. Kuo, P. J. Ferrara and R. W. Houim, "Flowfield Structure in a Fin-Slot Solid Rocket Motor (Part I)," *Journal of Propulsion and Power,* vol. 25, no. 2, 2009.

[56] R. Bachmann, J. Chambers and W. Giedt, "Investigation of Surface Heat-Flux Measurements with Calorimeters," *ISA Transactions,* vol. 4, no. 2, pp. 143-151, 1965.

[57] T. Diller, "Advances in Heat Flux Measurements," in *Advances in Heat Transfer*, vol. 23, New York, Academic Press, 1993, pp. 279-368.

[58] D. R. Hornbaker and D. L. Rall, "Thermal Perturbations Caused by Heat-Flux Transducers and Their Effect on the Accuracy of Heating-Rate Measurements," *ISA Transactions,* vol. 3, no. 2, pp. 123-130, 1964.

[59] M. W. Rubesin, "The Effect of an Arbitrary Surface-Temperature Variation along a Flat Plate on the Convective Heat Transfer in an Incompressible Turbulent Boundary Layer," Washington, 1951.

[60] W. Reynolds, W. Kays and S. Kline, "Heat Transfer in the Turbulent Incompressible Boundary Layer II - Step Wall-Temperature Distribution," 1958.

[61] D. Mukerji, J. K. Eaton and R. J. Moffat, "Convective Heat Transfer Near One-Dimensional and Two-Dimensional Wall Temperature Steps," *Transactions of the ASME,* vol. 126, pp. 202-210, April 2004.

[62] M. Kandula, G. Haddad and R.-H. Chen, "Three-dimensional thermal boundary layer corrections for circular heat flux gauges mounted in a flat plate with a surface temperature discontinuity," *International Journal of Heat and Mass Transfer,* vol. 50, pp. 713-722, 2007.

[63] J. V. Beck and K. A. Woodbury, "Inverse Problems and Parameter Estimation: Integration of Measurements and Analysis," *Measurement Science and Technology,* vol. 9, pp. 839-847, 1998.

[64] J. V. Beck, B. Blackwell and C. R. St. Clair, Inverse Heat Conduction: Ill-posed Problems, New York: John Wiley and Sons, Inc., 1985, p. 1.

[65] J. V. Beck and K. J. Arnold, Parameter Estimation in Engineering and Science, New York: John Wiley and Sons, Inc., 1977, pp. 4, 370-371.

[66] J. Lindsey and W. Guster, "A Method of Obtaining an Overall Heat Transfer Film Coefficient in Solid Fuel Rocket Nozzles," 1963.

[67] F. Price, V. Marple and R. Dupuis, "Internal Environment of Solid Rocket Nozzles," AD434129, Philco Research Laboratories, Cameron Station, Alexandria, Virginia, 1964.

[68] R. Duval, A. Soufiani and J. Taine, "Coupled radiation and turbulent multiphase flow in an aluminised solid propellant rocket engine," *Journal of Quantitative Spectroscopy & Radiative Transfer,* vol. 84, pp. 513-526, 2004.

[69] F. S. Blomshield, K. J. Kraeutle and R. A. Stalnaker, "Shuttle Redesigned Solid Rocket Motor Aluminum Oxide Investigations," in *31st JANNAF Combustion Meeting*, Sunnyvale, California, 1994.

[70] L. Landers, D. Booth, C. Stanley and D. Ricks, "ASRM Propellant and Igniter Propellant Developement and Process Scale-up," in *29th AIAA/SAE/ASME/ASEE Joint Propulsion Conference and Exhibit*, Monterey, California, 1993.

[71] W. M. Kays and M. E. Crawford, Convective Heat and Mass Transfer, Second ed., New York: McGraw-Hill Book Company, 1980, pp. 175, 220 - 222.

[72] D. Bartz, "A Simple Equation for Rapid Estimation of Rocket Nozzle Convective Heat Transfer Coefficients," *Jet Propulsion,* vol. 27, pp. 49-51, January 1957.

[73] R. L. Geisler, "A Global View of the Use of Aluminum Fuel in Solid Rocket Motors," in *38th AIAA/ASME/SAE/ASEE Joint Propulsion Conference & Exhibit*, Indianapolis, Indiana, 2002.

[74] W. S. Rasband, "ImageJ: Version 1.46p," National Institutes of Health, 1997-2004. [Online]. Available: http://imagej.nih.gov/ij. [Accessed June 2012].

[75] C. Mauer, "Kalman Filter," Open Source ImageJ plug-in, 2003. [Online]. Available: http://rsb.info.nih.gov/ij/plugins/kalman.html. [Accessed June 2012].

[76] E. Caron, M. Wells and D. Li, "A Compensation Method for the Disturbance in the Temperature Field Caused by Subsurface Thermocouples," *Metallurgical and Materials Transactions B,* vol. 37B, pp. 475-483, June 2006.

[77] W. D. Brewer, "Effect of Thermocouple Wire Size and Configuration on Internal Temperature Measurements in a Charring Ablator," NASA TN D-3812, National Aeronautics and Space Administration, Langley Research Center, Langley Station, Hampton, Virginia, 1967.

[78] 1. ASTM Standard E377, *Standard Practice for Internal Temperature Measurements in Low-Conductivity Materials,* West Conshohocken, PA: ASTM International, 2002.

[79] Y. Rabin and D. Rittel, "A Model for the Time Response of Solid-embedded Thermocouples," *Experimental Mechanics,* vol. 39, no. 2, pp. 132-136, June 1999.

[80] R. Morrison, Grounding and Shielding Circuits and Interference, fifth ed., John Wiley and Sons, Inc.: Hoboken, New Jersey, 2007, p. 78.

[81] P. Brown, G. Byrne and A. Hindmarsh, "VODE: A Variable Coefficient ODE Solver," *SIAM Journal of Scientific and Statistical Computing,* vol. 10, pp. 1038-1051, 1989.

[82] P. Roache, "Perspective: A Method for Uniform Reporting of Grid Refinement Studies," *Journal of Fluids Engineering,* vol. 116, pp. 405-413, 1994.

[83] T. Burchall, "Thermal Properties and Nuclear Energy Applications," in *Graphite and Precursors*, P. Delhaes, Ed., Amsterdam, The Netherlands, Gordon and Breach Science Publishers, 2001, p. 90.

[84] H. Coleman and W. Steele, Experimentation and Uncertainty Analysis for Engineers, 2nd ed., New York, NY: John Wiley and Sons, Inc., 1999, pp. 212-213, 162-164.

[85] G. Neuer, "Spectral and Total Emissivity Measurements of Highly Emitting Materials," *International Journal of Themophysics,* vol. 16, no. 1, pp. 257-265, 1995.

[86] S. Gordon and B. J. McBride, "Computer Program for Calculation of Complex Chemical Equilibrium Compositions and Applications," NASA Reference Publication 1311, Cleveland, OH, 1996.

[87] C. Kidd, "A Durable, Intermediate Temperature, Direct Reading Heat Flux Transducer for Measurements in Continuous Wind Tunnels," AEDC-TR-81-19 (ADA107729), Arnold Air Force Station, TN, 1981.

[88] J.-Y. Jung and M. Brewster, "Radiative Heat Transfer Analysis with Molten Al2O3 Dispersion in Solid Rocket Motors," *Journal of Spacecraft and Rockets,* vol. 45, no. 5, pp. 1021-1030, September-October 2008.

[89] M. F. Modest, Radiative Heat Transfer, second ed., New York: Academic Press, 2003.

[90] L. Dombrovskii, "Approximate Methods for Calculating Radiation Heat Transfer in Dispersed Systems," *Thermal Engineering,* vol. 43, no. 3, pp. 235-243, 1996.

[91] S. Tanaka, "Exact view-factor analysis for radiation from a disk to another coaxial disk through a coaxial hole," *Review of the Faculty of Maritime Sciences,* vol. 4, pp. 25-32, 2007.

[92] R. A. Rindal, "An Analysis of the Coupled Chemically Reacting Boundary Layer and Charring Ablator Part VI: An Approach for Characterizing Charring Ablator Response with In-Depth Coking Reactions," NASA CR-1065, National Aeronautics and Space Administration, Washington, D.C., 1968.

[93] J. Harrison and M. Brewster, "Analysis of Thermal Radiation from Burning Aluminum in Solid Propellants," *Combustion Theory and Modelling,* vol. 13, no. 3, pp. 389-411, 2009.

[94] M. Beckstead, "Correlating Aluminum Burning Times," *Combustion, Explosion, and Shock Waves,* vol. 41, no. 5, pp. 533-546, 2005.

[95] M. Brennan, "Recent Combustion Bomb Testing of RSRM Propellant," in *Proceedings of the 36th AIAA/ASME/SAE/ASEE Joint Propulsion Conference*, Lake Buena Vista, Florida, 1996.

[96] M. Brewster and J. Harrison, "Thermal Radiation from Burning Aluminum and Oxide Particles in Solid Propellants," *International Journal of Energetic Materials and Chemical Propulsion,* vol. 8, no. 2, pp. 99-112, 2009.

VITA

Heath Thomas Martin

Heath Thomas Martin was raised on a small cattle farm in rural northern Alabama, less than an hour's drive from Redstone Arsenal, where his grandfather designed rocket motors for tactical missiles, and NASA's George C. Marshall Space Flight Center, whose Space and Rocket Center Heath first visited at the age of three. An interest in pursuing engineering professionally and in watching quality football led him to matriculate to the University of Alabama in the Fall of the year 2000, where despite a preseason No. 3 ranking, the team finished a dispiriting 3-8, but Heath was named Outstanding Freshman in Mechanical Engineering. Four alternating semesters of full-time work in Operations Engineering in the Assembly Shop at Mercedes-Benz U.S.-International in Vance, AL as part of the University's Cooperative Education program provided a valuable education in practical engineering in a corporate environment as well as an earnest desire to seek an advanced degree. Through an association with Dr. John Baker, his thermodynamics professor, Heath performed undergraduate research project working with hybrid rocket motors, the scholarly inquiry for which lead him to the seminal works on HTPB combustion in hybrids produced by members of The Pennsylvania State University's High Pressure Combustion Lab (HPCL). After being frustrated in his attempt to perform live firings of a gaseous bipropellant rocket engine due to a lack of proper facilities while working on his Master's degree under Dr. Baker at the University of Alabama, Heath was dazzled by the resources he discovered at the HPCL while on a tour and decided then to pursue his doctorate under Distinguished Professor Kenneth Kuo. After completing his Master's thesis entitled "Optimal Rocket Performance Using Evolutionary Algorithms", he began his tenure at the HPCL in August of 2006, during which he was involved in the study of the assessment of the performance of ablative internal insulators in solid rocket motors, the topic of his dissertation, as well as a study of the temperature sensitivity of granular double-base propellants for mortar systems. Upon completion of his doctorate, Heath will continue his study of ablative insulator performance in solid rocket motors as a thermal analyst with Jacobs Engineering in Huntsville, Alabama.